THERMAL ANALYSIS OF COAL UNDER CONDITIONS OF RAPID HEATING

Hyok B. Kwon
Department of Environmental Protection, Kyungnam University
449 Wolyoung-Dong, Happo-Ku, Masan, 631-701 KOREA
and
Francis J. Vastola
Department of Materials Science and Engineering
Pennsylvania State University, University Park, PA 16802

Keywords: coal, pyrolysis, thermophysical property

INTRODUCTION

The heat effects of coal pyrolysis can be defined in terms of the sensible heats of the reacting substance and the heats of reaction. The heat capacities of coals and chars, necessary to evaluate the sensible heat contributions, have been measured by a variety of experimental techniques and the early published data have been reviewed (1, 2). However, the heat effects of pyrolysis have been the subject of considerable debate. Some investigators (3, 4) found that the pyrolysis was endothermic, while others (5-8) found it to be of an exothermic process. Temperature dependence (9) and rank dependence (10) of pyrolysis energetics add more complexities to the heat effects of pyrolysis processes.

Thermophysical properties such as the pyroheat, pyroheat capacity, and heat of pyrolysis of coal are important energetic data in design computations relating to various coal utilization processes. The most important use of thermophysical properties is in heat balance calculations. In general, the temperature of sufficiently small particles (say, 200 μm) during pyrolysis is assumed to be similar to that of the surrounding environment due to rapid heat transfer. Therefore, heat transfer does not influence the weight loss. And in most of the models used to predict the heat transfer effects, the net heat of pyrolysis is ignored. Freihaut and co-workers (11) incorporated heats of reaction in their model and predicted transport limitations for particle diameters below 100 μm. The endothermic heat effects during rapid pyrolysis have been identified (12, 13) qualitatively.

The objectives of this study were to measure the thermophysical properties of coal under conditions of rapid heating.

EXPERIMENTAL

Apparatus. A schematic diagram of the system used in this work is presented in Figure 1. Details of the apparatus and procedure are given elsewhere (14). The main components of the calorimeter are the grid reactor, electrical system, and microcomputer. The microcomputer is coupled with the reactor through a voltage regulator and a multiplexed analog/digital (A/D) converter for process control and data acquisition.

Electrical Heating. The reactor is an SS (Type 315) grid which is electrically heated by a constant voltage power supply. Heating rates were controlled by an adjustable voltage regulator powered by an acid-lead battery. The low internal resistance batteries and regulator ensure constant voltage at high current. The SS mesh grid and a brass bar, used as a reference resistance, make up the heating circuit (Figure 2). The low resistance (5.17 mΩ) and large mass (50 g) of the reference resistor minimize the changes in resistance from the variation in temperature due to resistive heating. Therefore, the reference resistance can be assumed to be constant during the experiment. The temperature of the reactor is monitored by a thermocouple spot-welded to the grid. For a given constant voltage the grid temperature reaches a steady state at which the resistive heat input balances losses by heat transfer. After being held at the final steady state temperature for the desired time, the sample is cooled by turning the power off. While the cooling period may last for a

few seconds, after the first 100 ms or so, the temperature becomes too low for pyrolysis reactions to continue (Figure 3).

Temperature Measurement. The pyrolysis temperature, defined as the temperature at the middle of the grid, is determined from a thin (50 μm) chromel-alumel thermocouple. The uncertainty in the actual temperature of the sample is reduced by use of a sample holder which contains a thermocouple as an integral part. A spot-weld fixes the junction just outside the folded grid near its center. Interaction between the heater and thermoelectric circuits at the mesh can cause gross distortions of the temperature signal and must be avoided. In this experiment, the thermoelectric circuits are isolated from the heating circuit by a differential input instrumentation amplifier.

Process Control and Data Acquisition. The system consists of an Apple II+ microcomputer and an 8-bit multiplexed A/D converter. The computer communicates with the system in two modes. First, the computer initiates and terminates the heating. Secondly, the computer monitors the change in the total voltage, the voltage across the reference resistor, and the thermocouple emf.

Calibration. A number of substances (Sn, Zn, Al; Aldrich Chemical Co., 5N) undergoing phase transitions at temperatures up to 933 K were tested (Table I). Temperature calibration was carried out using melting temperatures of these materials. At the same time, calorimetric calibration was carried out by using the enthalpies of fusion of these substances at their melting temperatures. The interval of the discontinuity corresponds to the enthalpy change (Figure 4). According to the calibration, the system overestimated the enthalpy change up to 19%, with 10% precision. The most probable reason for this overestimation is the underestimation of the heat loss of the grid. If the small metal sample is localized near the center of the grid employed, there will be a temperature difference through the grid, especially during the metal transition period. During this period, the transition tends to hold the grid temperature constant near its contact, while the temperature of the remainder of the grid increases. Since the temperature of the grid is monitored by the spot-welded thermocouple at the middle of the grid, its measured temperature underestimates the grid temperature and results in the undercompensation of heat loss, which is a strong function of temperature. This consideration is amply supported by experiment. If a small sample is located at the center of the grid, a three to five times greater experimental value than the literature value is obtained. However, when larger samples are spread over a larger area of the grid, this effect is markedly reduced. Moreover, this effect is markedly reduced both by the small particle size (140 x 170 mesh) and large mass (about 8 mg) of the coal used and by the less abrupt and more gradual coal pyrolysis reactions as contrasted with the sharp phase transition of a metal.

Sample Selection. Coal samples were obtained from the Penn State coal sample bank. Proximate and ultimate analyses of the coals are provided by the Penn State coal database and are presented in Table II.

Experimental Conditions. Experimental conditions are listed below:

1. Sample size	8.0 ± 0.2 mg
2. Particle size	100 microns (140 x 170 mesh)
3. Drying	Vacuum dry overnight at 383 K and in situ for 5 min at 393 K
4. Duration of reaction	20 sec
5. Final temperature	880 ± 5 K
6. Heating rate	200 K/s at 1 sec
7. Soaking time	15 sec
8. Data acquisition interval	20 ms

Procedure. After a thermocouple was welded to a new mesh, which was folded into a "sandwich" heating element, forming a 2.5 x 12 mm strip and connected across the electrodes, the cell was evacuated, charged with nitrogen gas, and prefired to prevent further physical and chemical change

of the mesh. During the prefiring, the mesh expanded and annealed until it reached a steady state condition. Then, 5 to 10 mg of coal sample was loaded into the mesh. The particles had a uniform diameter of approximately 100 μm (140 x 170 US mesh). This size was easily contained in the mesh with its 60-μm openings. After the coal was loaded, the cell was charged with nitrogen gas. The coal was dried inside the reactor for 10 min at 393 K. Next, the coal-grid system was heated with a constant voltage pulse, then cooled via simple heat dissipation. Subsequently, the remaining grid-char runs were made.

Data Reduction. In order to derive the thermal properties from the raw data, it is necessary to follow the reduction procedure which is described below and graphed in Figure 5. The interpretation of each symbol is given in Table III. Figure 2 shows the equivalent electrical circuit of the reactor. By measuring at 20-ms intervals, the two voltages e_s, e_r, and e_{tc}, the temperature of the system can be measured and the power input to the system, Wi can be calculated,

$$W_i = \frac{e_s e_r}{R_r} \qquad [1]$$

versus time. The power loss from the system at a given temperature can be calculated by determining the convective and radiative heat loss versus temperature according to the expression

$$W_l = A(T_g - T_{rm}) + B(T_g^4 - T_{rm}^4) \qquad [2]$$

The terms A and B can be obtained experimentally at the end of a char run by heating the system to a series of temperatures and fitting the data to Equation 2 using an iterative technique. A check can be made to ascertain whether the radiation coefficient, B, is physically valid or not by comparing emissivity. Since the Stefan-Boltzmann law also can be applied to grey bodies, emissivity is the ratio of the radiation density of a surface to that of a black body at the same temperature.

$$\epsilon = \frac{\text{energy actually radiated by the system}}{\text{energy radiated if the system were black}}$$

$$= \frac{\text{evaluated radiant energy}}{\text{radiant energy black body}}$$

$$= \frac{B(T^4 - T_{rm}^4)}{S(T^4 - T_{rm}^4)\sigma}$$

$$= \frac{B}{S\sigma} \qquad [3]$$

The calculated emissivities (Table IV) from the evaluated radiation coefficients using Equation 3 are in good agreement with literature values (oxidized metals = 0.6 – 0.85; carbon, lampblack = 0.95[16]). By being able to measure the power input to the system versus time and temperature and by being able to calculate the power loss from the system versus temperature, net power absorbed by the system versus time can be calculated. From these values the integral of heat absorbed by the system versus time can be obtained. Each run would consist of three heatings, the grid alone, the coal sample in the grid, and finally the char remaining in the grid. By being able to normalize the runs to power absorbed versus temperature, the net heat absorbed by the grid, coal, and char is obtained (Figure 5d). The substraction of the heat absorbed by the grid from that of the coal and the char runs enables the net heat requirements for heating the coal and the char to the final temperature to be obtained. The heat of pyrolysis is arrived at by subtracting the net heat absorbed by the char from that of the coal (Figure 5e). The differential of these values is shown in Figure 5f. The data are presented on the basis of the original mass of the coal sample.

RESULTS AND DISCUSSION

The thermophysical properties measured were 1) pyroheat, ΔH_{ph}, which is the energy required to heat coal to a given temperature and is the sum of the heat of pyrolysis and heat capacity over the heating temperature interval; 2) pyroheat capacity, C_{ph}, which is the pyroheat normalized over a differential temperature interval; 3) heat of pyrolysis, ΔH_{py}, which is the thermal difference between heating coal and char to the same final temperature; and 4) pyrolysis heat capacity, C_{py}, which is the heat of pyrolysis normalized over a differential temperature interval. The experimental results for the coal samples are presented in Tables V through VII.

Char. As can be seen in Table V, the heat capacity of the char increases from room temperature to approximately 700 K. Since these figures are based on the original weight of coal, the reported pyroheat capacity will be inversely dependent upon the VM content of the original coal. PSOC 867, with the smallest amount of VM and hence the greatest amount of remaining char, has the highest reported pyroheat and pyroheat capacity.

Coal. As the coal is heated, the mass remaining will decrease as VM is lost from the system being heated. Since the thermal data are reported on an original mass basis, the VM loss would tend to decrease the apparent pyroheat capacity; however, Table VI shows that the measured pyroheat capacity increases to a maximum in the 650 to 700 K temperature region. This is due to the endothermic reactions that are taking place during the pyrolysis. As the pyrolysis rate approaches its maximum in this temperature region, a significant portion of the energy absorbed is due to the pyrolysis. At the highest heating temperature, the pyroheat capacity of the remaining sample is close to that of the second heating (char run), indicating little VM was released during the char heating.

Pyrolysis. The difference in the quantity of heat needed to heat coal and the char to the same final temperature is that necessary to bring the coal material that will decompose to its decomposition temperature plus the heat required for the endothermicity of the reaction. Figure 4e and Table VII show that this amounts to a significant portion of the energy required to heat the coal. The differential of ΔH_{py}, C_{py} can be seen to peak during the period of maximum pyrolysis and then decrease as the pyrolysis rate approaches a low value. It should be noted that the pyroheat capacities of coal measured in this study do not include the energy necessary to heat the VM once it has been released from that release temperature to the final heating temperature.

CONCLUSIONS

The pyrolysis process for all the coals studied in this investigation was endothermic over the temperature range from 298 to 875 K. The pyrolysis rate and consequently the maximum rate of energy absorption approaches its maximum for all the coals in the temperature range 650 to 700 K. As the pyrolysis rate approaches its maximum in this temperature region, a significant portion of the energy absorbed is due to the endothermic reactions that are taking place during the pyrolysis. The differential of ΔH_{py} shows the peak during the period of maximum pyrolysis and the decrease as the pyrolysis rate approaches a low value.

ACKNOWLEDGMENTS

This study was made possible by financial support from the Coal Cooperative Program at The Pennsylvania State University. The authors thank the Penn State Coal Sample Bank and Data Base for supplying the sample and the analysis of the coal used in this study.

REFERENCES

1. Badzioch, S. *BCURA Monthly Bull.* **1960**, 24(11), 485-520.

2. Kirov, N.Y. *BCURA Monthly Bull.* **1965**, 29(2), 33-39.

3. Davis, J.D.; Place, P.B. *Ind. Eng. Chem.* **1924**, 16(6), 589-592.

4. Lopez-Peinado, A.J.; Tromp, P.J.J.; Moulijn, J.A. *Fuel* **1989**, 68, 999-1004.

5. Whitehead, W.L.; Breger, I.A. *Science* **1950**, 111, 279-281.

6. Berkowitz, N. *Fuel* **1957**, 36, 355-373.

7. Gold, P.I. *Thermochimica Acta* **1980**, 42, 135-152.

8. Elder, J.P.; Harris, M.B. *Fuel* **1984**, 63, 262-267.

9. Agroskin, A.A.; Goncharov, E.I. *Coke Chem. USSR* **1980**, 12, 15-18.

10. Mahajan, O.P.; Tomita, A.; Walker, P.L., Jr. *Fuel* **1976**, 55, 63-69.

11. Freihaut, J.D.; Leff, A.A.; Vastola, F.J. *Prepr. Am. Chem. Soc., Div. Fuel Chem.* **1977**, 22, 149-157.

12. Freihaut, J.D.; Zabielski, M.F.; Serry, D.J. *Prepr. Am. Chem. Soc., Div. Fuel Chem.* **1982**, 27, 89-98.

13. Morel, O.; Vastola, F.J. *Prepr. Am. Chem. Soc., Div. Fuel Chem.* **1984**, 29, 77-82.

14. Kwon, H.B. Ph.D. Thesis, The Pennsylvania State University, **1987**.

15. Weast, R.C. Ed., *CRC Handbook of Chemistry and Physics*; 64th ed., CRC Press: Boca Raton, Florida, **1983**; E-385.

Table I. Calibration

Standard Substance	Literature (15)		Measured	
	m.p.(K)	ΔH_{fusion}(J/g)	m.p.(K)	ΔH_{fusion}(J/g)
Sn	505.1	60.7	496	71
			496	67
			495	70
Zn	692.7	113.0	688	120
			690	127
			691	125
Al	933.5	396.0	928	414
			920	423
			932	450

Table II. Characteristics of Coal Used

PSOC No.	423	415	572	309	867
Apparent Rank	SUBB	SUBC	HVC	HVC	AN
Proximate Analysis (dry)					
% Moisture (as received)	24.1	31.0	3.5	10.1	3.8
% Ash	13.6	11.1	6.4	20.4	13.9
% Volatile Matter	50.5	50.6	52.6	37.6	3.7
% Fixed Carbon	35.9	38.3	41.1	42.0	82.4
Ultimate Analysis (daf)					
% C	72.6	72.5	73.1	77.1	95.1
% H	6.1	5.7	4.9	5.8	1.2
% N	1.1	1.4	0.0	1.7	0.8
% S (total)	2.0	0.9	0.3	1.0	0.6
% O (by difference)	18.1	19.4	21.7	14.4	2.3
Net Calorific Value (kJ/g, dmmf)	30.3	29.4	27.5	31.6	34.4

Table III. Data Reduction Symbols

	English Symbols
A	Coefficient for conduction and convection
B	Coefficient for radiation
e	Voltage drop
H	Enthalpy
I	Current
R	Resistance
T	Temperature
W	Power
	Subscripts
g	Grid
i	Input
l	Loss
r	Reference
s	System
rm	Room
tc	Thermocouple

Table IV. Calculated Emissivities[a]

PSOC No.	Run No.	B ($\times 10^{-12}$)	ϵ
423	830	5.372	0.65
415	780	5.465	0.66
572	680	6.960	0.84
309	790	6.485	0.78
867	1000	5.906	0.71

[a] Measured surface area of grid, 1.46×10^{-4} m^2;
Calculated emissivity of black body; $\epsilon = 5.67 \times 10^{-8}$ W/m^{2}K^4.

Table V. Thermophysical Properties of Char

PSOC ID No.	423		415		572		309		867	
Temperature (K)	ΔH_{ph} (J/g)	C_{ph} (J/gK)	ΔH_{ph} (J/g)	C_{ph} (J/gK)	ΔH_{ph} (J/g)	C_{ph} (J/gK)	ΔH_{ph} (J/g)	C_{ph} (J/gK)	ΔH_{ph} (J/g)	C_{ph} (J/gK)
400	35	0.52	30	0.51	13	0.48	24	0.48	41	0.74
425	52	0.63	50	0.63	28	0.61	38	0.59	63	0.89
450	69	0.73	64	0.75	46	0.74	56	0.69	92	1.04
475	89	0.83	88	0.87	66	0.87	72	0.79	121	1.18
500	112	0.92	110	0.98	91	0.98	96	0.87	159	1.30
525	138	1.00	138	1.08	121	1.08	121	0.96	191	1.42
550	165	1.08	167	1.16	151	1.19	151	1.04	226	1.51
575	194	1.15	201	1.24	184	1.29	174	1.11	269	1.60
600	221	1.20	235	1.31	213	1.37	201	1.19	313	1.69
625	257	1.25	265	1.37	250	1.44	236	1.26	356	1.77
650	291	1.30	306	1.42	293	1.48	269	1.34	403	1.84
675	323	1.33	340	1.45	333	1.52	302	1.42	445	1.90
700	357	1.34	376	1.47	370	1.56	337	1.49	502	1.93
725	392	1.34	416	1.47	411	1.58	377	1.54	553	1.94
750	429	1.34	458	1.47	448	1.59	419	1.58	605	1.94
775	465	1.33	492	1.46	490	1.60	464	1.61	652	1.94
800	496	1.32	530	1.46	534	1.60	506	1.62	701	1.93
825	524	1.32	566	1.45	573	1.60	542	1.63	742	1.93
850	552	1.32	595	1.45	612	1.60	578	1.64	783	1.93
875	578	1.32	623	1.45	649	1.60	614	1.64	825	1.93

Table VI. Thermophysical Properties of Coal

PSOC ID No.	423		415		572		309		867	
Temperature (K)	ΔH_{ph} (J/g)	C_{ph} (J/gK)	ΔH_{ph} (J/g)	C_{ph} (J/gK)	ΔH_{ph} (J/g)	C_{ph} (J/gK)	ΔH_{ph} (J/g)	C_{ph} (J/gK)	ΔH_{ph} (J/g)	C_{ph} (J/gK)
400	43	0.81	41	0.75	20	0.64	33	0.71	46	0.76
425	68	1.00	57	0.95	36	0.82	55	0.88	70	0.91
450	101	1.18	84	1.15	63	1.01	80	1.04	96	1.06
475	133	1.35	121	1.34	93	1.19	110	1.18	126	1.20
500	172	1.51	160	1.52	123	1.37	145	1.32	160	1.33
525	212	1.65	205	1.67	164	1.54	182	1.44	196	1.45
550	259	1.77	253	1.82	207	1.70	222	1.56	235	1.55
575	307	1.86	293	1.94	255	1.84	263	1.68	276	1.65
600	355	1.95	352	2.05	301	1.96	305	1.79	322	1.74
625	410	2.02	403	2.13	356	2.06	352	1.89	367	1.82
650	462	2.07	463	2.20	411	2.14	403	1.97	414	1.89
675	513	2.09	521	2.24	468	2.20	456	2.03	464	1.94
700	571	2.06	576	2.22	526	2.22	508	2.06	514	1.97
725	628	1.98	636	2.14	583	2.21	566	2.00	566	1.97
750	678	1.83	697	1.97	644	2.10	620	1.87	619	1.96
775	729	1.67	755	1.79	702	1.93	674	1.76	670	1.94
800	772	1.56	799	1.66	754	1.79	721	1.70	717	1.93
825	805	1.49	834	1.59	803	1.71	763	1.66	761	1.93
850	838	1.46	863	1.55	839	1.66	798	1.65	804	1.92
875	864	1.45	892	1.54	876	1.64	834	1.65	846	1.92

Table VII. Thermophysical Properties of Pyrolysis

PSOC ID No.	423		415		572		309		867	
Temperature (K)	ΔH_{ph} (J/g)	C_{ph} (J/gK)	ΔH_{ph} (J/g)	C_{ph} (J/gK)	ΔH_{ph} (J/g)	C_{ph} (J/gK)	ΔH_{ph} (J/g)	C_{ph} (J/gK)	ΔH_{ph} (J/g)	C_{ph} (J/gK)
400	8	0.26	10	0.22	6	0.15	9	0.22	5	0.02
425	15	0.35	7	0.30	7	0.20	16	0.28	7	0.02
450	32	0.43	19	0.39	17	0.26	24	0.33	4	0.02
475	43	0.51	32	0.46	27	0.32	37	0.39	4	0.02
500	59	0.58	49	0.52	31	0.38	49	0.43	0	0.03
525	74	0.64	67	0.58	42	0.45	61	0.47	4	0.03
550	94	0.68	85	0.64	56	0.50	71	0.51	9	0.04
575	112	0.71	92	0.69	70	0.54	88	0.55	7	0.05
600	133	0.74	116	0.73	87	0.58	103	0.59	8	0.05
625	152	0.76	138	0.76	105	0.61	116	0.62	10	0.05
650	171	0.77	156	0.78	118	0.65	133	0.63	10	0.05
675	189	0.76	180	0.79	134	0.67	154	0.62	19	0.04
700	214	0.73	199	0.76	156	0.67	170	0.58	11	0.03
725	236	0.66	219	0.69	171	0.64	189	0.48	12	0.03
750	248	0.52	239	0.54	195	0.53	200	0.32	14	0.02
775	264	0.37	263	0.37	211	0.37	209	0.19	17	0.01
800	276	0.26	268	0.23	220	0.22	214	0.09	16	0.00
825	281	0.19	268	0.15	229	0.12	221	0.04	18	0.00
850	285	0.15	268	0.11	227	0.07	220	0.02	20	0.00
875	286	0.14	269	0.09	227	0.05	220	0.02	21	0.00

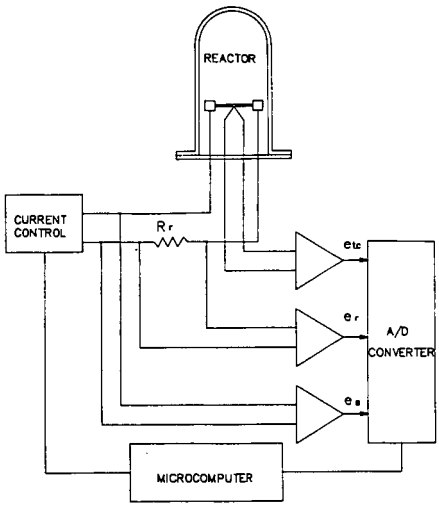

Figure 1. Schematic diagram of the system.

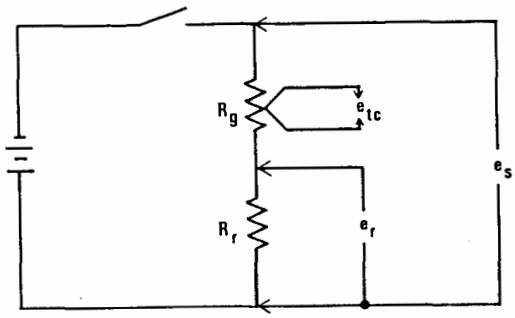

Figure 2. Equivalent circuit of the heating system.

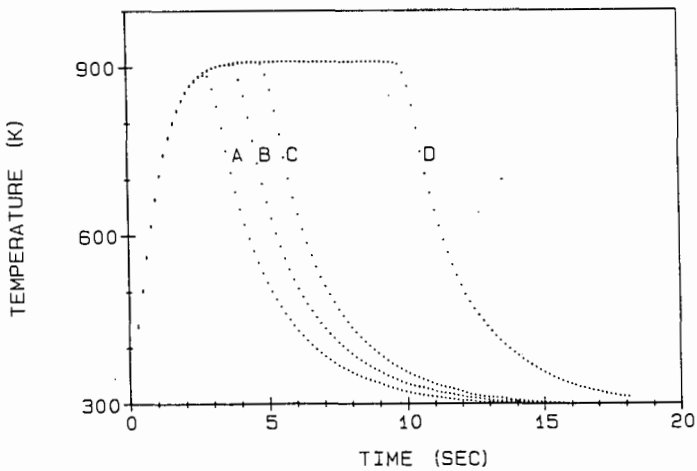

Figure 3. Heating and cooling curves for blank grid. Soak time at final temperature (sec.); 0 (A), 1 (B), 2 (C), and 7 (D).

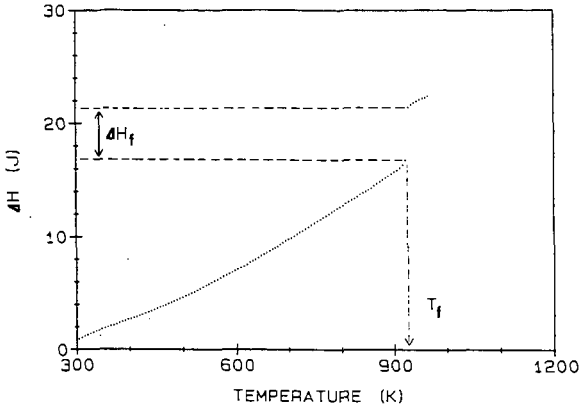

Figure 4. Typical calibration run for aluminum.

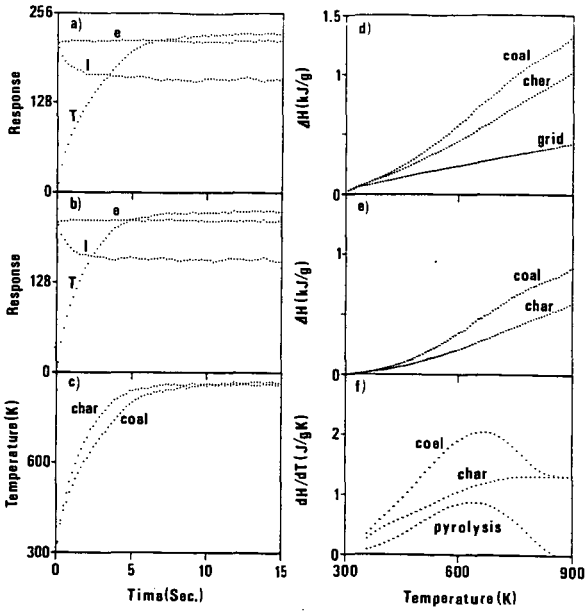

Figure 5. Data reduction. Coal run (a), char run (b), temperature profile (c), enthalpy change (d), normalized enthalpy change (e), and rate of enthalpy change (f).

EVALUATION OF THE SURFACE PROPERTIES OF ILLINOIS BASIN COALS

I. Demir[1], A. A. Lizzio[1], E. L. Fuller[2], and R. D. Harvey[1]
[1]Illinois State Geological Survey, 615 E. Peabody Drive, Champaign, IL 61820. [2]Oak Ridge National Laboratory, PO Box 2008, MS-6088, 1 Bethel Valley Road, Oak Ridge, TN 37831

Keywords: coal, surface area, diffuse reflectance infrared spectroscopy

INTRODUCTION

The surface properties of coal, such as surface area, pore volume and surface chemical structure, affect the physical-chemical behavior of coal in many coal conversion and cleaning processes. Knowledge of the surface area and porosity of a given coal is of major importance in understanding the mass transport phenomena that govern its physical-chemical behavior. For example, Mahajan and Walker [1] pointed out that the amount and ease of extraction of coal-bed methane are controlled by the porosity and pore size distribution of the coal. The porosity of coal affects its specific gravity, which is critical in those coal preparation processes that take advantage of density differences between coal and mineral matter. In coal conversion (e.g., gasification), the transport of reactants to the internal coal surface and the escape of product molecules from the pores are significantly influenced by the pore structure. Surface area and porosity data can be especially useful for removal of organic sulfur from coal. Organic sulfur occurs in coal as part of both aromatic and aliphatic functional groups and as thioether bridges [2,3]; that is, most of the organic sulfur appears to be located on or near the micropore walls. An important limiting factor for removal of organic sulfur may be the diffusion of reacting agents into and product molecules out of the micropores. Knowledge of the pore structure of the coal precursor can also be helpful in predicting the type of porosity that may develop and, hence, in assessing the suitability of the coal for the production of activated carbons, carbon molecular sieves, etc.

Interpretations of data on surface area and porosity of coal differ due to the physical and chemical complexity of coal. Gregg and Sing [4] reviewed the use of adsorption methods for the determination of surface area and pore size distribution of porous solids. Fuller [5] suggested that accessibility (to adsorbates) is probably a better term to define the surface area and pore structure of coal. Marsh [6] stated that the concept of a "real" or "true" physical surface area does not exist for microporous coals and carbons and recommends the use of the "equivalent" surface area, i.e., the value of surface area which the adsorbent exhibits under the experimental conditions used. The commonly applied theoretical equations used to interpret adsorption isotherms include those of Langmuir, Brauner-Emmett-Teller (BET), Dubinin-Radushkevich (DR), and Dubinin-Astakhov (DA). The Langmuir and BET equations supposedly predict monolayer coverage by the adsorbate in porosity on external surfaces, from which a surface area can be calculated. The other two equations essentially are applied to CO_2 adsorption to predict the micropore volume that can then be multiplied by the cross-sectional area of the CO_2 molecule to calculate the surface area. Because a large percentage of the coal porosity is in micropores (<20 Å in diameter), micropore surface area very closely approximates the total surface area [7].

Mercury porosimetry is another technique that is used to determine surface area and pore volume of coal. The mercury porosimetry technique is based on measuring the amount of mercury penetration into pores as a function of applied pressure. Although coals are aperture-cavity type materials [1,8], the mercury porosimetry computations treat pores as cylindrically shaped. Such a simplification is generally accepted for treating what, otherwise, would be a complex problem. Mercury porosimetry yields useful data on large pores, but measurements of smaller pores (obtained at high pressures) are questionable because the compressibility of coal results in particle breakdown and/or enlargement of some pores at the expense of others.

In short, the surface area and pore volume of a microporous solid, such as coal, depend on how they are measured and how the adsorption or intrusion data are interpreted. If all conditions are specified, data on the surface area and pore volume of coal have value and application, especially for comparing the physical-chemical behavior of one coal to that of another.

Oxidation of coal samples can significantly change their porosity and surface area. For example, Kaji et al. [9] showed that the extent of low temperature (30-180°C)

oxidation correlated negatively with internal surface area of pores >100 Å in diameter for five coals that ranged in rank from subbituminous to anthracite. The surface chemical structure of coal can be delineated using diffuse reflectance infrared spectroscopy (DRIS) [10-12]. The DRIS technique can also be used to monitor changes in the surface chemical structure of coal during oxidation processes [13-15].

The goal of this study was to establish a data base for surface properties of the coals in the Illinois Basin Coal Sample Program (IBCSP) to aid coal scientists and engineers in the research and development of improved processes for desulfurization and increased utilization of Illinois Basin coals. Surface area and pore volume distributions and surface chemical structure of eight IBCSP coals were determined in both a (relatively) unoxidized and oxidized state. Statistical relationships among these surface properties and other available characterization data on these coals were also determined and evaluated.

EXPERIMENTAL

Samples

Eight of the IBCSP coals were obtained in a fresh state, i.e., with minimum prior exposure to air (Table 1). After their removal from the IBCSP storage barrels, a 750 g representative split of each coal (except IBC-108) was placed in a rod mill, purged with argon gas, and dry-ground for 30 minutes to reduce the particle size to <100 mesh; the IBC-108 coal is supplied by the IBCSP only in micronized form (<400 mesh). An analysis of the ground samples with a Microtrac particle size analyzer indicated that the particle size of each was reduced to about 90% <100 mesh (<149 μm) with a mean volume size diameter ranging from 38 to 60 μm. A split of each ground sample was analyzed for surface properties in the fresh state. Another split of each sample was exposed to air oxidation at room temperature for two months and then analyzed similarly to investigate the effect of this mild oxidation on the surface properties of the coals. The analytical methods used to determine the surface properties of the samples are briefly described below.

Gas Adsorption

The samples were analyzed on a Quantachrome Autosorb-1 gas sorption system to obtain CO_2 and N_2 adsorption isotherms at 273 and 77 K, respectively. Surface areas were computed from the analysis of N_2 and CO_2 adsorption isotherms using the BET and DR equations, respectively. Molecular cross-sectional areas used in the computations were 18.7 $Å^2$ for CO_2 and 16.2 $Å^2$ for N_2. The linear plots required for the BET and DR equations were obtained at relative pressure (P/P_o) ranges of 0.05 to 0.2 and 0.001 to 0.01, respectively. The surface area and pore volume distributions for the portion of the micropores penetrated by N_2 (5 to 20 Å diameter) and for mesopores (20 to 500 Å diameter) were calculated from N_2 adsorption data using the deBoer t-equation and the Barret-Joyner-Halenda (BJH) method [16]. The total pore volume for pores 5 to about 1800 Å in diameter was determined from the amount of N_2 adsorbed at 77 K at a relative pressure of 0.99.

Mercury Porosimetry

The samples were analyzed on a Micromeritics Autopore II mercury intrusion porosimeter in the pressure range of 5 to 60,000 psia that produced surface area and pore volume distributions for pores with diameters of 30 to 10,000 Å. A surface tension of 485 dynes/cm and a contact angle of 130° for mercury were used in the computations. Although, based on the particle size analyses of the samples, the 10,000 Å (1 μm) dimension was estimated to be the size of the smallest particles and thus the lower limit of the interparticle space, the presence of some interparticle space with diameters smaller than 10,000 Å cannot be ruled out.

Diffuse Reflectance Infrared Spectroscopy (DRIS)

The ground coal samples were analyzed on a computer-controlled DRIS instrument (Digilab Model 40 with diffuse reflectance attachment) for their infrared spectra. Many (5,000 to 20,000) interferograms were acquired and averaged to achieve a high signal to noise ratio. Mechanical and mathematical smoothing were not used to avoid band distortion.

RESULTS AND DISCUSSION

Surface Area and Pore Volume

Fresh Samples. Table 2 shows that the N_2-BET surface areas of the fresh samples ranged from 4 to 53 m^2/g which were less than their corresponding CO_2-DR surface areas (112-152 m^2/g). This difference can be attributed to the lower activated diffusion rate of N_2 in the micropores at 77 K compared to that of CO_2 at 273 K [17]. It is

generally assumed that the N_2-BET surface area represents the area contained in all pores having a diameter greater than about 5 Å [18], and the CO_2-DR surface area represents the entire surface area of coal [1,4,18] that, in practice, is referred to the surface area in all pores with diameters greater than 3.5 Å. In addition, CO_2 is likely to penetrate both open and closed pores through imbibition [19], thus yielding higher surface areas than N_2.

Gumkowski et al. [20] reported a N_2 surface area of 23.5 m^2/g for a sample that was obtained from the same mine as IBC-105 coal, consistent with the result on IBC-105 coal (Table 2). Machin et al. [21] reported N_2-BET surface areas ranging from 1.8 to 91.8 m^2/g for sixteen high volatile A (hvA) and high volatile B (hvB) bituminous coals from the Illinois Basin. Thomas and Damberger [22] measured N_2-BET surface areas of 1.8 to 99 m^2/g for three samples and CO_2-BET surface areas of 46 to 292 m^2/g for forty samples from Illinois mines; hvA bituminous coals had the lowest and hvC bituminous coals the highest CO_2-BET surface areas. Mercury porosimetry measurements reported by Thomas and Damberger revealed that the hvC coals contained a large number of pores with diameters of 90 to 220 Å whereas relatively few pores in hvA coale were greater than 35 Å. Previous studies [21-23] indicated that, in a given coal, vitrinite macerals have a higher microporosity and surface area than inertinite macerals. Gan et al. [18] determined N_2-BET (77 K) and CO_2-BET (298 K) surface areas of twenty six coals from various locations in the United States. One of their samples (PSOC-22) was similar to the IBC-101 coal and another one (PSOC-24) to IBC-102 coal in terms of their seam of origin and carbon content. They reported N_2-BET and CO_2-BET surface areas of 88 and 169 m^2/g, respsctively, for PSOC-22. For sample PSOC-24, they reported a N_2-BET surface area of 2.2 m^2/g and a CO_2-BET surface area of 228 m^2/g. These values are different from those for IBC-101 and IBC-102 coals reported in Table 2. This discrepancy can be attributed to differences in the methods used and variations in the properties of the samples, again demonstrating that surface area data on coals depend on experimental conditions and/or can vary from sample to sample within the same rank and seam.

Most of the N_2 surface area of the samples was assigned to mesopores (20-500 Å in diameter) (Table 2). Pores with diameters between 5 and 20 Å were referred to here as "N_2-micropores". A very small or insignificant N_2-micropore surface area suggested that either N_2 penetration into 5 to 20 Å diameter pores was physically limited or that most of the micropore surface area was derived from pores smaller than 5 Å in diameter that were penetrated by CO_2 but not by N_2.

The CO_2 surface area of the IBC-101 coal was the lowest and that of the IBC-109 coal highest among the samples (Table 2). The N_2 surface areas (mostly in mesopores) of IBC-101, IBC-102, and IBC-107 coals were considerably higher than those of the other four coals (Table 2). The IBC-103 coal, the highest rank and lowest equilibrium moisture coal (Table 1), had the lowest N_2 surface area among the eight coals (Table 2). Surface area distributions of the coals showed considerable variation from one coal to another, as illustrated by three examples in Figure 1. Surface area distributions in Figure 1 were calculated assuming average diameter of a cylindrical pore filled with N_2 in each pore size range and, therefore, the cumulative area was different from N_2-BET surface area which was based on monolayer coverage of entire surface. Most of the N_2 pore volume was derived from mesopores and macropores (Table 2). The N_2 pore volume of the fresh samples had a five-fold range (0.017 to 0.083 cm^3/g), with sample IBC-103 having the lowest value.

The above discussions regarding differences in surface area and porosity among the samples may have implications for the response of these coals to coal conversion and cleaning processes. For example, the IBC-103 coal, which has the second highest micropore surface area (as indicated by high CO_2 surface area), may resist chemical desulfurization more than the other coals because its relatively low mesopore surface area and pors volume would limit the diffusion of reacting agents into and product molecules out of the micropores. The opposite can be said for coals IBC-101 and IBC-102 which have relatively high ratios of mesopore to micropore surface areas. Raw coals possess molecular sieving capabilities to some extent, but because of their low adsorption capacity they have limited application. The IBC-103 coal could possibly be used as a "primitive" carbon molecular sieve without charring since carbons which exhibit large differences in N_2 and CO_2 surface areas are known to make good sieves for separation of O_2 and N_2 [24].

Like the gas adsorption data, mercury porosimetry measurements showed that surface area and pore volume distributions vary significantly among the samples (Table 3).

Surface areas of mesopores derived from mercury porosimetry for coals IBC-101, IBC-102, and IBC-107 were higher than those of the other four coals (Table 3), consistent with the N_2 adsorption data (Table 2). However, according to the mercury porosimetry results (Table 3), the fresh coal IBC-106 had the lowest mesopore surface area among the eight coals, inconsistent with the N_2 adsorption data (Table 2). Mercury porosimetry indicated higher surface areas and pore volumes than the N_2 adsorption method for similar pore size ranges (Figs. 2 and 3). Mercury intrusion, even at these relatively low intrusion pressures (1000-3600 psia), probably compressed the coal and, accordingly, enlarged the mesopores at the expense of micropores. Different results from the two techniques also could arise from the different equations and assumptions for each technique.

Because mineral matter comprises only a small portion of the samples and has only very small surface area and porosity, the measured surface areas and pore volumes are mostly derived from the organic matter portion of the coal. Although adjusting the values in Tables 2 and 3 for mineral matter would increase the surface areas of all the samples, the interpretations made above would not change.

Effect of Room Temperature Air-Oxidation. The CO_2 surface area of all coals, except IBC-103, increased somewhat as a result of exposure to air at room temperature for a two-month period with IBC-101 coal showing the greatest increase (Fig. 4). Although some of these changes were within the analytical error (standard error = 3%), a consistent change in only one direction suggests a real trend. The increased CO_2 surface area with air-oxidation is consistent with a controversial mechanism discussed in the literature [19]; the adsorption of CO_2 increases, at least slightly, with increased oxygen functional groups present on the coal surface.

It is interesting to note that for five of the samples, the macropore volume in pores >1800 Å decreased as a result of the exposure of the coals to room temperature air oxidation (Table 5). Although the cause of this observation cannot be determined from the present data, the oxidation and resulting increased molar volume of mineral matter disseminated in the macropores is one of the possibilities. For example, the respective molar volumes of gypsum and hematite, two oxidation products of pyrite, are 3.1 and 1.3 times that of pyrite. The unusually high pore volume for coal IBC-108 (Table 3, Fig. 3) was due to the fine particle size of this sample (<400 mesh) that caused some of the interparticle space in the sample to be counted as pore space.

Statistical Analyses

Correlation coefficients and regression plots were determined for the data on surface area, pore volume, and other coal characteristics. Because coal IBC-108 had been provided in slurry form and processed differently from the rest of the samples, it was excluded from the statistical analyses.

Figure 5 and Table 4 show that the CO_2 surface area correlated positively with apparent rank, i.e., the CO_2 surface area tended to increase with increasing heating value and decrease with increasing volatile matter and equilibrium moisture of the coals. The observed positive correlation between apparent rank and CO_2 surface area was not consistent with the general trend observed by Thomas and Damberger [22] for coals of similar carbon content. This inconsistency could be due to the fact that they used a different gas adsorption temperature (196 K vs 273 K) and a different equation (BET vs DR) to compute the CO_2 surface area. The strong negative correlation between the CO_2 surface area and organic sulfur (Table 4) is not meaningful in this case because high rank (high CO_2 surface area) and low rank (low CO_2 surface area) coals in the IBCSP originated from low-sulfur and high-sulfur mines, respectively. In contrast to the CO_2 surface area, N_2 surface area (mostly in mesopores) correlated negatively with apparent rank, i.e., it tended to decrease with increasing heating value (Fig. 5) and increase with increasing equilibrium moisture and volatile matter (Table 4).

Surface Chemical Structure

Fresh Samples. The DRIS spectra of all eight coals were found to be similar. An example of the DRIS spectra is shown in Figure 6. The sloping background curve in Figure 6 (dashed line along the lower portion of each spectrum) is a direct result of the physical scattering of the electromagnetic radiation from the coal particles. Clays in the samples gave rise to two sets of bands (Fig. 6). The hydroxyls of clays are only weakly hydrogen (H) bonded and have two vibrational bands between 3600 and 3650 cm^{-1}. The second clay band set includes three characteristic bands that are due

to lattice modes of vibration at low wave numbers.

A number of hydroxyl entities (alcoholic, acidic, phenolic, aldehydic, etc.) within the organic substrate involve H bonds of various strengths and are indicated by the large absorption band envelope from 3600 to 2000 cm^{-1} (Fig. 6). There is evidence of some preferential modes of vibration prevailed as noted in the maxima and inflection points of the DRIS spectra. Superimposed upon the hydroxyl band envelope is the composite envelope for the various organic hydrocarbons. The two envelopes can be analyzed independently if one assumes a linear baseline. A scaled-up version of the hydroxyl band envelope of Figure 6 (truncated by the uppermost dashed line as shown in the figure) is shown in Figure 7. Deconvolution of the hydroxyl band reveals five species with increasing H bond strengths in the sequence of 3547, 3399, 3314, 3020, and 2565 cm^{-1}.

The composite envelope of the various organic hydrocarbons superimposed on the hydroxyl band envelope (Fig. 6) can be deconvolved into six components (Fig. 8), and summation curve was barely distinguishable from the parent envelope. The unsaturated hydrocarbon bands (olefinic and aromatic) predictably occur above 3000 cm^{-1}, and the four bands characteristic of aliphatic modes (CH2 and CH3 groups) below 3000 cm^{-1}. A small aldehyde (-C=O) C-H vibration band occur at 2727 cm^{-1} (Fig. 6).

The absorption bands due to oxygen functional groups occur mostly in the 1900 to 1400 cm^{-1} region. The presence of carbonyls is indicated by the peak at 1700 cm^{-1} (Fig. 6). The absorption band below 1600 cm^{-1} is due to the bending modes of vibration of the respective entities in the organic substrate. The large peak at 1600 cm^{-1} is present for virtually all conjugated aromatic structures, especially if they are oxygenated to some degree. The complex, broad feature at 1100 to 1400 cm^{-1} is due to the overlap of a several bending mode bands associated with the chain and ring elements in the organic matrix.

Effect of Room Temperature Air Oxidation on Surface Chemical Structure. The exposure of the eight IBCSP coals to air at room temperature for a 2-month period did not cause any noticeable change in their DRIS spectra. An example of the DRIS spectra of the coals exposed to the room temperature air oxidation is shown in Figure 9. The interpretation of this DRIS spectrum is similar to that of a fresh sample. As in the case of fresh samples, oxygen insertion processes formed bands that appear as shoulders (inflections) on the side of the strong polynuclear aromatic peak noted as the carbonyl band (Fig. 9). Figure 10 shows the deconvolution of the carbonyl envelope. Aldehyde carbonyls show bands centered at 1664 cm^{-1}, and carboxylic acids give rise to absorption peaks centered at 1703 and 1712 cm^{-1}. The band centered at 1886 cm^{-1} is caused by a very highly oxidized state, probably aromatic anhydrides and/or aromatic carbonates. However, examination of the DRIS spectra for fresh samples (Fig. 6) shows similar signals for the oxygen functional groups already present in coal.

The surface area and pore volume data suggested that a small amount of oxidation took place upon exposure of the coals to room temperature air for a two-month period. Because coal surface is expected to adsorb a significant amount of oxygen within a relatively short period of time upon exposure to air [25], the surfaces of the fresh IBC coals were probably already oxidized during their collection in the field. During the two-month oxidation period, it is likely that the interior of the particles of the IBC coals became progressively oxidized. The oxidation that took place in the interior of the particles apparently was not detected by DRIS, which is a surface, not bulk analysis, technique. Some additional surface oxidation that might have taken place during the two-month oxidation period was apparently not significant enough to be detected by the DRIS technique. Comparing this study to past studies indicates that DRIS spectra would be affected only by oxidation processes that are more rigorous (longer exposure times and/or higher exposure temperatures) than those used for this study. Clemens et al. [14] monitored changes in surfaces of dried New Zealand coals as a result of exposure to oxygen or air at 30 to 180°C and concluded that the reactivity responsible for self-heating of these coals involved exothermic formation of hydroperoxides followed by their decomposition into carboxylic acid/aldehyde species. Pisupati and Scaroni [15] reported on the compositional and structural changes of selected bituminous coals during natural weathering and laboratory oxidation at 200 °C. They observed high concentrations of carboxylic acid and ketonic groups and reduced aliphatic hydrocarbon groups in most of their outcrop samples, and formation of ester groups in laboratory-oxidized samples, relative to those in fresh samples.

REFERENCES

1. Mahajan, O. P. and Walker, P. L., In: Analytical Methods for Coal and Coal Products, C. Karr (ed.), Academic Press, NY (1978).
2. Attar, A., and Dupuis, F., In: Coal Structure, M. L. Gorbaty and K. Ouchi (eds.), Advances in Chem. Ser., 192, Amer. Chem. Soc., Washington, D.C. (1981).
3. Palmer, S. R., Hippo, E. J., Kruge, M. A., and Crelling, J. C., In: Geochemistry of Sulfur in Fossil Fuels, W. L. Orr and C. M. White (eds.), ACS Symp. Series 429, ACS, Washington, DC (1990).
4. Gregg, S. J. and Sing, K. S. W., 1982. Adsorption, Surface Area and Porosity. Academic Press, New York, NY (1982).
5. Fuller, E. L., In: Coal Structure, M. L. Gorbaty and K. Ouchi (eds.), ACS 192, p. 293-309, American Chemical Society, Washington, D.C. (1981).
6. Marsh, H., Carbon 25, 49 (1987).
7. Sharkey, A. G. and McCartney, J. J., In: Chemistry of Coal Utilization, Second supplementary volume, M. A. Elliot (ed.), John Wiley & Sons, New York (1981).
8. Walker, P. L., Austin, L. G., and Nandi, S. P., Fuel 45, 173 (1966).
9. Kaji, R., Hishnuma, Y., and Nakamura, Y., Fuel, 64, 297 (1985).
10. Solomon, P. R., Hamblen, D. G., and Carengelo, R. M., In: Coal and Coal Products: Analytical Characterization Techniques, E. L. Fuller (ed.), ACS Symp. Series 205, ACS, Washington, DC (1982).
11. Painter, P. C., Sobkowiak, M., and Youtcheff, J., Fuel 66, 973 (1987).
12. Fuller, E. L., and Smyrl, M. R., Applied Spectroscopy 44, 451 (1990).
13. Smyrl, N. R. and Fuller., E. L., Jr., In: Coal and Coal Products: Analytical Characterization Techniques, E. L. Fuller (ed.), ACS Sym. Ser. 205, 133 (1982).
14. Clemens, A. H., Matheson, T. W., and Rogers, D. E., Fuel 70, 215 (1991).
15. Pisupati, S. V. and Scaroni, A. W., Fuel 72, 531 (1993).
16. Barret, E. P., Joyner, L. G. and Halenda, P. H., J. Amer. Chem. Soc. 73, 373 (1951).
17. Garrido, J., Linares-Solano, A., Martin-Martinez, J. M., Molina-Sabio, M., Rodriguez-Reinoso, F., and Torregrosa, R., Langmuir 3, 76 (1987).
18. Gan, H., Nandi, S. P., and Walker, P. L., Fuel 64, 272 (1972).
19. Mahajan, O. P., Carbon 29, 735 (1991).
20. Gumkowski, M., Liu, Q., and Arnett, E., Energy & Fuels 2, 295 (1988).
21. Machin, J. S., Staplin, F., and Deadmore, D. L., Illinois State Geological Survey Circ. 350, Champaign, IL (1963).
22. Thomas, J., and Damberger, H. H., 1976. Illinois State Geological Survey Circ., 493, Champaign, IL (1976).
23. Unsworth, J. F., Fowler, C. S., and Jones, L. F., Fuel 68, 18 (1989).
24. Nandi, S.P. and Walker, P.L., Jr., Separation Science 5, 441 (1976).
25. L'Homme, G. A., Pirard, J. P., and Ledent, P., In: Fundamental Issues in Control of Carbon Gasification Reactivity, J. Lahaye and P. Ehrburger (eds.), Kluwer Academic, Dordrecht, The Netherlands (1991).

ACKNOWLEDGEMENTS: This research was funded in part by the Illinois Department of Energy and Natural Resources through its Coal Development Board and Illinois Clean Coal Institute and by the U.S. Department of Energy. However, any opinions, findings, conclusions, or recommendations expressed herein are those of the authors and do not necessarily reflect the views of IDENR, ICCI, and DOE.

Table 1. Analyses of eight IBCSP Coals.

	IBC-101	IBC-102	IBC-103	IBC-105	IBC-106	IBC-107	IBC-108	IBC-109
Moisture (%)	14.7	14.2	5.7	9.4	10.4	9.3	45.0	9.2
Equil. moist (%,mmf)	16.0	15.8	6.7	16.2	11.9	16.7	-	10.8
Vol. matter (%,dmmf)	44.4	41.8	38.8	43.4	42.5	44.4	42.5	37.6
Mineral matter (%,d)	13.6	9.3	10.7	22.6	11.8	14.5	5.9	9.6
Carbon (%, dmmf)	80.1	81.7	83.4	82.1	81.5	79.6	80.6	82.8
Hydrogen (%,dmmf)	6.0	5.9	5.6	5.9	5.6	5.7	5.6	5.4
Nitrogen (%, dmmf)	1.5	1.6	1.9	1.6	1.9	1.4	1.6	1.9
Oxygen (%,dmmf)	8.8	9.7	7.8	7.8	8.8	9.8	9.8	9.2
Sulfatic sulfur (%,d)	0.05	0.06	0.02	0.00	0.01	0.26	0.01	0.0
Pyritic sulfur (%,d)	1.2	2.2	1.1	2.5	1.8	0.8	0.4	0.5
Organic sulfur (%,dmmf)	3.6	1.1	1.3	2.7	2.2	3.5	2.4	0.7
Total sulfur (%,d)	4.4	3.3	2.3	4.5	3.8	3.7	2.7	1.1
Chlorine (%,d)	0.12	0.02	0.18	0.10	0.02	0.08	0.03	0.42
BTU/lb (m,mmf)	12147	12537	13911	12334	13040	11779	-	13194
FSI	4.0	4.0	5.5	3.5	4.5	2.5	3.5	4.0
Rank	hvCb	hvCb	hvBb	hvCb	hvBb	hvCb	hvCb	hvBb
Vitr. reflect.	0.46	0.62	0.74	0.50	0.54	0.56	0.58	0.73
Vitrinite (%,dmmf)	88.3	89.9	85.7	86.7	85.7	86.6	89.6	87.4
Inertinite (%,dmmf)	6.1	4.1	8.8	10.0	7.9	8.3	7.9	7.7
Liptinite (%,dmmf)	5.6	6.0	5.5	3.3	6.4	5.1	2.6	4.9

Table 2. Surface area and pore volume of fresh and oxidized IBCSP coals (-100 mesh), as measured with gas adsorption*.

Coal Sample	CO_2 surface area(m^2/g)	N_2 surface area (m^2/g) Total	Mesopore	N_2-Micropore	N_2 pore volume (cc/g)** Total	Micropore
IBC-101	112 [135]	53 [45]	47 [42]	5.30 [3.85]	0.078 [0.071]	0.002 [0.002]
IBC-102	137 [139]	52 [44]	51 [43]	0.04 [1.14]	0.083 [0.071]	<0.001 [0.001]
IBC-103	148 [143]	4 [3]	4 [3]	0 [0]	0.017 [0.011]	0 [0]
IBC-105	116 [119]	21 [22]	18 [18]	2.73 [3.95]	0.032 [0.034]	0.001 [0.002]
IBC-106	134 [136]	27 [38]	24 [35]	1.84 [3.45]	0.040 [0.063]	0.001 [0.002]
IBC-107	120 [136]	43 [43]	39 [40]	3.85 [2.46]	0.063 [0.067]	0.002 [0.002]
IBC-108	143 [145]	16 [16]	16 [16]	0 [0]	0.026 [0.036]	0 [0]
IBC-109	152 [155]	14 [14]	13 [11]	1.69 [2.41]	0.024 [0.022]	0.001 [0.001]

* Values in brackets are for oxidized coals.
** For pores with diameters between about 5 Å and 1800 Å at a partial pressure of 0.99.

Table 3. Surface area and pore volume of fresh and oxidized IBCSP coals (-100 mesh), as measured with mercury intrusion porosimeter*.

Coal Sample	Surface area (m^2/g) 30-500 Å pores	500-1800 Å pores	1800-10000 Å pores	Pore volume(cm^3/g) 30-500 Å pores	500-1800 Å pores	1800-10000 Å pores
IBC-101	94.2 [83.5]	0.5 [0.5]	0.4 [0.4]	0.16 [0.13]	0.01 [0.01]	0.05 [0.04]
IBC-102	91.9 [84.9]	0.7 [0.6]	0.5 [0.4]	0.16 [0.14]	0.01 [0.01]	0.06 [0.05]
IBC-103	60.5 [48.9]	0.3 [0.4]	0.4 [0.3]	0.09 [0.07]	0.01 [0.01]	0.05 [0.04]
IBC-105	58.9 [65.3]	0.4 [0.4]	0.3 [0.4]	0.09 [0.10]	0.01 [0.01]	0.04 [0.05]
IBC-106	38.6 [76.6]	0.4 [0.4]	0.3 [0.3]	0.07 [0.12]	0.01 [0.01]	0.03 [0.03]
IBC-107	83.8 [78.5]	0.5 [0.5]	0.4 [0.3]	0.13 [0.13]	0.01 [0.01]	0.04 [0.04]
IBC-108	65.7 [67.4]	1.1 [1.2]	2.4 [2.0]	0.10 [0.10]	0.03 [0.03]	0.34 [0.27]
IBC-109	80.7[65.6]	0.4 [0.3]	0.3 [0.3]	0.12 [0.10]	0.01 [0.01]	0.04 [0.03]

* Values in brackets are for oxidized coals.

Table 4. Correlation coefficients for fresh -100 mesh IBCSP coals. Only correlations coefficients greater than 0.600 are included.*

Carbon dioxide surface area-		
	volatile matter	-0.948
	vitrinite reflectance	0.940
	organic sulfur	-0.925
	BTU/lb	0.837
	nitrogen content	0.814
	equilibrium moisture	-0.825
	hydrogen content	-0.784
	carbon content	0.769
	mineral matter	-0.640
	nitrogen surface area	-0.610
Nitrogen surface area-		
	equilibrium moisture	0.891
	carbon content	-0.816
	BTU/lb	-0.789
	nitrogen content	-0.778
	inertinite content	-0.712
	vitrinite content	0.710
	mercury pore volume	0.710
	volatile matter	0.717
	hydrogen content	0.699
	oxygen content	0.655
	mercury surface area	0.644
	vitrinite reflectance	-0.626
Nitrogen pore volume-		
	equilibrium moisture	0.760
	inertinite content	-0.775
	mercury volume	0.761
	vitrinite content	0.752
	nitrogen content	-0.743
	BTU/lb	-0.717
	hydrogen content	0.703
	mercury surface area	0.668
	volatile matter	0.657
	oxygen content	-0.650
Mercury surface area-		
	vitrinite content	0.794
	inertinite content	-0.632
Mercury pore volume-		
	vitrinite content	0.908
	inertinite content	-0.806

*Chemical and petrographic values are on a dry, mineral matter free (mmf) basis. Equilibrium moisture is on mmf basis. BTU/lb is on equilibrium moist, mmf basis.

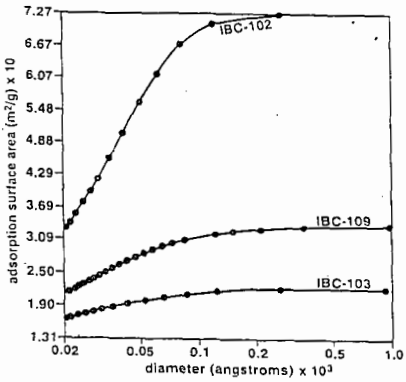

Figure 1. Cumulative surface area distribution in pores of various sizes for three of the fresh IBCSP coals as determined by the N_2 gas adsorption method.

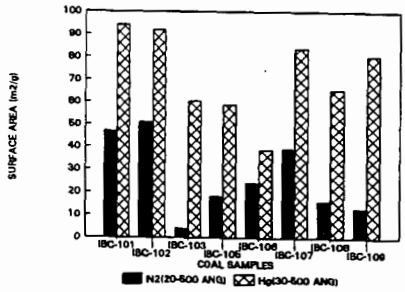

Figure 2. Comparison of surface areas of the IBCSP coals determined by N_2 adsorption and mercury intrusion methods.

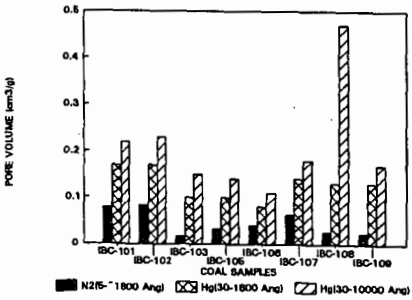

Figure 3. Comparison of pore volumes of the IBCSP coals determined by N_2 adsorption and mercury intrusion

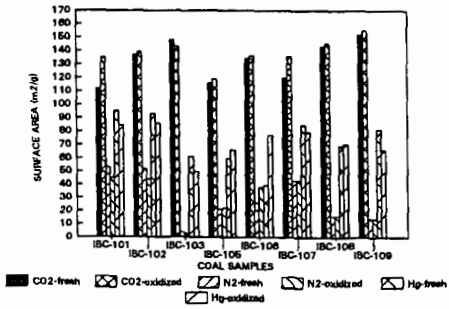

Figure 4. Effect of oxidation on the surface area of eight IBCSP coals.

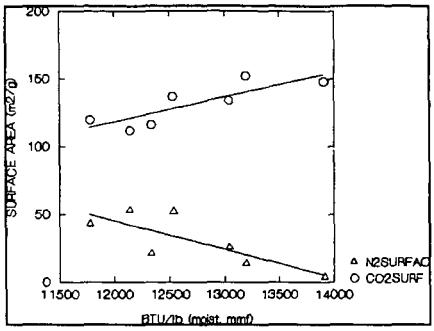

Figure 5. Variation of CO_2 and N_2 surface areas with heating value (BTU/lb) of fresh IBCSP coals.

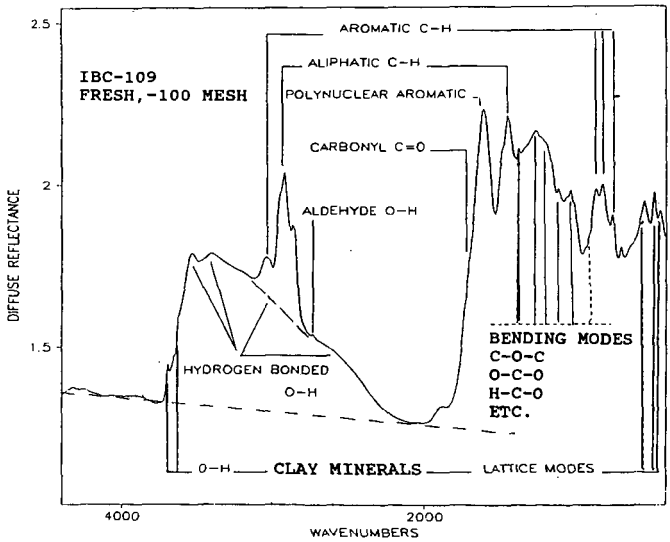

Figure 6. DRIS spectrum of fresh -100 mesh IBC-109 coal.

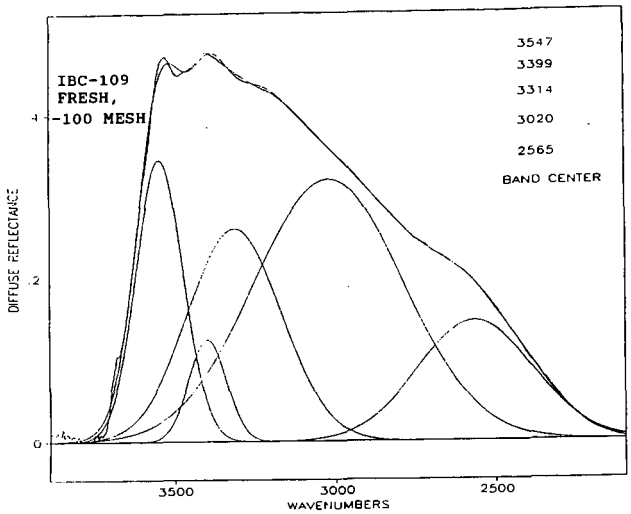

Figure 7. Deconvolution of hydroxyl band envelope of Figure 6 into its constituent components. Chi-squared of summation curve relative to parent curve=0.0204.

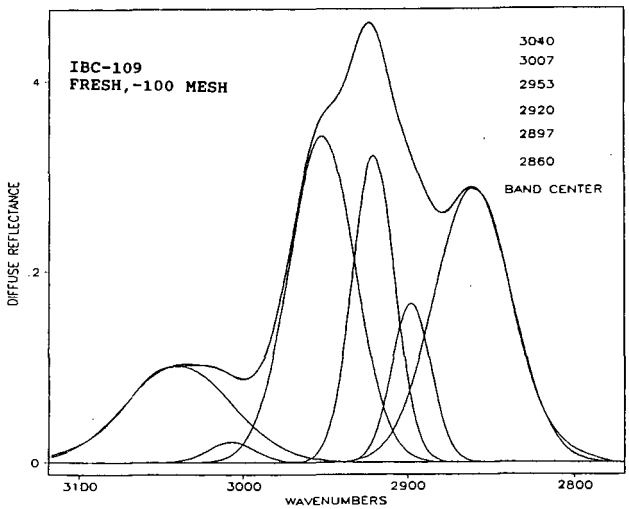

Figure 8. Deconvolution of hydrocarbon band envelope of Figure 8 into its constituent components. Chi-squared of summation curve relative to parent curve=0.000738.

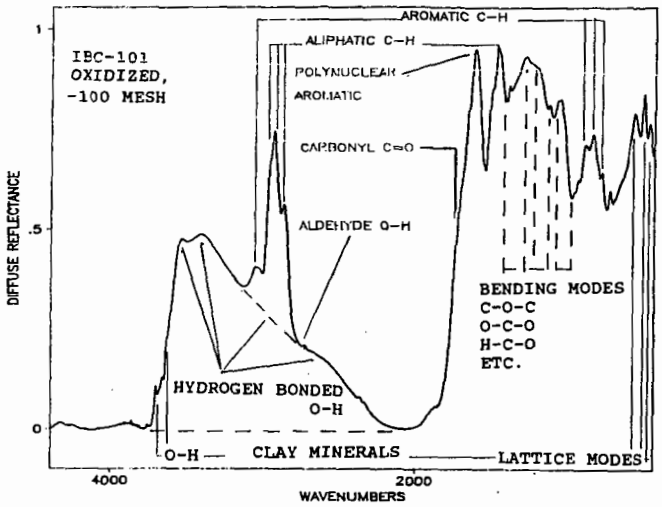

Figure 9. DRIS spectrum of oxidized -100 mesh IBC-101 coal.

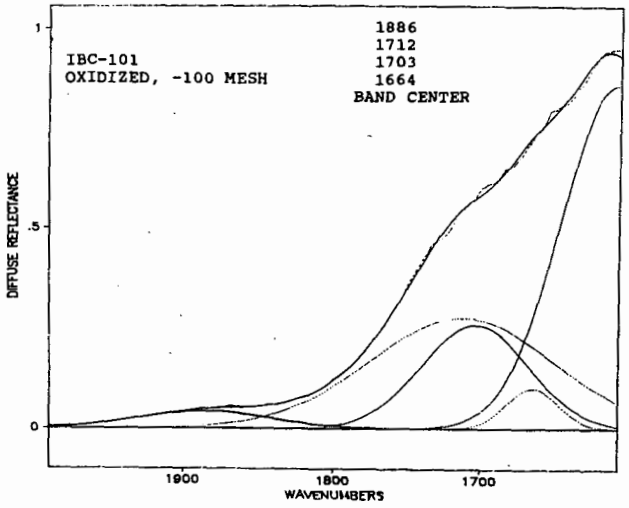

Figure 10. Band deconvolution for carbonyl region of the DRIS spectrum of the oxidized -100 mesh IBC-101 coal.

MINERAL ASSOCIATIONS IN PULVERIZED COAL

J.N. Harb, P.N. Slater and J.E. Marchek
Department of Chemical Engineering and
Advanced Combustion Engineering Research Center
Brigham Young University
Provo, Utah 84602

Keywords: Coal minerals, mineral associations, CCSEM

INTRODUCTION

Ash formed during the combustion of pulverized coal produces a variety of operational and environmental problems. Efforts to anticipate and control these problems have led to the development of mathematical models to predict mineral transformations and deposition during combustion of pulverized coal. These models require a description of the coal mineral matter as input. Advanced analytical techniques such as Computer Controlled Scanning Electron Microscopy (CCSEM) have been developed to provide the required information.

Early development of the CCSEM technique was performed by Huggins *et al.* [1] who used a scanning electron microscope equipped with a Tracor Northern 2200 X-ray analysis system to examine coal minerals. The Energy and Environmental Research Center at the University of North Dakota has developed and refined the technique for both coal minerals and ash [2]. Additional work on the association of the coal minerals with the organic matrix has been performed by Straszheim and co-workers at Iowa State University with use of a sophisticated image analysis system (LeMont Scientific DB-10) [3]. Recent work in our laboratory has examined mineral/mineral associations in coal particles [4]. This paper contains a brief description of the associations of two key minerals from two eastern U.S. bituminous coals.

ANALYSIS PROCEDURE

Computer Controlled Scanning Electron Microscopy was performed with use of a JSM-840A scanning electron microscope (JEOL) equipped with an eXL-FQAI Microanalysis System (Oxford Analytical), a Pentafet LZ5 Light Element Detector (Oxford), a LEMAS Stage Automation System (Oxford) and an ultra-thin window (MOXTEK). Samples were mounted with a mixture of carnauba wax and Cerita wax (M. Argueso & Co., Inc., Mamaroneck, NY) [5]. Carnauba wax was chosen to provide sufficient contrast between the coal and the mounting material on the backscattered electron image [6]. The Cerita wax was used to decrease sample cracking. Mounted samples were sectioned, polished, and coated with carbon.

The description of the analysis procedure which follows has been presented elsewhere and is repeated here for completeness [4]. Two automated analysis routines, Quantitative Mineral Analysis (QMA) and Analysis of Mineral and Coal Associations (AMCA), were developed. QMA was used to determine the size and composition of mineral particles by analyzing samples at magnifications of 100X and 400X. During the analysis, the sample stage was moved to predefined positions or fields where a backscattered electron image was collected. For each field, the sizes and positions of mineral particles were determined and stored. The electron beam was then moved to the center of each mineral particle and an X-ray spectrum was collected for 2 seconds (approximately 10,000 X-ray counts). Next, peak and background corrections were made. A ZAF correction was then made to account for the effects of atomic number (Z), absorption (A), and fluorescence (F) at each analysis point. The composition in weight percent was subsequently stored and the beam was moved to the next mineral particle for analysis. After analysis of all the particles in a given field, the stage was moved to the next field and the process was repeated. The results from both magnifications were then classified to identify the mineral species present, and combined off-line on a Sun computer workstation. A typical QMA analysis required approximately 12 hours of beam time to analyze 3000 to 4000 mineral particles.

The AMCA routine combined the quantitative mineral analysis with image analysis to determine the association of minerals with the coal matrix. This analysis was similar to the mineral-only analysis except that the backscattered electron images were also saved during the analysis, and the samples were analyzed at a single magnification of 220X. The stored images were later processed with use of Mineral Liberation image analysis software on the eXL, and the mounting medium, coal and minerals were identified by their respective brightness on the backscattered electron image. The amount (area) of coal and/or minerals on each particle, as well as the particle size and location were determined and stored. This information was then combined with the composition data on the mineral particles to yield the particle-by-particle mineral content for the coal. A typical AMCA analysis included about 35,000 coal and mineral particles and required approximately 24 hours of beam time in addition to off-line processing.

These procedures were used to examine two eastern U.S. bituminous coals which were recently tested in a utility boiler [7]. Ultimate and proximate analyses of these two coals are given in Table 1 [8].

RESULTS AND DISCUSSION

Table 2 shows the major mineral matter species found in the coal as determined with the QMA procedure. The weight fraction of each species was approximated from the measured area fraction with use of the species density by assuming that the volume fraction was equivalent to the area fraction [9]. As seen from the data, Coal A has significantly more pyrite than Coal B. On the other hand, Coal B has more K-Al-Silicates and more aluminosilicates than Coal A. Both pyrite and K-Al-Silicates have been identified as species which may contribute to slagging problems in boilers.

Data on the mineral content of the individual particles from AMCA were used to examine the association of specific minerals in the coal. Associations were determined by identifying particles which contained either pyrite or K-Al-Silicate minerals and then evaluating, on a frequency basis, other minerals also contained in that particle. Note that the sum of the percent association over all minerals may be greater than 100 percent since a single mineral grain may be associated with several other types of grains in the same coal particle.

Figures 1 and 2 provide association data for K-Al-Silicate and pyrite, respectively. The extent of association for the K-Al-Silicates, including the lack of association with pyrite, was similar to that of other silica-bearing minerals. In contrast, the pyrite shows a large percentage of "self-association" (i.e., pyrite present in particles with no other minerals). Analysis of the individual pyrite particles showed that 69% of the self-associated pyrite in Coal A and 57% in Coal B was present in particles which contained less than 80% mineral (area basis). In fact, a substantial fraction (31% of the self-associated pyrite in Coal A and 21% in Coal B) was found in particles containing less than 20% mineral. These data indicate that pyrite in these two coals does not tend to associate as extensively as the K-Al-Silicate minerals, and that a significant fraction (by number) of the pyrite was included or locked in the coal matrix of particles where pyrite was the only mineral present.

Results for self-associated K-Al-Silicates showed that 47% in Coal A and 27% in Coal B were present in particles which had less than 20% mineral. In other words, almost half of the K-Al-Silicate minerals in Coal A which were not associated with other minerals were included in coal particles that contained less than 20% mineral. Clearly, the fact that a mineral is self-associated does not imply that it is excluded.

Some interesting differences between the two coals can be seen in Figure 1. A higher fraction of K-Al-Silicate minerals in Coal B were self-associated. Also, a significantly lower percentage of K-Al-Silicates in Coal B were associated with quartz. A mixture of K-Al-Silicates with quartz would probably have a higher melting point than the K-Al-Silicate alone. The association of K-Al-Silicates with aluminosilicates was also lower in Coal B, in spite of the fact that Coal B contained a much higher percentage (by weight) of aluminosilicates. Coal B also contained more ash and had a higher weight percent of K-Al-Silicates in the ash (see Tables 1 and 2). Therefore, a boiler

burning Coal B may be more likely to experience deposition problems associated with K-Al-Silicate minerals which typically melt under normal combustion conditions [10].

Mineral/mineral associations were also examined as a function of the size of the mineral grains. Intuitively, one might expect larger particles to be excluded and show lower levels of association, while the smaller particles are included or locked in the coal matrix. Figure 3 shows the fraction of pyrite that was self-associated as a function of mineral size for Coal B. Included in each bar is the percent of the self-associated minerals that were excluded (i.e., in particles with greater than 80% mineral). The majority of small pyrite grains were not associated with other minerals. A large fraction of these small grains (41%) was also excluded. It is possible that fragmentation of the large excluded pyrite particles during pulverizing was responsible the presence of small excluded pyrite grains. The fraction of pyrite associated with other minerals was lowest for the larger pyrite particles.

The data for K-Al-Silicate particles were somewhat different as shown in Figure 3. The level of self-association was lower than that observed for pyrite. The level of self-association decreased with increasing mineral particle size. No self-associated K-Al-Silicate particles were found in the large size range. The percentage of the self-associated particles which were also excluded was significantly lower for the K-Al-Silicate minerals than for pyrite. Note that the size and morphology of ash formed from K-Al-Silicate minerals included in the coal matrix will probably be affected by the combustion behavior of the char (e.g. swelling vs. non-swelling).

Although the measurements and analysis presented in this paper provide insight into coal/mineral and mineral/mineral associations, the results are not without limitations. For example, the association data is based on two-dimensional cross-sections of particles which may underestimate the degree of association. The importance of this effect is currently under investigation. Also, there is a limit on the size of particle for which a reasonable composition may be obtained. Thus, the mineral data do not reflect the presence of small mineral inclusions less than about 1 micron in diameter. The statistical validity of large particle data is a problem for samples where only a few large particles are present. While these limitations may affect the magnitude of the results, they are not expected to change the significance of the key observations presented in this paper.

CONCLUSIONS

Computer Controlled Scanning Electron Microscopy has been implemented on a JEOL 840A scanning electron microscope equipped with an Oxford eXL X-ray microanalysis and image analysis system. This system was used to analyze the mineral composition of two eastern U.S. bituminous coals. In addition, a procedure was developed to determine the association of the minerals with the coal matrix and with other minerals within the coal. The mineral content of each coal was determined on a particle-by-particle basis and used to examine the association of both pyrite and K-Al-Silicate minerals in the coal. Results showed differences in the association of each of these two minerals for both of the coals analyzed.

ACKNOWLEDGMENT

This work was sponsored by the Advanced Combustion Engineering Research Center. Funds for this Center are received from the National Science Foundation, the State of Utah, 28 industrial participants, and the U.S. Department of Energy.

REFERENCES

1. Huggins, F.E., Kosmack, D.A., Huffman, G.P. and Lee, R.J., 1980, Coal mineralogies by SEM automatic image analysis, SEM/1980/I, pp. 531-540, SEM Inc., AMF O'Hare, IL.

2. Zygarlicke, C.J. and Steadman, E.N., 1990, Advanced SEM techniques to characterize coal minerals, *Scanning Microscopy*, vol. 4, no. 3, pp. 579-590.

3. Straszheim,W.E. and Markuszewski, R., 1992, Characterization of mineral matter in coal for prediction of ash composition and particle size, in *Inorganic Transformations and Ash Deposition During Combustion*, ed. by S.A. Benson, pp. 165-177, ASME, New York, N.Y.

4. Yu, H., Marchek, J.E., Adair, N.L, and Harb, J.N., 1993, Characterization of Minerals and Coal/Mineral Associations in Pulverized Coal, Proceedings of the Conference on the Impact of Ash Deposition of Coal Fired Plants, Solihull, Birmingham, UK, June 20-25, 1993 (in review).

5. Yu, H., 1992, Characterization of Mineral Particles in Coal by Computer Controlled SEM-EDS, M.S. Thesis, Brigham Young University, Provo, UT, 84602.

6. Straszheim, W.E., Younkin, K.A., Greer, R.T. and Markuszewski, R., 1988, Mounting materials for automated image analysis of coals using backscattered electron imaging, *Scanning Microscopy*, vol. 2, no. 3, pp. 1257-1264.

7. Cannon, J.N. and Webb, B.W., 1993, Seventh-Year Progress Report, Vol. II, ed. by L. D. Smoot, Advanced Combustion Engineering Research Center, Brigham Young University and University of Utah, pp. 338-349.

8. Butler, B.W., 1992, An Experimental Evaluation of Radiant Energy Transport in Particle-Laden Flames, Ph.D. Dissertation, Brigham Young University, Provo, UT, 84602.

9. Petruk, W., 1990, Measurements of mineral liberatiòn in connection with mineral beneficiation, in *Progress Mineralogy IX*, ed. by W. Petruk *et al.*, pp. 31-36, TMS-AIME, Warrendale, PA.

10. Srinivasachar, S., Helble, J.J., Boni, A.A., Shah, N., Huffman, G.P., and Huggins, F.E., 1990 Mineral Behavior During Coal Combustion 2. Illite Transformations, Progress in Energy and Combustion Science, vol. 16, no. 4, pp. 293-302.

Table 1. Properties of Coals A and B [10].

Proximate Analysis				
	Coal A		Coal B	
	% as received	% dry	% as received	% dry
Moisture	4.9	---	6.15	---
Ash	7.4	7.6	10.4	11.5
Volatile	34.95	37.25	18.75	19.40
Sulfur	2.01	2.0	1.41	1.50
Heating Value (kJ/kg)	31,249	32,714	30,470	32,123
Ultimate Analysis (%)				
	Coal A		Coal B	
Carbon	77.0	81.8	73.5	78.0
Hydrogen	3.69	3.89	4.2	4.35
Nitrogen	1.22	1.29	1.10	1.17
Oxygen	3.85	4.05	3.00	3.5
Ash Fusion Temperature Data (K)				
	Coal A		Coal B	
	Reducing Atmosphere	Oxidizing Atmosphere	Reducing Atmosphere	Oxidizing Atmosphere
Initial Deformation	2080	2310	2770	>2800
Softening	2175	2400	>2800	>2800
Hemispherical	2245	2460	>2800	>2800
Fluid	2295	2500	>2800	>2800

Table 2. Mineral particle size and composition distributions (% by weight).

Major Mineral Phases	% of Total Mineral Coal A	% of Total Mineral Coal B
Quartz	8.7	5.3
$Fe_2O_3/FeCO_3$	1.3	1.2
Aluminosilicate	38.1	54.4
Ca-Al-Silicate	0.9	0.7
Fe-Al-Silicate	0.7	0.7
K-Al-Silicate	11.5	17.8
Pyrite	30.4	14.8
$CaCO_3/CaO$	3.4	0.5
Unknown	3.1	3.3
Total	100.0	100.0

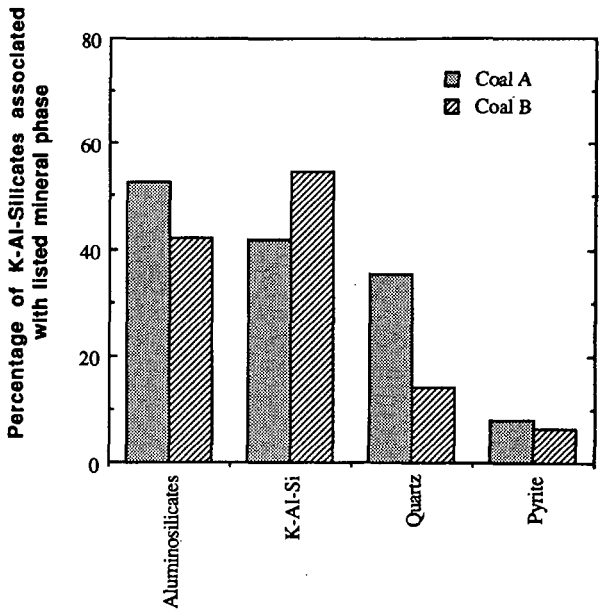

Figure 1. Association of K-Al-Silicates with other major coal minerals phases.

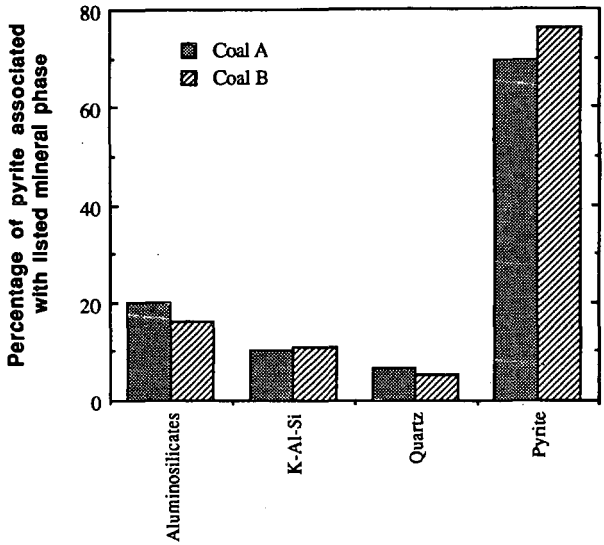

Figure 2. Association of pyrite with other major coal mineral phases.

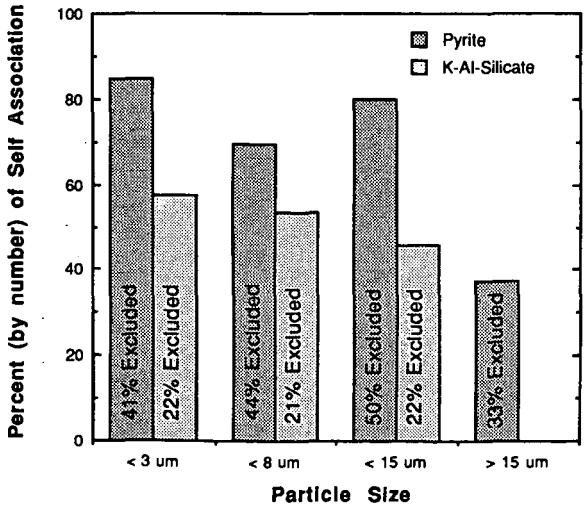

Figure 3. Extent of self-association and the percent of self-associated particles which were excluded as a function of the mineral grain size.

CHEMICAL COMPOSITION AND SIZE DISTRIBUTIONS FOR FLY ASHES

Sarbajit Ghosal, Jon L. Ebert and Sidney A. Self

High Temperature Gasdynamics Laboratory,
Department of Mechanical Engineering,
Stanford University, Stanford, California.

Keywords: fly ash, composition distribution, size distribution.

1 INTRODUCTION

The aim of this paper is twofold: to present mathematical functions to describe and store CCSEM/AIA (Computer Controlled Scanning Electron Microscopy / Automatic Image Analysis) and size data for fly ashes, and to discuss two limitations of using single-particle measurement techniques to draw general conclusions about ash properties.

Fly ash characterization is complicated by the strong inter-particle variation in morphology, diameter and chemical composition. However, with the development of microanalytical tools such as CCSEM/AIA (e.g., Barta *et al*, 1990; Steadman *et al*, 1992), diameters and chemical compositions of individual particles for statistically significant sample sizes (>1000) can now be determined with relative ease.

It is necessary to store the large amounts of data generated by CCSEM analyses in convenient forms that can be easily manipulated. In this paper, simple mathematical functions are proposed which incorporate the information in differential and cumulative forms. The functions are used to detect size-composition correlations.

Ash size distribution was measured using the Coulter Multisizer. The broad size distribution of the ash is well described by the lognormal function truncated outside the measurement limits, and the detailed size information is stored compactly using four quantities.

It is observed that CCSEM may not present a complete picture of the distribution of oxides with significant size-composition correlation because of sampling limitations. This phenomenon is illustrated for iron oxide which is preferentially present in larger ash particles. Additionally, a comparison of the size distributions obtained with CCSEM, and with the Multisizer, shows that the former tends to overpredict the median size because of an artifact associated with sample preparation.

Measurements were made on ash samples from six representative coals collected in cyclones and baghouses of pilot and full-scale power plants. These coals are Illinois #6, Kentucky #9, Upper Freeport, PA, (all three bituminous), Beulah, ND, and San Miguel, TX (both lignites), and Eagle Butte, WY (sub-bituminous). The San Miguel and the Eagle Butte ashes were obtained from full-scale power plants. The other four ashes were generated at the pilot-scale facilities of Foster Wheeler, and collected using a cyclone and baghouse in sequence. However for these four, the whole ashes could not be reconstituted due to unavailability of information on the relative proportions of baghouse and cyclone ashes. They were characterized separately with respect to their chemical, density, and size distributions. Due to space limitations, in general only one or two ashes are cited here as examples. Complete analyses for all six ashes (including a description of sample preparation techniques for CCSEM analysis) are presented by Ghosal (1993).

2 COMPOSITION DISTRIBUTION FUNCTIONS

For all six ashes, 1000–1800 particles were selected at random by the CCSEM software. Their diameters were measured and their compositions analyzed with respect to the following twelve elements: Si, Al, Fe, Ca, Mg, Na, K, Ti, Ba, S, P, and Cl. For such sample sizes, the numbers of particles detected per micron-bin drop sharply and steadily for diameters $\gtrsim 5\ \mu m$. In general, it was seen that particles with diameter $<8\ \mu m$ constitute $\gtrsim 90\%$ of the sample. However, the larger diameter bins contain insufficient numbers of particles, and should not be considered for drawing conclusions on size-composition relationships. A minimum population of twenty-five particles per micron-bin was arbitrarily chosen to determine the upper diameter limit, D_{25}.

Ash samples (40–50 g each) were melted and quenched rapidly to form glassy slags. Polished samples were prepared for chemical composition analysis using electron microprobe. Appropriate detectors and standards were used to measure the concentrations of the above twelve elements. Because each slag is prepared from a large ash sample, the analysis accurately yields the bulk (average) composition of the ash. The elemental compositions from both CCSEM and microprobe data were converted to oxide compositions using the following formulae: SiO_2, Al_2O_3, Fe_2O_3, CaO, MgO, Na_2O, K_2O, TiO_2, BaO, SO_3, and P_2O_5.

The mineral matter in coal is present in equilibrium, crystalline phases, generally having fixed compositions. However, the composition distribution of the ash particles is much more continuous. This is a result of the complex formation process, whereby the mineral inclusions melt, coalesce, and cool rapidly to form (primarily) spherical glassy ash particles. Hence, it is appropriate to use mathematical functions to describe inter-particle compositional variation. The following functions are proposed to describe the composition distribution for a single ash particle, and also to determine size-composition relationships.

1. The function, $c_o(D)$, is defined so that $c_o(D)\,\mathrm{d}D$ represents the mass fraction (or %) of oxide o present in particles with diameters between D and $D + \mathrm{d}D$. Integrating $c_o(D)$ over all diameters yields the average mass fraction of oxide o in the ash.

2. The second function $\xi_o(x, D)$ is defined so that $\xi_o(x, D)\,\mathrm{d}x\,\mathrm{d}D$ represents the volume fraction of ash with mass fraction of oxide o between x and $x + \mathrm{d}x$ made up of particles with diameters between D and $D + \mathrm{d}D$.

3. Finally, there is a function, $\zeta_o(x)$, such that $\zeta_o(x)\,\mathrm{d}x$ represents the number fraction of ash particles with mass percentage of oxide o between x and $x + \mathrm{d}x$.

A convenient way to study size-composition relationships is to use a cumulative function, $C_o(D)$, defined as

$$C_o(D) = \frac{\int_0^D c_o(x)\, x^3\, \mathrm{d}x}{\int_0^D x^3\, \mathrm{d}x}$$

Thus, $C_o(D)$ is the average mass fraction of oxide o for all ash particles with diameters less than D. Figure 1 shows the distribution $C_o(D_{25})$ for the Illinois and Beulah ashes. The cumulative number distribution, $F_0(D)$, shows the fraction of the sample included in calculating $C_o(D)$. The magnitude of the slope of $C_o(D)$ indicates the magnitude of size-composition correlation.

Among all six ashes, it is noted that only two, Illinois #6 and Kentucky #9 (not shown here), have an average Fe_2O_3 content $>5\%$. While the iron content showed a small decrease with increasing diameter for the Illinois and Kentucky ashes over the whole size range, it showed no dependence on size for the other four. Similarly, CaO showed a very small decrease with increasing diameter for some of the ashes. In general, the $C_{Al}(D)$, $C_{Fe}(D)$, and $C_{Ca}(D)$ graphs are flat, indicating that there is negligible correlation between particle size and composition.

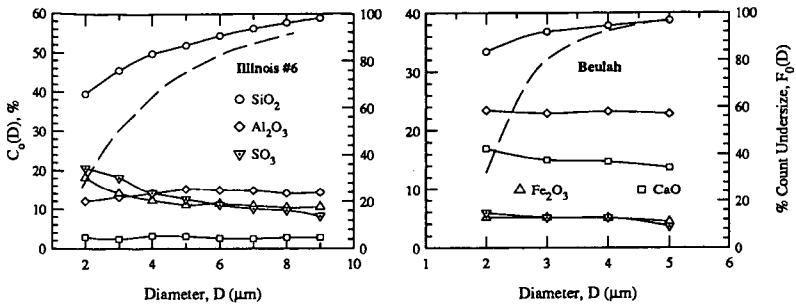

Figure 1: Cumulative undersize composition distribution. The right hand axis shows the count undersize, which is graphed as a dashed line.

Consistent size-composition trends are shown by sulfur and silica. The sulfates are deposited preferentially on smaller particles which confirms earlier reports (e.g., Ramsden and Shibaoka, 1982). However, the size-dependence of SO_3 is strong in some ashes (e.g., Illinois #6) and weak in others (e.g., Beulah). The positive size-concentration relationship for SiO_2 is noted in five of the six ashes, with the exception of the atypical calcia- and alumina-rich Eagle Butte ash. As discussed later, many of the large ash particles ($D \gtrsim 10\ \mu m$), not detected here, are relatively iron-rich. Hence, the slope of $C_{Fe}(D)$ can be expected to increase significantly at larger diameters. Similar observations with respect to size and composition relationships for the major oxides are reported by Mamane *et al* (1986) who studied Al/Si distribution as a function of particle diameter, and Hemmings and Berry (1986) who analysed the average composition of size-classified ash derived from sub-bituminous coal.

The distribution of the oxides in the ash volume can be expressed on a cumulative basis by integrating $\xi_o(x, D)$ in the following manner

$$f_o(x) = \int_0^x \int_0^{D_{25}} \xi_o(x', D)\, \mathrm{d}D\, \mathrm{d}x'$$

Here, $f_o(x)$ is the volume fraction of ash with mass percent of oxide o less than x. Particles with $D > D_{25}$ are omitted. When x=100%, $f_o(x)$ is unity for each of the oxides. Figure 2 presents $f_o(x)$ for the Illinois and Beulah ashes, and its interpretation gives some useful information. Large or small slopes over an increment of Δx implies the presence of a large or small proportion of particles with oxide content between x and $x + \Delta x$, respectively. Among all oxides, silica is distributed most broadly (i.e., with the largest range of mass fractions), with Illinois ash having the broadest $f_o(x)$.

Both Kentucky and Illinois ashes are found to contain a significant volume fraction of silica-rich particles (i.e., >80% SiO_2). Although Al_2O_3 is one of the two most predominant oxides, there are no alumina-rich particles (i.e., $\gtrsim$ 60%). For iron, it is seen that 90% of the ash volume contains $\lesssim$ 8% of iron (by mass) for all the ashes, with the exception of Illinois #6 (which has a broader distribution with only 65% of the ash volume containing <8% of Fe_2O_3). Hence, for all ashes except Illinois #6, the fraction of ash volume containing a wide range of Fe_2O_3 mass fraction (20%–50%) is negligible. The distribution of CaO is similar to that of Fe_2O_3 in most of the ashes, except in Eagle Butte ash (not shown here) where it is the main constituent, and resembles the Al_2O_3 distribution of the other ashes. The four oxides shown are clearly the major constituents since, for all ashes, only 10% of the ash volume is seen to contain more than 10% of the other oxides by mass.

Representation of ash composition as cumulative distribution functions, as presented in Figure 2, represents significant reduction of the overall data size. For example, for twelve oxides, one could tabulate

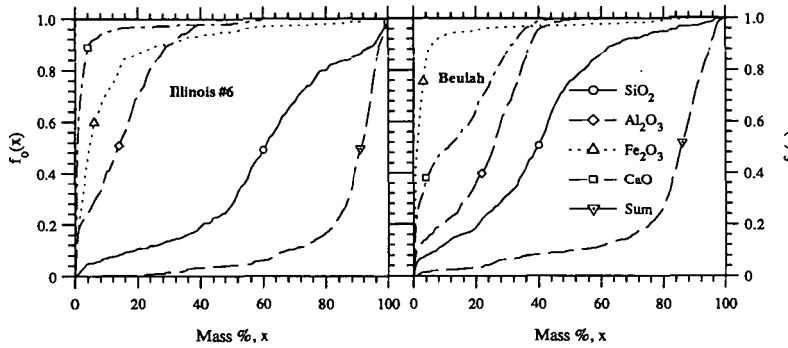

Figure 2: Volume-composition distribution shown on a cumulative basis. $f_o(x)$ represents the volume of ash with mass fraction of oxide o less than x%, as a fraction of the total volume.

$f_o(x)$ at 1% intervals for a total of 1200 stored values (many of which are zero since many of the minor oxides occur in only trace amounts). Alternatively, these distribution functions may be fitted with appropriate polynomials if additional data compression is desired.

The primary limitation of this scheme is that it does not allow for correlation between the various species, or with particle size. As illustrated in Figure 1, the correlation between composition and size is not significant for the ashes studied here. Analysis of the linear correlation coefficient, R, for the twelve oxides revealed that there are generally no significant correlations between any two oxides, although BaO and TiO_2 were exceptions with $R \simeq 0.7$ for the Illinois #6 ash.

3 IRON DISTRIBUTION IN ASHES

An average ash composition, ϑ_o, was obtained by combining the CCSEM data with the volume distribution, $F_3(D)$, obtained from the Multisizer data (Ghosal, 1993). For all ashes, it was found that $1\% < \vartheta_{Fe} < 13\%$ (Table 1), which is only 25%–70% of that determined by microprobe analysis. The reason for this discrepancy appears to be statistical. Size measurements of the iron-rich ash fractions, separated into classes by centrifugal separation (Ghosal, 1993), show that they have significantly higher median diameters than that of the whole (unseparated) ash. Consequently, they are fewer in number, and a typical CCSEM sample size of one or two thousand particles is not statistically large enough to detect sufficient numbers of such particles, in contrast to the microprobe data which is averaged over a large sample.

It is noted that a large CCSEM sample is needed for an accurate estimate of the average iron content even if iron distribution is not weighted in favor of larger particles because Fe_2O_3 constitutes <20% or less of the ash mass. Simple statistical analyses suggest that a sample size of >15,000 particles is needed for estimating the *bulk* iron content of the Kentucky ash with a confidence interval of 0.5% (Ghosal, 1993). Nevertheless, CCSEM analyses provides useful information about iron distribution among the smaller ash particles ($D \lesssim 7\ \mu m$).

Table 1: Average Fe_2O_3 content of ashes (by mass) obtained from CCSEM and electron microprobe analyses illustrating the underprediction of the iron content from CCSEM data.

Fly Ash	CCSEM, ϑ_o	Microprobe	Ratio, ϑ_o/Microprobe
Kentucky #9	6.9%	12.59%	0.55
Illinois #6	13.0%	18.96%	0.69
Upper Freeport	4.8%	13.05%	0.37
Eagle Butte	3.1%	6.88%	0.45
Beulah	4.6%	16.88%	0.27
San Miguel	1.2%	2.75%	0.44

4 ASH SIZE DISTRIBUTION

Fly ash has a broad size distribution with diameters spanning more than three orders of magnitude. Hence, it is important to measure the dispersion of the size distribution (i.e., the standard deviation). In the few references giving size data (e.g., Fisher, *et al*, 1978; Wall, *et al*, 1981; Hemmings and Berry, 1986), only median diameters are discussed. Furthermore, a suitable mathematical function is needed to describe the size distribution. Such a function allows for comparison of various ashes, and are also needed for computation of properties of ash aerosols, e.g., radiative properties (Ghosal and Self, 1993).

A method for accurate measurement of ash size distribution (for particle diameters $\gtrsim 1\ \mu m$) using the Coulter Multisizer is presented by Ghosal *et al* (1993). For powders (such as fly ash) with size distributions that are typically very broad and skewed toward small particles, lognormal functions are commonly used to describe the size distributions (Crow and Shimizu, 1988). However, because of lack of size information outside the measurement limits set by the dynamic range of the Multisizer, the data are fitted to a function truncated outside the measurement limits (a, b). The form of this truncated lognormal distribution function, characterized by a number median diameter, D_n, and a geometric standard deviation (GSD), σ_g, is shown below:

$$\frac{dF^{(a,b)}(D)}{d(\ln D)} = \frac{\frac{1}{(2\pi)^{1/2}\ln\sigma_g}\exp\left[-\frac{1}{2}\left(\frac{\ln D/D_n}{\ln\sigma_g}\right)^2\right]}{\int_{\ln a}^{\ln b}\frac{1}{(2\pi)^{1/2}\ln\sigma_g}\exp\left[-\frac{1}{2}\left(\frac{\ln x/D_n}{\ln\sigma_g}\right)^2\right]d(\ln x)} \qquad a \le D \le b$$

The surface area and volume distributions are the second and third moments, respectively, of the above number (or count) distribution. All have the same value of σ_g. Thus, if one median diameter and σ_g are known, the other two can be calculated (Crow and Shimizu, 1988). In this manner, detailed information on the ash size distribution can be stored compactly using four quantities: D_v, σ_g, a, and b. For example, for the Upper Freeport ash, these numbers are 9.3 μm, 2.76, 1.2 μm, and 60 μm, respectively. The median diameters by number count and area are respectively D_n=0.4 μm and D_a=3.3 μm.

The above function was found to fit the size data very well, and the best-fit values of median diameters and GSD are shown in Table 2. The values of D_v and σ_g tend to fall in the ranges of 9–15 μm and 2.0–3.0, respectively with one exception. The San Miguel lignite ash, which is highly cenospheric, contains many large particles, and its D_v is two to three times larger than that of the other ashes. For many of the ashes, the values of D_n are below the lower limit of measurement, and the number of particles detected in each Multisizer size channel continues to increase with decreasing diameter. Best-fit parameters calculated for the data of Wall *et al* (1981) were found to be D_v=10.5 μm and σ_g=2.95, within the ranges observed in this study.

Table 2: Size parameters for best-fit lognormal functions used to represent the size distributions of the fly ashes studied. The truncation limits, (a, b), are (1.2 μm, 180.0 μm) for the San Miguel ash, and (1.2 μm, 60.0 μm) for the remaining ashes.

Fly ash	Coal Type	Collection	D_n	D_a	D_v	D_{32}	σ_g
Kentucky #9	Bituminous	Baghouse	1.2	5.1	10.4	7.3	2.33
Kentucky #9	Bituminous	Cyclone	3.4	9.4	15.6	12.1	2.04
Illinois #6	Bituminous	Baghouse	0.4	3.4	10.1	5.8	2.85
Illinois #6	Bituminous	Cyclone	2.3	7.9	14.6	10.7	2.19
Beulah, ND	Lignite	Baghouse	0.4	3.9	12.7	7.0	2.98
Beulah, ND	Lignite	Cyclone	1.2	5.4	11.5	7.9	2.39
Upper Freeport, PA	Bituminous	Baghouse	0.4	3.3	9.3	5.6	2.76
San Miguel, TX	Lignite	ESP	1.1	10.5	32.3	18.4	2.89
Eagle Butte, WY	Sub-bituminous	Baghouse	0.6	5.0	14.3	8.4	2.80

4.1 Comparison of CCSEM Size Distribution with Multisizer Data

The geometric diameters of ash particles are determined using an image analyzing program that computes the average length of eight 'chords' passing through the 'center' of the particle as determined by an appropriate algorithm. Size distributions were computed from this data. The cumulative undersize form of the lognormal distribution plots as a straight line on a log-probability graph. However, for the truncated function, there is a departure from the straight line at the large and small diameter limits. The volume distribution obtained from the CCSEM data is plotted along with the Multisizer distribution for the Kentucky #9 ash in Figure 3.

It is virtually impossible to prepare a fully deagglomerated ash sample for CCSEM. The freeze-drying method used here (Ghosal, 1993) produces well-deagglomerated samples with very few particle clusters per SEM frame (which were rejected by limiting the acceptable range of shape factors). However, these few ash particle clusters typically consist of numerous small ash particles (1–5 μm) attached to one or two larger particles. Consequently, there is a deficit of small fly ash particles among those analyzed by CCSEM. The Multisizer data shows that D_v from CCSEM data is about 40% larger than that of the Multisizer distribution. No study of the effect of sample preparation on CCSEM size distribution could be located in the literature.

The difference in the two distributions in the large diameter ranges is due to statistical reasons. Because of the much larger sample size, the large ash particles are better represented in the Multisizer sample (>150,000 particles) than in the CCSEM sample (≈1000 particles). The Multisizer sampled 23 particles of diameter >50 μm. Using this data, it is seen that a random CCSEM sample size of ≈4000 particles is necessary to encounter one particle of diameter >50 μm. Additionally, it is possible that some of these 'rare' large particles are rejected as part of agglomerates.

These artifacts explain the departure of the CCSEM curve from the Multisizer curve in the smaller and larger diameter ranges, respectively. While the median diameter from SEM data depends on which of the factors predominates[2], the standard deviation is necessarily smaller because the range of particles examined is narrower. Hence, the slope of the size distribution is slightly steeper compared to the Multisizer distribution for each ash (Figure 3). These observations illustrate the limitations of measuring size distributions of powders with a broad size range using microscopes. It may account for discrepancies between ash size distributions measured using SEM and Coulter Counter reported by Fisher *et al* (1978),

[2]For the Kentucky #9 ash, the effect of the shortage of small particles predominates.

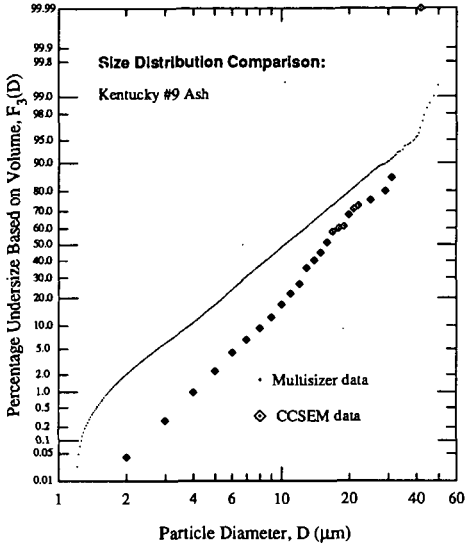

Figure 3: Comparison of Kentucky #9 ash size distribution obtained with Coulter Multisizer measurements (combining data obtained using 30 μm and 100 μm orifices) with CCSEM size data.

between ash size distributions measured using SEM and Coulter Counter reported by Fisher *et al* (1978), but not explained.

5 SUMMARY AND CONCLUSIONS

Although chemical composition measurement on a particle-by-particle basis using CCSEM confirmed significant inter-particle variation, correlation between size and composition is seen only for SiO_2, and SO_3. This observation is valid for ash particles with $D \lesssim 8\ \mu m$, which comprise over 90% by number, and ≈50% by volume, of the ashes in general. From this and other studies (see Ghosal, 1993), it was found that a large fraction of the iron is concentrated in relatively few, large particles. Thus, to get comprehensive and statistically reliable data using currently feasible CCSEM sample sizes, it appears necessary to perform CCSEM on accurately size-classified ashes.

Mathematical functions were used to describe oxide distributions in the ash. Cumulative distribution functions provide a means of representing the large volume of CCSEM data in a more compact form. The loss of oxide-to-oxide composition correlation associated with this representation is not important for many applications, such as characterization of the optical properties of fly ash.

Accurate size measurements made with the Coulter Multisizer showed that a truncated lognormal function describes the ash size distribution quite well. The differences between the size distributions obtained using the Multisizer and CCSEM are explained in terms of artifacts related to the SEM sample preparation technique, and statistical limitations imposed by sample size.

Acknowledgements: This work was supported by DOE under contract number DE-AC22-87PC 79903. The CCSEM measurements were made at the Energy and Environment Research Center of Grand Forks, ND.

References

[1] Barta, L. E., *et al*, 1990, "A Statistical Investigation on Particle to Particle Variation of Fly Ash Using SEM-AIA-EDAX Technique", *Material Research Society Symposium Proceedings*, Vol. 178, pp. 67–82.

[2] Crow, E. L., and Shimizu, K., 1988, *Lognormal Distributions*, Marcel Dekker Inc., New York.

[3] Fisher, G. L., *et al*, 1978, "Physical and Morphological Studies of Size-Classified Coal Fly Ash", *Environmental Science and Technology*, Vol. 12, No. 4, pp. 447–451.

[4] Ghosal, S. (1993), "Optical Characterization of Coal Fly Ashes and Infrared Extinction Measurements on Ash Suspensions", Ph. D. thesis, Mechanical Engineering Department, Stanford University, Stanford, CA 94305.

[5] Ghosal, S., and Self, S. A., 1993, "Optical Characterization of Coal Fly Ash", presented at the 29th ASME/AIChE National Heat Transfer Conference, Atlanta.

[6] Ghosal, S., Ebert, J. L., and Self, S. A., 1993, "Fly Ash Size Distributions: Use of Coulter Multisizer and Fitting to Truncated Lognormal Distributions", *Particle and Particle Systems Characterization*, Vol. 10, pp. 11–18.

[7] Hemmings, R. T., and Berry. E. E., 1986, "Speciation in Size and Density Fractionated Fly Ash", *Material Research Society Symposium Proceedings*, Vol. 65, pp. 91–104.

[8] Mamane, Y., Miller, J. L., and Dzubay, T. G., 1986, "Characterization of Individual Fly Ash Particles Emitted from Coal and Oil-Fired Power Plants", *Atmospheric Environment*, Vol. 20, No. 11, pp. 2125–2135.

[9] Ramsden, A. R., and Shibaoka, M., 1982, "Characterization and Analysis of Individual Fly Ash Particles from Coal-fired Power Stations by a Combination of Optical Microscopy, Electron Microscopy and Quantitative Electron Microprobe Analysis", *Atmospheric Environment*, Vol. 16, No. 9, pp. 2191–2206.

[10] Steadman, E. N., *et al*, 1992, "Coal and Ash Characterization: Digital Image Analysis Applications", in *Inorganic Transformation and Ash Deposition During Combustion*, Ed: S. A. Benson, ASME, New York.

[11] Wall, T. F., *et al*, 1981, "Fly Ash Characteristics and Radiative Heat Transfer in Pulverized-Coal-Fired Furnaces", *Combustion Science and Technology*, Vol. 26, pp. 107–121.

SIZE-RELATED VARIATIONS IN COAL FLY ASH COMPOSITION AS DETERMINED USING AUTOMATED SCANNING ELECTRON MICROSCOPY

K.A. Katrinak and C.J. Zygarlicke
Energy & Environmental Research Center, University of North Dakota
Grand Forks, North Dakota 58202-9018

Keywords: individual-particle analysis, scanning electron microscopy, coal fly ash

ABSTRACT

A new preparation method for fly ash samples has enabled characterization of particles as small as 0.1 μm in diameter, an order of magnitude less than the lower size limit of 1 μm previously used for automated scanning electron microscopy. The method involves freeze-drying an ash dispersion on vitreous carbon, which provides a very low-contrast background. The smallest particles can thus be imaged and then analyzed using energy-dispersive x-ray spectrometry. Individual particles in this extended size range have been characterized using ash produced through bench-scale combustion of Eagle Butte and Eagle Butte/Kentucky No. 9 blend coals. Distinct size-related compositional variations are evident. Supermicron particles consist largely of calcium- and aluminosilicate-rich minerals. The submicron fraction is dominated by sulfate-, phosphate-, and chloride-rich particles, probably formed through condensation. Their unique composition indicates the importance of including these smallest particles in ash characterization.

INTRODUCTION

Scanning electron microscope analysis of coal and ash samples yields size and composition data on a particle-by-particle basis, information critical in predicting inorganic transformations during combustion. Through automated techniques, hundreds to thousands of individual particles can be chemically analyzed using energy-dispersive x-ray spectrometry and image processing. A minimum of operator effort is thus required to achieve a statistically significant characterization of the sample.

Electron microscope techniques are commonly applied to coal mineral and ash particles with minimum diameters of 1 μm. However, individual-particle analysis is also important for submicron ash particles, which form during combustion from both organically associated elements and from minerals in coal.

Organically associated elements in low-rank coals, including Na, Mg, and Ca, and, to a lesser extent, K, Fe, and Al, commonly vaporize during combustion. Na, Mg, and K are particularly volatile and can condense homogeneously as submicron particles if the ratio of vapor-phase alkali elements to ash surface area is large. These particles usually react with SO_2 to form submicron sulfate particles by the time they reach the outlet of the boiler.

Mineral particles in coal undergo much less vaporization and condensation during combustion. The extent of vaporization depends on the composition of the local gas. If air is not vigorously mixed with the burning coal particles, reducing zones can exist in the flame. Within the reducing zones, SiO_2 can be reduced to SiO, which is volatile. In cooler zones of the furnace, the SiO vapor will oxidize and condense as small SiO_2 particles in much the same way as the vaporized Na species.

Submicron particles can also be produced through size reduction of larger mineral particles when decomposition or fragmentation occurs during heating. When rapidly heated, pyrite fractures and, upon partial oxidation, forms FeS fragments before melting at 1075°C (1). Calcite ($CaCO_3$), siderite ($FeCO_3$), and ankerite ($CaFe[CO_3]_2$) also fragment upon decomposition to form submicron particles (1).

Once formed, submicron particles are difficult to remove from the flue gas stream. When emitted, these fine particles contribute far more to plume opacity per unit mass than do larger particles (2). The effect of the fine particles on plume opacity is maximized because their size distribution peaks near a diameter equal to the wavelength of visible light, the particle size with the greatest amount of scattering per unit mass (3, 4). Understanding of the composition and formation of submicron particles is thus important in mitigating particulate emissions.

Submicron particles are difficult to analyze with automated techniques because their small size places them near the imaging and analytical detection limits of the conventional scanning electron microscope. Using a new sample preparation method involving freeze-drying, individual ash particles with diameters as small as 0.1 μm can be analyzed automatically in the Tracor-Northern automated digital electron microscope (ADEM). The new technique is termed scanning electron microscopy with image analysis (SEM-IA) and is generally similar to computer-controlled scanning electron microscopy (CCSEM). The technique and test results are described below.

METHODS

Sample Preparation. Coal fly ash was produced in a bench-scale drop-tube furnace, as described elsewhere (5). Samples were prepared by freeze-drying a small amount of dispersed particles onto a substrate of vitreous carbon (6). Vitreous carbon is used because its exceptionally smooth surface allows unambiguous identification of small particles. Freeze-drying maintains a uniform separation between particles.

Data Acquisition. The Tracor-Northern ADEM is used for SEM-IA of the freeze-dried sample preparations. It has a spatial resolution of 0.1 μm, allowing analysis of the smallest ash particles. A low accelerating voltage (7 kV) is used to keep the excitation volume within the particles and to improve imaging. Secondary electron imaging (at 10,000x magnification) and derived binary images are used to locate and measure the size of each particle. The image analysis consists of acquiring 25 digital images of each field of view, then averaging them to remove noise.

After an average image has been formed, individual ash particles are automatically sized, then analyzed for chemical composition using energy-dispersive x-ray spectrometry (EDS). The system is configured to detect Na, Mg, Al, Si, P, S, Cl, K, Ca, Fe, Ba, and Ti. Spectra are acquired for 15 seconds at 300 pA. A relatively low beam current is used to minimize sample damage. Spectra collected using these parameters generally contain sufficient x-ray counts to identify the elemental composition of most submicron particles. The use of a low accelerating voltage results in decreased detection efficiency for many metals, but this does not detract from the analysis of typical submicron particles.

Region-of-interest (ROI) integrated counts and particle-sizing information is saved in the ADEM computer as each field of view, containing approximately 20 individual ash particles, is completed. The light loading of particles is necessary to prevent electron beam overlap onto adjacent particles during analysis. Currently, only approximately 200 particles per sample are analyzed because of the operator time required to manually select each field of view.

Data Reduction. After each sample analysis is complete, the data files are transferred to the Tracor-Northern TN-8500 computer and reduced using the same routines applied to CCSEM data (7). The particle classification program PARTCHAR, developed at the University of North Dakota Energy and Environmental Research Center, was modified to apply more specifically to submicron particles through the inclusion of more sulfate-, phosphate-, and chloride-bearing types and fewer metal-rich types.

RESULTS AND DISCUSSION

Fly ash samples produced from Eagle Butte coal and from a blend of Eagle Butte (70%) and Kentucky No. 9 (30%) coals were analyzed to test the SEM-IA method. The tests were designed to investigate any sampling bias and to compare SEM-IA with CCSEM results for identical samples.

Morphology. Visual inspection of the freeze-dried sample preparations in the ADEM shows that many submicron particles are present. In some instances, several submicron particles are fused together, forming irregularly shaped aggregates. Such aggregates are common in fly ash and probably form at elevated temperatures prior to emission (8, 9). Alternatively, vapor-phase condensation may have occurred following aggregation, smoothing the spherule surfaces together through deposition of coatings. No attempt was made to break up these aggregates, as this would alter the size distribution of the original sample.

Test of Sampling Bias: Eagle Butte Ash. It is possible that operator selection of fields of view could result in overrepresentation of the smallest particles. However, large agglomerated groupings of particles are sometimes present in the sample preparation (probably the result of overloading the sample suspension), and so some operator discretion is necessary. A single freeze-dried preparation of Eagle Butte fly ash was analyzed twice using the SEM-IA method: first using fields of view selected because they contained relatively high proportions of submicron particles, then using randomly selected areas.

Size distributions for the two runs are shown in Figure 1. The results were similar, with both size distributions peaking at a particle diameter of 0.4 μm. The run emphasizing submicron particles has a second peak at a particle diameter of 25 μm, indicating large particle agglomerates were encountered in the areas analyzed. As mentioned above, these agglomerates are an artifact of the sample preparation procedure. The agglomerates are readily identified by their size distribution curve, which is distinctly separate from the curve representing the submicron particles and can easily be removed from the data set after the analysis is completed.

The results of these two runs suggest that the true size distribution of the sample is accurately measured by the SEM-IA method. The peak at diameter 0.4 μm may indicate a uniformity of ash formation processes leading to a consistent particle size.

Comparison of SEM-IA and CCSEM Methods: Eagle Butte Ash. In order to directly compare SEM-IA and CCSEM results, the same freeze-dried dispersion of Eagle Butte fly ash was analyzed using both SEM-IA and CCSEM. In addition, a standard dispersion of the same ash sample was prepared and analyzed using CCSEM. Results are shown in Table 1. Particle compositions for the SEM-IA and CCSEM analyses are completely different, whereas the results for the two CCSEM runs are similar. Particles detected using SEM-IA are predominantly sulfate-, phosphate, and chloride-rich, whereas those detected through CCSEM represent an assortment of minerals, mostly Ca-rich, including Ca aluminate, Ca silicate, gypsum/Al-silicate, Ca-Al-silicate, and others. A minor number of sulfate-rich particles were also detected through CCSEM.

The compositional variations between the SEM-IA and CCSEM data sets reflect the different size ranges represented by the two types of analyses. In the SEM-IA run, the maximum particle diameter in Table 1 was 1.6 μm. Large agglomerates, with diameters of 25 μm and greater, are sample preparation artifacts and were not included in the table. The CCSEM analyses include only particles with diameters >1 μm, and so most of the particles detected using SEM-IA would not be included in the CCSEM results.

It is less clear why the SEM-IA results do not include many particles with diameters in the low end of the CCSEM size range, i.e., those with diameters of 2 to 10 μm. Apparently the fields of view selected for SEM-IA analysis contained few or no particles in this range, in contrast to the areas used for CCSEM. Only a very small area of the sample was used to obtain data for 226 particles

through SEM-IA. The CCSEM analysis of the same freeze-dried preparation included a much larger area (at lower magnification), yielding data for 453 particles. The CCSEM analysis of the standard dispersion included 1013 particles. In the future, SEM-IA runs will be lengthened to make them more directly comparable with CCSEM analyses.

The distinct compositional variation between the submicron size fraction (as measured using SEM-IA) and the supermicron fraction (measured using CCSEM) confirms that they are formed through different processes. Condensation of alkali vapors is evidently the primary mechanism for formation of submicron particles, while the mineral-rich content of the supermicron particles indicates they probably formed through decomposition and fragmentation.

Comparison of SEM-IA and CCSEM Methods: Eagle Butte/Kentucky No. 9 Blend Ash. The SEM-IA method was also evaluated by comparison with CCSEM results for ash from the Eagle Butte/Kentucky No. 9 70%/30% blend. In this case, a freeze-dried dispersion was analyzed using SEM-IA, and a standard dispersion prepared from the same sample was analyzed using CCSEM (Table 2). As for the Eagle Butte ash samples discussed above, the results for the blend ash show distinct size-related compositional variations. The SEM-IA results, which include data for particles with a maximum diameter of 1.6 μm only, are dominated by sulfates, phosphates, and chlorides. No typical coal minerals were identified in the SEM-IA data set. Almost half of the particles identified using SEM-IA did not fit into any of the defined compositional categories and were thus classified as "unknown." These unclassified particles contain Si, Al, Mg, Ca, Na, S, Cl, and other elements in varied proportions and may represent coated mineral particles.

The CCSEM data for the blend ash indicate a range of minerals. As for the Eagle Butte ash, the mass of the blend ash analyzed using CCSEM is concentrated in particles with diameters from 1 to 10 μm. The CCSEM results for the blend ash indicate more sulfate-rich particles and fewer Ca-bearing particles than do the results for the Eagle Butte ash.

CONCLUSIONS

SEM-IA results clearly indicate a size-related shift in composition, from mineral-rich particles in the supermicron fractions, to sulfate-, phosphate-, and chloride-rich particles in the submicron fractions of both Eagle Butte and Eagle Butte/Kentucky No. 9 blend ashes. The distinct compositions of the two size fractions confirm that they form through different processes, probably primarily fragmentation and coalescence for the supermicron particles and vaporization and condensation for the submicron particles. The unique compositions of particles in the submicron fraction suggest that individual-particle analysis of these smallest particles is essential to achieving an overall understanding of the transformations occurring during combustion.

ACKNOWLEDGMENT

This work was supported by the U.S. Department of Energy under Cooperative Agreement No. DE-FC21-86MC10637.

REFERENCES

1. Raask, E. "Mineral Impurities in Coal Combustion," Hemisphere Publishing Corp.: New York, 1984.

2. Balfour, D.A.; Meserole, F.M.; Defries, T. "Utility Stack Opacity Troubleshooting Guidelines," final report; EPRI Research Project No. 2250-3, 1991.

3. Mie, G. "Beitrage zur Optik truber Medien speziell kolloidaler Metallosungen," *Ann. Phys.* **1908**, *25*, 377-445.

4. Bohren, C.F.; Huffman, D.R. "Absorption and Scattering of Light by Small Particles," John Wiley & Sons: New York, 1983, 530 p.

5. Zygarlicke, C.J.; McCollor, D.P. "The Effect of Coal Blending on Inorganic Transformations: A Study of an Eagle Butte/Kentucky #9 Blend," *In* Proceedings of the Ninth Annual International Pittsburgh Coal Conference; 1992, pp 775-789.

6. Katrinak, K.A.; Brekke, D.W.; Hurley, J.P. "Freeze-Dried Dispersions for Automated Scanning Electron Microscope Analysis of Individual Submicron Airborne Particulates," *In* Proceedings of the 50th Annual Meeting of the Electron Microscopy Society of America; San Francisco: San Francisco Press, Inc., 1992, pp 408-409.

7. Zygarlicke, C.J.; Steadman, E.N. "Advanced SEM Techniques to Characterize Coal Minerals," *Scanning Microscopy Intl.* **1990**, *4* (3), 579-589.

8. Hazrati, A.; Schrodt, J.T. "Microcharacterization of Micron/Submicron Fly Ash from a Pulverized-Dry-Coal-Burning Power Plant," *Surf. Interface Anal.* **1988**, *13*, 142-148.

9. Kaufherr, N.; Lichtman, D. "Comparison of Micron and Submicron Fly Ash Particles Using Scanning Electron Microscopy and X-Ray Elemental Analysis," *Environ. Sci. Technol.* **1984**, *18* (7), 544-547.

Table 1. Compositions, in Weight Percentages, for Eagle Butte Fly Ash

Particle Type	SEM-IA Run (freeze-dried)	CCSEM Run (freeze-dried)	CCSEM Run (standard)
Quartz	0	3.8	6.5
Iron Oxide	0	1.6	0.2
Periclase	1.6	0	0
Alumina	0	0.3	0
Calcite	0	0.7	0.8
Dolomite	0	3.0	5.0
Kaolinite	0	1.5	0
Ca Al-Silicate	0	5.0	6.2
Na Al-Silicate	0	4.3	2.3
Mixed Al-Silicate	0	1.6	1.1
Ca Silicate	0	6.5	2.6
Ca Aluminate	0	17.3	24.4
Sulfate-Rich	42.7	2.0	1.3
Phosphate-Rich	16.2	0	0
Chloride-Rich	11.4	0	0
Gypsum/Al-Silicate	0	5.8	2.8
Si-Rich	0	0.6	1.6
Ca-Rich	0	5.9	2.9
Ca-Si-Rich	0	2.2	2.6
Unknown	28.1	37.7	39.9
TOTALS	100.0	100.0	100.0

Table 2. Compositions, in Weight Percentages, for Eagle Butte/Kentucky No. 9 Blend Ash

Particle Type	SEM-IA (freeze-dried)	CCSEM (standard)
Quartz	0	6.5
Iron Oxide	0	0.5
Rutile	0	0.1
Alumina	0	0.1
Calcite	0	1.4
Ankerite	0	0.2
Kaolinite	0	6.3
Montmorillonite	0	1.8
K Al-Silicate	0	0.5
Fe Al-Silicate	0	3.9
Ca Al-Silicate	0	9.2
Na Al-Silicate	0	9.7
Aluminosilicate	0	0.1
Mixed Al-Silicate	0	2.4
Ca Silicate	0	1.9
Ca Aluminate	0	1.4
Sulfate-Rich	24.5	17.7
Phosphate-Rich	13.4	0
Chloride-Rich	14.7	0
Gypsum/Al-Silicate	0	3.0
Si-Rich	0	3.0
Ca-Rich	0	0.1
Ca-Si-Rich	0	0.6
Unknown	47.4	29.4
TOTALS	100.0	100.0

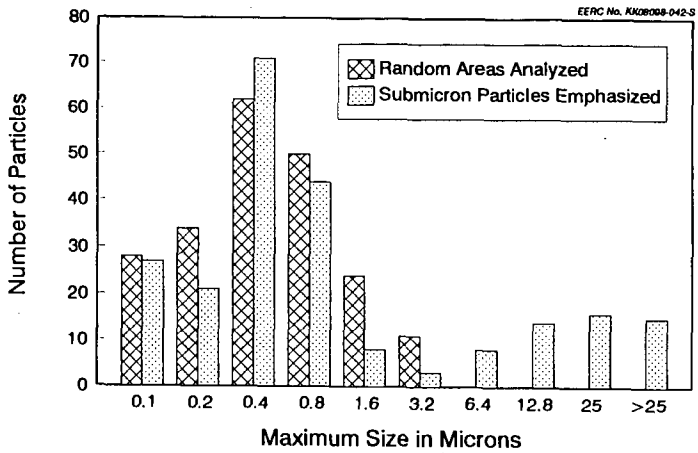

Figure 1. Size distributions for SEM-IA results for Eagle Butte ash, using a freeze-dried sample preparation.

ROLE OF CALCIUM DURING COAL COMBUSTION REVISITED

A. D. Shah, G. P. Huffman, F. E. Huggins, and Naresh Shah
CFFLS, 233 Mining and Mineral Resources Bldg.
University of Kentucky
Lexington, KY 40506-0107

Keywords: coal combustion, CCSEM, calcium behavior

ABSTRACT

Calcium is one of the most abundant elements found in low rank coals and plays a major role in ash fouling and slagging processes that result in reduced boiler efficiency during combustion of such coals. The form of occurrence of calcium in the parent coal and its interaction with other mineral matter in coal and with gaseous components during pulverized coal combustion govern the fundamental mechanisms in ash formation and ash characteristics. Several lignite and bituminous coals and their combustion products have been analyzed using Computer Controlled Scanning Electron Microscopy (CCSEM). Comparison of combustion tests carried out in different size furnaces indicate minor differences in the calcium behavior implying that the form of occurrence of calcium in the coal is more important than the scale of test facilities in determining the fate of calcium and other elements. Hence comparative combustion experiments carried out in small scale test facilities can accurately reflect the behavior of coal in utility boilers. Depending on its occurrence, calcium may react with clays to form molten Ca-aluminosilicate slag or may react with SO_2 and volatile Na to form Ca-Na sulfates.

INTRODUCTION

In low rank coals, calcium is predominantly dispersed in the macerals and is bound to carboxyl groups, whereas in bituminous coals, it is present as the discrete mineral, calcite (1). This difference in the form of occurrence plays a major role in the behavior of calcium during combustion. Past work indicates that both forms of calcium eventually react with clay minerals to form a molten glassy phase (1,2). The extent to which glass formation takes place depends on the mineral types, size and amounts in the original coals.

This paper investigates by means of the computer controlled scanning electron microscopy (CCSEM) technique, several reactions of calcium that occur during combustion, including their reactions with clays. In our research of the behavior of different elements during coal combustion, we have examined several low rank and bituminous coals and their combustion products from different test facilities of varying scale (2). The calcium behavior in ash from several bituminous and low rank coals is discussed in order to relate the form of occurrence in coal to ash formation processes. Comparative CCSEM analyses on Beulah lignite ash from several test facilities are also presented to emphasize that the size of the test facilities is of

secondary importance.

EXPERIMENTAL

Combustion experiments at three very different size test facilities were carried out at comparable temperatures. At University of Arizona (UA), a 1.8-5.0 kg/hr utility grind combustor was used to conduct the combustion tests and the samples were collected in size-segregated Anderson impactor plates. At the State Electricity Commission of Victoria (SECV), Australia, a 35 kg/hr pilot scale combustion test facility was used and the samples were collected at different locations in the facility. At PSI Technology Co. (PSI) and at MIT, combustion tests were carried out in a drop tube furnace (DTF). More specific information can be found in reference 2. Details on the CCSEM technique, sample preparations, and analyses are described elsewhere (3,4,5).

RESULTS AND DISCUSSIONS

Forms of occurrence of calcium in different coals : The four different coals compared to illustrate the effect of the form of occurrence of calcium on its interactions during combustion are an Illinois #6 bituminous coal, an Eagle Butte sub-bituminous coal, a San Miguel lignite, and a Beulah lignite. The forms of calcium in these coals were established in previous papers using CCSEM and XAFS techniques (1,2). To summarize briefly, calcite is the dominant Ca-bearing mineral in Illinois #6 coal and occurs either in close contact with other minerals or as discrete particles. Carboxyl bound calcium and a minor phase containing Ca-Sr-Al-P, possibly crandallite, are the major Ca-rich forms in Eagle Butte coal. In San Miguel lignite, calcium exists in two dominant forms: as a carboxyl bound, dispersed through the macerals and as a zeolite mineral. In Beulah lignite, calcium is primarily carboxyl bound in the macerals.

Calcium behavior during combustion in different coals : The four coals were combusted in DTFs at MIT and at PSI under similar conditions (7% O_2, approx. 1750K). The CCSEM analyses of the ash indicate varying degrees of interactions between calcium and clays as shown in the volume percentage-ternary diagrams in Figure 1. These diagrams show the volume distribution of all the ash particles identified by the CCSEM as containing > 80% Ca+Si+Al.

There is comparatively little interaction between discrete calcite and silicate minerals found in Illinois #6 coal during combustion. Some of the calcite remains as CaO particles in the ash.

In the Eagle Butte ash, numerous particles are identified by the CCSEM as Ca-rich, which are principally CaO derived from the carboxyl-bound calcium present in the coal. Calcium also interacts strongly with the clays and quartz forming Ca-aluminosilicate glass and calcium silicate phases (figure 1b). The glass phases may also form due to reaction of crandallite minerals and the clays. The crandallite mineral in the coal, which is a mixture of Ca, Sr, P and Al, probably plays a role in

the formation of an unusual Ca-rich calcium aluminate phase seen in the volume percentage-ternary diagram.

The Ca-Si-Al phase in the San Miguel lignite is richer in Si-Al. This is due to the presence of the Si-Al rich zeolite mineral in the coal. Any dispersed carboxyl-bound calcium must react with clay minerals and adds to the Ca-Si-Al glass phase. The majority of the Ca-Si-Al phase is directly formed from decomposition of the zeolite mineral.

Beulah lignite ash shows a narrow band of composition extending from the Ca-rich apex to the Si-Al border at ~Si/Al=1. The calcium that is molecularly dispersed in the macerals bound to the carboxyl group, apparently coalesces to form CaO. Some of the CaO fumes may react with clays to form Ca-Si-Al phase.

There is little formation of calcium sulfate observed in any of the DTF ash samples. The particle sizes of the Ca-Si-Al phase are comparable.

Comparison of calcium behavior in Beulah coals combusted in different size combustors : The UA impactor samples and the SECV ash samples of Beulah lignite show a similar calcium behavior to that observed in the DTF samples. Several combustion tests were carried out in the UA combustion facility. The CCSEM analysis on the size segregated ash samples collected from these tests show Ca-aluminosilicate glass as one of the dominant calcium phases. With the decrease in the particle size of the UA impactor samples, there is a reduction in the Ca-rich (CaO) particles. The Ca-aluminosilicate glass phase is more concentrated near the center of the volume percentage-ternary diagram for the finer ash fraction (figure 2).

The Ca-aluminosilicate phase in the SECV ash samples shows similar characteristics. The electrostatic precipitator (ESP) ash sample which consists of finer particles than the combustion chamber sample, show a tendency to form a phase shifted towards the center of the Ca-Si-Al plot. This shift in the composition is due to the fact that the smaller particles yield a more homogeneous glass phase. There is also a reduction in the CaO particles in the ESP as observed in the finer UA samples.

The UA and SECV samples also contain a substantial Ca-S-Na phase which is not present in the DTF samples. Figure 3 presents the volume percentage-ternary diagrams for these samples. The calcium sulfate phase is formed due to the reaction between CaO fumes and the SO_2 that is present in the gas phase during combustion. Sodium with a much lower volatilization temperature, undergoes sulfation in the vapor state to form Na_2SO_4. The two sulfates form a Ca-S-Na solid solution on rapid cooling.

The sulfate phase is dominant only in the finer ash samples. This is again attributed to the occurrence of calcium in Beulah coal and also to the fact that the sulfate phase arises from the fumes and the vapor phase. The varied compositional range in different samples is expected due to slightly different operating temperatures and due

to different sample collection methods. It appears that the combination of the size-segregated UA ash samples would cover the entire range of composition found in the plot of Ca-S-Na in the SECV samples (figure 3).

ACKNOWLEDGEMENTS

This research was supported by the U. S. Department of Energy under DOE Contract No. DE-AC22-86PC90751. We are also grateful to Dr. J. J. Helble of PSIT Inc. and Prof. T. W. Peterson of the University of Arizona for providing samples for this investigation.

References:

1. Huffman, G. P., Huggins, F. E., Shah, N., and Shah, A. D., Behavior of basic elements during coal combustion, Progress in energy and combustion science, 16 #4, 293-302 (1990).

2. Helble, J. J., Srinivasachar, S., Boni, A. A., Kang, S. G., Graham, K. A., Sarofim, A. F., Beer, J. M, Gallagher, N. B., Bool, L. E., Peterson, T. W., Wendt, J. O. L., Shah, N., Huggins, F. E., and Huffman, G. P., Mechanism of ash evolution - a fundamental study. Part I: Low-rank coals and the role of calcium. *Proceedings, Engineering Foundation Conference on Inorganic Transformation and Ash Deposition,* (Palm Coast, FL), pp. 209-228, Benson, S. A. (Ed.) (1991).

3. Huggins, F. E., Kosmack, D. A., Huffman, G. P. and Lee, R. J., Coal Mineralogies by SEM automated image analysis, Scanning Electron Microscopy 1980/I, pp. 531-540, SEM Inc., AMF O'hare, Chicago.

4. Huggins, F. E., Huffman, G. P. and Lee, R. J., Scanning Electron Microscopy-Based Automatic Image Analysis (SEM-AIA) and Mössbauer Spectroscopy: Quantitative Characterization of Coal Minerals, Coal Products: Analytical Characterization Techniques, pp. 239-258, E. L. Fuller, Jr. (Ed) ACS Symposium Series No. 205 (1982).

5. Shah, N., Huffman, G. P., Huggins, F. E. and Shah, A. D., Graphical representation of CCSEM data for coal minerals and ash particles, Proceedings, Engineering Foundation Conference on Inorganic Transformation and Ash Deposition During Combustion, (Palm Coast, FL), pp. 179-190, Benson, S. A. (Ed.) (1991).

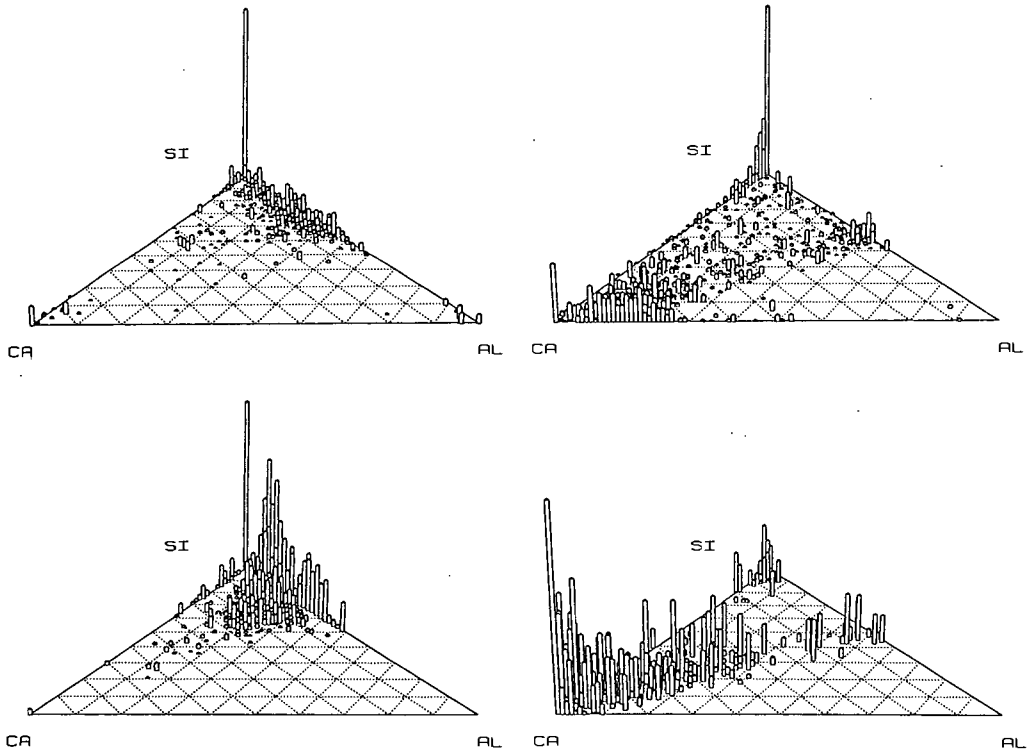

Figure 1. Ca-Si-Al volume percentage-ternary diagrams for the DTF ash samples of a)Illinois #6, b)Eagle Butte, c)San Miguel, and d)Beulah lignite. Combustion conditions 7% O_2, approx. 1750K.

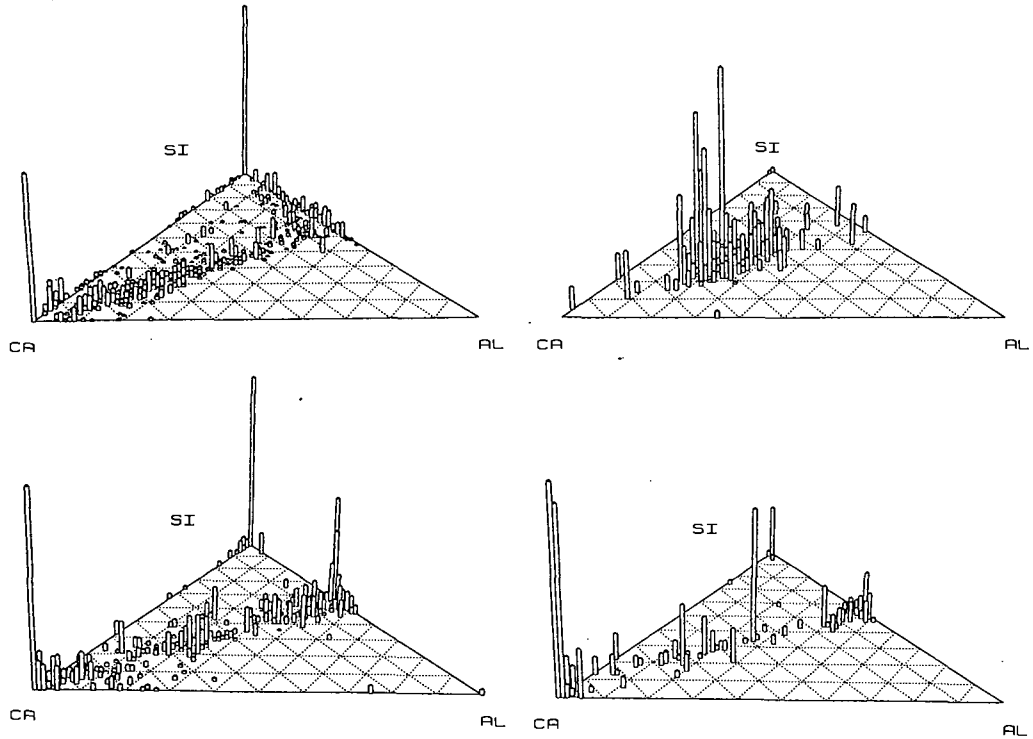

Figure 2. Ca-Si-Al volume percentage-ternary diagrams of Beulah lignite ash from a)UA combustor, impactor 1, b)UA combustor, impactor 7, c)SECV combustor, combustion chamber, and d)SECV combustor, electrostatic precipitator.

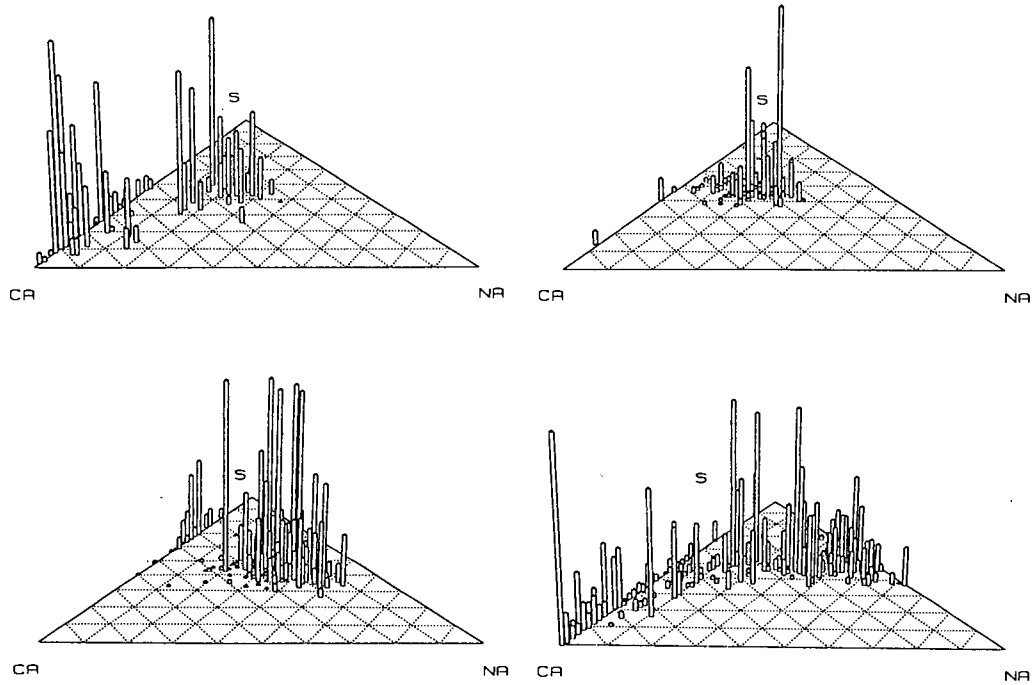

Figure 3. Ca-S-Na volume percentage-ternary diagram for Beulah lignite ash from a)UA combustor, impactors 1+cup, b)UA combustor, impactors 2+3+4, c)UA combustor, impactors 5+6+7+8+AF, and d)SECV combustor, electrostatic precipitator.

HIGH TEMPERATURE DESULFURIZATION OF SYNTHESIS GAS WITH IRON COMPOUNDS

Mitri S. Najjar and Dick Y. Jung
Texaco Inc.
P.O. Box 509
Beacon, NY 12508

Keywords: desulfurization; coal gasification; iron

INTRODUCTION

Generally, coal conversion and sulfur removal are performed in separate processing units. A combination of these two key steps within a single reaction vessel may lead to a more efficient overall process. As part of our efforts to explore this concept, the feasibility of adding iron compounds with the coal feed was examined as a means to capture sulfur in-situ during the partial oxidation of coal in a Texaco gasifier operating in the slagging mode. Iron-based compounds have been previously used as sorbents for sulfur removal but most studies have been done at lower temperatures in external desulfurization beds or with fluidized bed coal gasifiers. Relatively little work has been done to study high temperature desulfurization in conjunction with an entrained flow gasifier.

To rapidly screen iron oxide as a potential sorbent for sulfur capture, we performed theoretical studies and bench-scale testing to study the behavior of coal ash/sorbent systems under slagging gasifier conditions. Our theoretical studies included literature searches, thermodynamic equilibrium calculations, and predictions of ash/sorbent interactions utilizing published phase diagrams. Bench scale tests primarily consisted of mixing the sorbent with coal ash and exposing the mixture to synthetic Texaco coal gasification syngas mixtures at various temperatures to determine sulfur pick up and coal ash-sorbent-sulfur phase equilibria.

METHODS

Calculations Equilibrium calculations were performed for the iron sulfide/oxide interchange reaction under Texaco coal gasification conditions using either oxygen or air as the oxidant feed. Tables 1 and 2 respectively list the syngas compositions for oxygen and air gasification of Pittsburgh #8 coal at two slag (ash + additive) levels. The compositions shown under the heading "Less Reducing" are typical of normal operating conditions. The "More Reducing" conditions may be more difficult to achieve in practice because of possible slag flow problems at the lower operating temperatures. The corresponding partial pressures of oxygen and sulfur were computed using SOLGASMIX[1]. These computations were performed by keeping the moles of oxygen, carbon, hydrogen, nitrogen and sulfur constant for each case to study the effects of temperature independently.

Experiments To validate these equilibrium predictions, bench scale drop tube furnace equilibrium experiments were performed for selected coal ash-additive systems. The apparatus and experimental procedures have been previously described in our related work[2] evaluating calcium compounds as potential in-situ sulfur capture agents. Coal ash samples mixed with the sorbent are suspended in a crucible exposed to a continuous flow of $CO/CO_2/Ar/SO_2$ gas mixtures that match the computed oxygen and sulfur partial pressures

in Texaco coal gasifiers. After equilibration over at least 18 hours, the slag sample was rapidly quenched by dropping the filled crucible into a pool of water or cool syngas. The quenched slag sample was then recovered and characterized by optical microscopic examination as well as electron microprobe EDX analysis of representative grains to measure phase compositions.

RESULTS

The results of the equilibrium calculations for the iron sulfide/oxide interchange reactions with our various syngas compositions are listed in Table 3. Three major trends were observed. The ratio of iron sulfide to oxide activities increases at lower temperatures and/or more reducing conditions. Also, if one compares the ratio of iron sulfide to oxide activities at the same temperature, one observes that this ratio is higher for the oxygen gasification cases relative to the corresponding air gasification case. This suggests that oxygen gasification appears to be more favorable than air gasification for in-situ sulfur capture with iron as sorbent. Hence, the most favorable case for the iron sulfide/oxide interchange reaction involves oxygen gasification at the lowest temperature and the most reducing condition.

SOLGASMIX was also used to estimate the maximum theoretical level of sulfur capture in the iron oxysulfide phase assuming two different levels of sulfur in the coal: 2.14 wt%, and 4.0 wt%. These calculations assume no loss of iron to the silicate phase and hence represent maximum availability of iron for sulfur capture. The results shown in Figure 1 indicate that a higher percentage sulfur reduction can be achieved as the sulfur content of the coal increases.

In addition to the above equilibrium calculations, published literature data[3-7] were used to predict the partitioning of iron among the metal, oxide and oxysulfide phases. The estimated results at 2200 F are listed in Table 4. The Fe/S atomic ratio increases from 1.33 for the "More Reducing, 12% slag" case to 1.43 for the "Less Reducing, 20% slag" case. Again, these calculations indicate that iron utilization for sulfur capture is more efficient under more reducing conditions. However, the predicted amount of metallic iron is also higher at the more reducing conditions. In addition, the activity of iron oxide in the oxysulfide phase is lower for the more reducing case. Hence, it is expected that the amount of iron that can possibly associate with the silicate phase will be lower for the more reducing case since only iron oxide interacts significantly with the silicate phases.

Based on these calculations, in-situ sulfur capture due to the possible formation of a separate oxysulfide phase appears promising but experimental confirmation is needed. To check these calculations, atmospheric bench scale drop tube equilibrium tests were conducted using coal ash and iron oxide sorbents exposed to simulated syngas that match the computed oxygen and sulfur partial pressures. The results from several bench scale equilibrium tests indicate that when iron oxide was added to Pittsburgh #8 coal ash, a separate major oxysulfide phase formed in addition to the silicate phase. Typical EDX analysis for these two phases from a bench scale test are shown in Table 5. The effect of temperature on the atomic ratio of iron to sulfur in the oxysulfide phase for FeO/Pittsburgh #8 slag mixtures is shown in Figure 2. The Fe/S atomic ratio in the oxysulfide phase decreases from about 1.7 at 2500 F to about 1.15 at 1800 F.

CONCLUSIONS

The feasibility of adding iron-based compounds as potential sulfur capturing sorbents during coal gasification was examined using theoretical equilibrium calculations as well as

bench scale equilibrium droptube furnace experiments. It is predicted that iron based compounds introduced with the coal-water slurry feed can be effective agents for in-situ desulfurization under simulated syngas conditions commonly encountered in Texaco coal gasifiers operating in a slagging mode. Sulfur capture is enhanced by operating at more reducing conditions, lower temperatures and using oxygen as oxidant. Bench scale drop tube furnace tests indicate that sulfur capture is significantly increased when iron compounds were added to coal ash due to the formation of a new (major) oxysulfide phase in addition to the silicate phase. Experimental data support the predicted trend of increasing sulfur capture with decreasing temperature.

ACKNOWLEDGEMENTS

The authors gratefully acknowledge financial support for this work under the joint Texaco/Department of Energy Cooperative Program (Contract No. DE-FC21-87MC23277) on "Integration and Testing of Hot Desulfurization and Entrained Flow Gasification for Power Generation Systems" with METC's Dr. Justin Beeson as Contract Manager during this phase of the work. Within Texaco, Ron McKeon performed most of the experimental runs while Tris Laurion provided EDX analyses of slag samples.

REFERENCES

1. G. Eriksson, Acta Chem. Scand., **25** , 1971, pp 2651.
2. M. S. Najjar and D. Y. Jung, ACS Division of Fuel Chemistry Preprints **35**(4), 1990, pp 1473-1478.
3. H. Shima and A. Naldrett, Economic Geology **70**, 1975, pp 960-7.
4. D. C. Hilty and W. Crafts, Trans. AIME **194**, 1952, pp 1307-12
5. E. T. Turkdogan and G. J. Kort with Appendix by L. S. Darken and R. W. Gurry, Met. Trans. **2**, 1971, pp 1561-70.
6. M. Stofko, J. Schmiedl, and T. Rosenqvist, Scand. J. Metl. **3**, 1974, pp 113-18.
7. T. Rosenqvist and T. Hartvig, Part II, Meddeleise Nr. 12 fra Mettallurgisk Komite', Trondheim, Norway, 1958.

TABLE 1: Syngas composition for Texaco gasification of coal with oxygen oxidant

	More Reducing		Less Reducing	
Case Number	**I**	**II**	**III**	**IV**
wt% slag (ash+additive)	12	20	12	20
Syngas Composition, vol%				
CO	43.44	41.66	39.09	36.52
H_2	32.91	32.04	30.12	28.94
CO_2	9.32	10.35	12.20	13.53
H_2O	13.11	14.76	17.46	19.91
CH_4	0.03	0.03	0.02	0.02
Ar	0.06	0.06	0.06	0.06
N_2	0.45	0.44	0.42	0.41
H_2S	0.64	0.62	0.60	0.58
COS	0.04	0.04	0.03	0.03

TABLE 2: Syngas composition for Texaco gasification of coal with air oxidant

	More Reducing		Less Reducing	
Case Number	I	II	III	IV
wt% slag (ash+additive)	12	20	12	20
Syngas Composition, vol%				
CO	20.14	19.53	15.25	13.89
H_2	14.58	14.73	10.79	10.14
CO_2	6.09	6.38	8.28	8.85
H_2O	8.18	8.93	10.87	12.00
CH_4	0.05	0.05	0.02	0.02
Ar	0.61	0.60	0.65	0.66
N_2	50.06	49.50	53.80	54.11
H_2S	0.27	0.26	0.32	0.31
COS	0.02	0.02	0.02	0.02

TABLE 3: Computed equilibrium ratio of activities of iron sulfide to iron oxide (a_{FeS}/a_{FeO}) for the iron oxide/sulfide reaction $FeO + \frac{1}{2} S_2 = FeS + \frac{1}{2} S_2$

Case Number	I		II		III		IV	
Oxidant	Oxygen	Air	Oxygen	Air	Oxygen	Air	Oxygen	Air
Temp., °F								
1800	10.70	8.23	9.48	7.64	7.69	5.15	6.20	4.48
2200	5.09	3.93	4.49	3.66	3.66	2.51	2.96	2.20
2500	3.23	2.59	2.86	2.41	2.33	1.65	1.88	1.45

TABLE 4: Predicted equilibrium partitioning of iron among oxysulfide and metal phases at 2200°F based on literature data

Case Number	I	II	III	IV
$\log_{10}$\{Partial pressures\}				
S_2	-4.59	-4.60	-4.57	-4.52
O_2	-12.40	-12.30	-12.10	-11.90
Elemental, wt%				
Fe	67.70	67.70	67.70	67.70
S	29.00	28.30	27.70	27.00
O	3.30	4.00	4.60	5.30
Fe/S wt ratio	2.33	2.39	2.44	2.51
Fe/S atom ratio	1.33	1.37	1.40	1.43
lbmole/100 lb mix				
FeS	0.91	0.88	0.87	0.84
FeO	0.21	0.25	0.29	0.33
Fe	0.10	0.07	0.05	0.04
a_{FeO}	0.19	0.21	0.24	0.26

TABLE 5: Selected EDX analysis results from bench scale testing

	EDX Microanalysis				Calculated Ratios	
Particles	Fe	S	Na	Si	$(Fe/S)_{atom}$	$(Fe/Si)_{wt}$
Oxysulfide phase	67.53	25.59	2.15		1.51	
	69.68	24.28	2.06		1.64	
	69.67	24.10	2.02		1.65	
	67.86	25.95	2.02		1.49	
Silicate phase	50.28	1.48	1.48	25.64		1.96
	43.63	1.42	1.42	34.62		1.26
	49.63	1.55	1.47	30.34		1.64
	50.98	1.52	1.38	28.65		1.78
	46.57	1.31	1.40	33.40		1.39

Figure 1: Estimated maximum theoretical sulfur capture as a function of temperature, syngas composition and wt% sulfur in coal

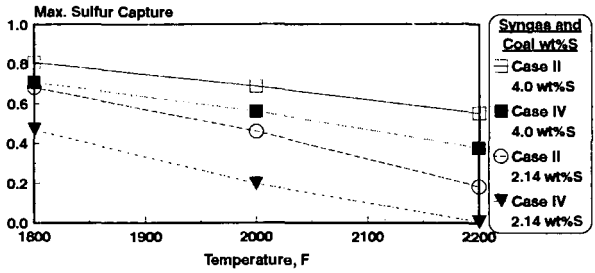

Figure 2: Effect of temperature on oxysulfide phase composition for FeO sorbent and Pittsburgh #8 coal ash slag mixtures

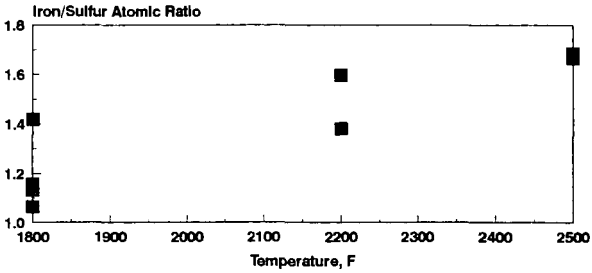

Laboratory Techniques for Evaluating Ash Agglomeration Potential in Petroleum Coke Fired Circulating Fluidized Bed Combustors

R. E. Conn
Foster Wheeler Development Corporation
12 Peach Tree Hill Road
Livingston, NJ 07039

Keywords: circulating fluidized bed (CFB), ash agglomeration, vanadium

INTRODUCTION

Petroleum coke is a waste product which is produced in large quantities in refineries throughout the U. S. Traditionally, petroleum coke has not been a boiler fuel of choice due to its relatively high sulfur content. Its burning in conventional pulverized coal-fired boilers is not desirable unless costly flue gas desulfurization is available or the coke is blended with coal to achieve acceptable sulfur emissions. However, in a CFB the coke can be effectively utilized in an environmentally sound manner by using a sorbent material for sulfur capture.

Based on experience with heavy oil fired boilers, vanadium in the fuel can result in the formation of low-melting compounds and consequent backpass deposits. In a CFB, vanadium can cause additional concerns of agglomeration in the combustor or loop seal due to molten ash compounds. When petroleum coke is burned, vanadium will ultimately oxidize to vanadium pentoxide (V_2O_5), which has a melting point well below nominal combustor temperatures (1275°F). In addition, other constituents in the coke ash and calcium-based sorbents can react with vanadium to form complexes with low melting temperatures. This paper presents simple laboratory techniques which were developed for assessing the agglomeration potential from petroleum coke firing. The results of this work helped define CFB operating conditions and identify solid additives which minimize ash agglomeration.

EXPERIMENTAL

Several laboratory tests were utilized for evaluating the potential of ash agglomeration from petroleum coke firing. These tests included measurement of ash sinter strength, electrical resistance and "hot" angles of repose/internal friction. These tests were conducted with loop seal ash (j-valve) taken from a full scale 100 MW CFB firing 100 percent delayed petroleum coke.

Analyses of the petroleum coke ash and j-valve ash are shown in Table 1. The petroleum coke contained 0.51% ash, with V_2O_5 and NiO contents of 57.0% and 10.2%, respectively. As expected the concentration of nickel and vanadium in the j-valve ash were much lower as a result of dilution from the limestone sorbent. Ash fusion temperatures are shown in Table 2. The ash fusion temperatures were considerably lower for the pure coke ash due to its relatively high vanadium content. As expected the ash fusion temperatures were lower in an oxidizing atmosphere, since vanadium compounds in a reduced state have much higher melting points than vanadium pentoxide. Particle size analysis showed that the j-valve ash

received at the laboratory was fairly fine and had a D_{50} of about 150 microns.

Ash sintering tests were performed with the j-valve ash in order to evaluate the effect of time, temperature and atmosphere on ash particle-to-particle bonding. This test has been used extensively in the past for evaluating the backpass fouling tendencies of coal ashes in p.c.-fired boilers (1, 2). This simple test involved heating a compacted ash sample in a tube furnace under an artificial atmosphere to a desired temperature for a specified period of time. After cooling the sample was measured to determine the extent of shrinkage, then crushed with a Buehler metallurgical press to measure the compressive strength. The accuracy of this machine yielded strengths which were $\pm$ 25 psi; an average strength was obtained by crushing triplicate samples. Both shrinkage and compressive strength are parameters which give an indication of the extent of agglomeration. The effect on sintering of chemical additives containing magnesium (MgO and dolomite) was also evaluated.

In conjunction with these sintering tests, electrical resistance measurements were performed on ash compacts as a function of temperature. This test is much more sensitive than conventional ash fusion tests and has been used to determine the temperature at which trace ash components melt (3,4,5). These tests were accomplished by placing ash in a crucible (0.5 in dia x 1.0 in high) between two platinum foil electrodes and measuring the electrical resistance with a Fluke multimeter. The ash sample was heated in air at a rate of 10°F/min to a temperature of 1800°F.

A simple test was also used to measure the angles of repose and internal friction of j-valve ash samples at temperatures up to about 1500°F. This test can provide important information related to the flow properties of ash in a CFB loop seal. In this test, about 3 lb of ash was placed in a 5 inch diameter quartz cylinder centered on ceramic insulation with a 1 inch diameter hole. A stainless steel strip was used to cover the hole and act as a slide gate to allow flow. This setup was placed on ceramic bricks in a box furnace which was then heated at a rate of about 5°F/min in air at temperatures between 1100°F and 1500°F. After the furnace was heated to the desired temperature, the stainless steel strip was removed which then allowed the solids in the cylinder to flow. The dimensions of the ash pile and the remaining ash in the cylinder were then measured with calipers to calculate the angles of repose and internal friction (see Figure 1).

RESULTS AND DISCUSSION

Ash sintering test results are shown in Table 3 for the j-valve ash; the effect of temperature, time and atmosphere were evaluated in these tests. Heat treatment temperature was shown to have the most significant effect on the compressive strength of ash compacts sintered in a gas mixture containing 1000 ppm SO_2/air. This gaseous environment was used to simulate that present in the bed of the CFB. No measurable compressive strength was observed until the ash was heated up to 2000°F. However, the ash compacts revealed minor shrinkage when sintered at temperatures less than 2000°F, thus indicating that agglomeration was occurring.

Table 4 lists some of the possible low melting point constituents in the j-valve ash. Even

though the j-valve ash contained only 0.8% V_2O_5, other ash and sorbent constituents can interact with vanadium to yield phases with melting points of less than 1650°F. Formation of these low melting phases was probably responsible for the shrinkage of the ash compacts below 2000°F. The development of sinter strength at 2000°F was probably due to increased liquid phase formation, coupled with a lower liquid phase viscosity. Ceramic literature has shown that the rate of agglomeration in the presence of a liquid phase is inversely proportional to the viscosity of the liquid phase (6). Ash samples heated to 2000°F appeared to have a liquid layer on the surface which actually became bonded to the alumina crucibles upon cooling. The compressive strength of the sintered ash compacts increased by a factor of three as the sintering time was increased from 2 to 18 hours (Table 3). This threefold increase in sinter strength is consistent with ceramic data which shows that the rate of ash sintering is proportional to time to the one-half power (6).

The compressive strength was found to be higher for samples sintered in the SO_2/air atmosphere compared to those sintered in air and a 1000 ppm CO/N_2 mixture. The higher compressive strength of the sample sintered in the atmosphere containing SO_2 was probably a result of bonding from the sulfation of unreacted CaO. The lower compressive strength of the ash sintered in the reducing atmosphere may be due to more vanadium being present in a reduced state. As shown in Table 4, the melting point is much higher for vanadium trioxide and tetroxide (V_2O_3 and V_2O_4) compared to V_2O_5).

Sintering tests were also performed with additives containing magnesium. These additives included a commercially available boiler additive (88.5% MgO) and a calcined dolomite containing about 40% MgO. Magnesium compounds have been used extensively to inhibit corrosion/deposition in gas turbines firing residual oil fuels containing vanadium. In gas turbines the magnesium reacts with vanadium in the fuel to form $Mg_3V_2O_8$ which has a much higher melting point than V_2O_5. Sintering test results showed that the addition of 1 wt% of the boiler additive greatly reduced the compressive strength of the ash compacts. Calcined dolomite was also shown to reduce the ash sinter strength, but to a lesser degree than the boiler additive probably due to the lower concentration of magnesium in the dolomite.

Electrical resistance measurements are shown in Figure 2 for the j-valve ash as a semi-logarithmic plot of resistance versus inverse absolute temperature. As shown in this plot, there is a change in the slope of the plot at a temperature of about 1300°F. This sharp increase in the slope of the log r versus inverse absolute temperature curve has generally been attributed to trace melting on particle surfaces, which consequently allows increased electrical conduction (3). This technique is much more sensitive than conventional ash fusion tests and can detect the melting of minor ash constituents (~1%). The onset of melting in the j-valve ash appears to coincide with the melting point of vanadium pentoxide, though it could actually be due to other ash eutectics with vanadium (Ni and Ca). Resistance measurements were also performed with ash containing 1% of the boiler additive, in order to elucidate the role of vanadium on melting. As shown in Figure 2, there was no change in the slope of the log resistance versus 1/T plot, possibly indicating that the magnesium was reacting with the vanadium to form a higher melting point material.

A several inch thick deposit taken from the upper cyclone of the 100 MW coke fired CFB

was also studied in laboratory tests. The ash chemical analysis in Table 1 shows that the deposit was enriched in vanadium (3.4% vs. 0.8%). As expected the ash fusion temperatures were much lower for the deposit compared to the j-valve ash due to this enrichment. The compressive strength of this deposit (3500 psi) was much higher than the laboratory sintered ash samples; this difference was probably due its higher vanadium content and extended exposure to elevated temperatures. A piece of this highly fused deposit was ground to less than 100 mesh (149 microns) for electrical resistance measurements. As shown in Figure 2, the deposit also had a lower onset of melting than the j-valve ash (1250 vs 1300°F).

SEM photomicrographs of the inner deposit layer and middle cross-section are shown in Figure 3. The deposit appeared to have been fairly molten and contained particles on only several microns in diameter. Semi-quantitative XRD analysis showed that the deposit was relatively consistent throughout in Ca, S and V concentrations. It was likely that vanadium interacted with calcium in the sorbent to form a low melting, low viscosity phase which promoted particle-to-particle bonding. The phase diagram for the CaO and V_2O_5 system shows equimolar concentrations of V_2O_5 and CaO form a low melting eutectic at 1432°F. Even though most of the outer surface of sorbent particles would be a sulfated shell ($CaSO_4$), some portion of the surface could be CaO due to attrition. This CaO on the surface could then react with vanadium. Phase equilibria between V_2O_5 and $CaSO_4$ could not be found in the literature and is an area for future work.

The results of ash flow tests are summarized in Table 3. For the j-valve ash without additive, the angles of repose and internal friction began to increase at about 1300°F. This temperature is approximately the same temperature at which the electrical resistance measurements show trace melting within the ash. When the temperature was increased to 1400°F, the solids would not flow and remained hung-up in the cylinder. A crusted layer was observed on the top of the ash along with weak agglomeration throughout the cylinder. With 1% of the boiler additive, the ash was observed to flow freely at temperatures up to 1500°F. Apparently, the MgO in the additive increased the melting point of eutectics and prevented agglomeration.

The extent of melting in this test appeared minor, but sufficient to inhibit the flow of solids. As a result, poor fluidization zones should be avoided in a loop seal since defluidized ash could agglomerate over a period of time, even at relatively low temperatures. This problem can be compounded in a full-scale CFB due to the weight of the column of solids causing pressure sintering.

SUMMARY AND CONCLUSIONS

Even though petroleum coke is relatively low in ash, several thousand ppm of vanadium in a coke can cause concern for ash agglomeration problems in a CFB loop seal. Laboratory tests showed that two major operating parameters can have a significant effect on controlling agglomeration. First, combustor temperature has a strong effect on the formation of low melting vanadium eutectics and the rate of agglomeration. Second, defluidization of combustor ash can lead to sintering at relatively low temperatures since dense packing promotes particle-to-particle bonding. Commercial experience with petroleum coke firng has

shown that maintaining the combustor temperature below 1700°F has helped eliminate the formation of cyclone deposits. Likewise, proper fluidization in the loop seal has been shown to reduce agglomeration of settled ash over a long period of time. Magnesium-based solid additives can also be utilized as a means of controlling vanadium related ash agglomeration. Although commercially available boiler additives can reduce agglomeration in laboratory tests, they are probably not viable candidates for commercial units due to cost considerations. On the other hand dolomite as a source of vanadium should be considered, provided it has the proper size distribution to interact with vanadium.

REFERENCES

(1) Barnhart, D. H. and Williams, P. C., "The Sintering Test - An Index to Fouling Tendency", Trans. AIME, 78, 1229-1236 (1956).

(2) Conn, R. E. and Jones, M. L., "Comparison of Low-Rank Coal Ash Sintering Characteristics with Pilot Plant Ash Fouling Tendencies", paper presented at Third Engineering Foundation Conference on Slagging and Fouling Due to Impurities in Combustion Gases, Copper Mountain, Co, July 1984.

(3) Raask, E., "Sintering Characteristics of Coal Ashes by Simultaneous Diltatometry-Electrical Resistance Measurements", J. Therm. Anal., 16, 91-102 (1979).

(4) Conn, R. E. and Austin, L. G., "Studies of the Sintering of Coal Ash Relevant to Pulverized Coal Utility Boilers", Fuel, 63, 1664-1670 (1984).

(5) Cumming, J. W. and Sanyal, A., "The Electrical Resistance of Coal Ash at Elevated Temperatures", Proceedings of the Second International Conference on Fouling and Slagging from Impurities in Combustion Gases, Henniker,N.H., July 1981.

(6) Frenkel, J. J., "Viscous Flow of Crystalline Bodies Under the Action of Surface Tension", Journal Phys., (Moscow) 9, 385 (1945).

(7) Kunii, D. and Levenspiel, O., Fluidization Engineering, Krieger Publishing Co., Malabar, FL (1969).

Table 1 Composition of Ash from 100 MW CFB

Ash Composition, wt%			
	Pet Coke Ash	J-Valve Ash	Cyclone Deposit
SiO_2	13.8	0.3	Nil
Al_2O_3	5.9	0.1	0.3
Fe_2O_3	4.5	Nil	Nil
CaO	3.6	47.1	43.1
MgO	0.6	1.4	1.7
Na_2O	0.4	0.1	0.1
NiO	10.2	0.2	0.7
V_2O_5	57.0	1.4	3.8
SO_3	1.6	48.0	48.0
Total	97.9	98.6	97.8

Table 2 Fusion Temperatures of Ash from 100 MW CFB

Ash fusion Temperatures, °F						
	Pet Coke Ash		J-Valve Ash		Cyclone Deposit	
	Reducing	Oxidizing	Reducing	Oxidizing	Reducing	Oxidizing
ID	2187	1974	2900(+)	2567	2765	2453
ST(sph)	2205	2037	2900(+)	2656	2810	2459
ST(hemi)	2213	2061	2900(+)	2798	2814	2706
FT	2220	2077	2900(+)	2800	2815	2707

Table 3 Sinter Test Results with J-Valve Ash

Temperature °F	Duration, hr	Atmosphere	Compressive Strength, Psi	Shrinkage, %
1800	2	SO_2/air	0	5
1900	2	SO_2/air	0	11
2000	2	SO_2/air	320	25
2000	18	SO_2/air	960	33
2000	2	air	200	18
2000	2	CO/N_2	125	10
2000*	2	SO_2/air	125	12
2000*	18	SO_2/air	200	15
2000**	2	SO_2/air	200	22

* 1% MgO additive added
** 1% calcined dolomite added

Table 4 Possible Ash Constituents formed During Combustion of Petroleum Coke and their Melting Points

Compound		Melting Point, °F
Calcium Sulfate	$CaSO_4$	2642
Nicke Oxide	NiO	3794
Sodium Sulfate	Na_2SO_4	1616
Vanadium trioxide	V_2O_3	3578
Vanadium tetroxide	V_2O_4	3578
Vanadium Pentoxide	V_2O_5	1274
Calcium Metavanadate	$CaO.V_2O_5$	1432
Sodium metavanadate	$Na_2O.V_2O_5$	1166
Nickel pyrovanadate	$2NiO.V_2O_5$	1650
Ferric metavanadate	$Fe_2O_3.V_2O_5$	1580

Table 5 Angles of Repose and Internal Friction for J-Valve Ash

Temperature, °F	No Additive Angle, deg. Repose	Internal Friction	1% MgO additive Angle, deg. Repose	Internal Friction
1500	- - no solids flow - -		40	90
1400	- - no solids flow - -		37	53
1300	37	90	35	51
1200	29	53	37	51
1100	30	51	36	51
Cold	30	48	35	50

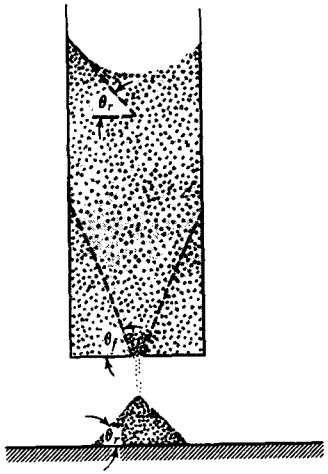

Figure 1 Angles of repose and internal friction (7)

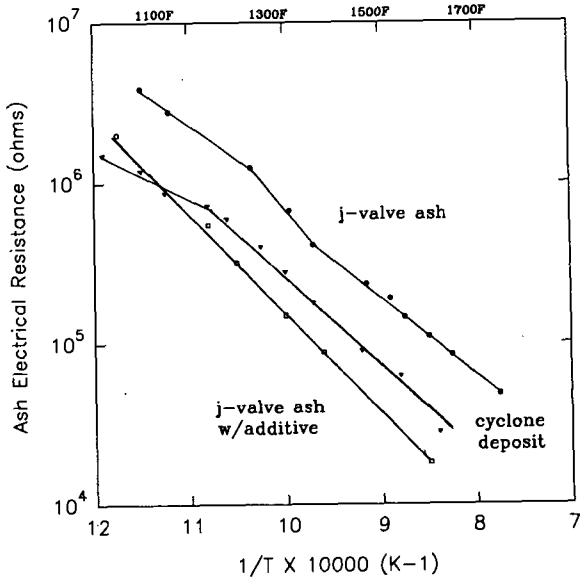

Figure 2 Ash electrical resistance measurements

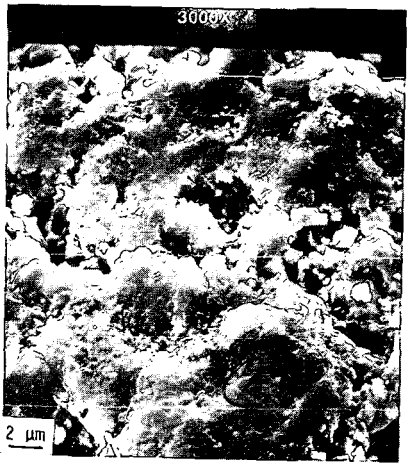

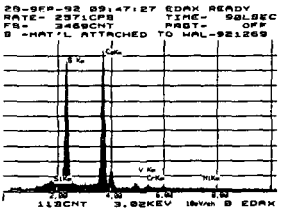

ELEM	CPS	AT % ELEM
S K	340.407	43.442
CA K	416.483	52.584
V K	15.923	2.086
CR K	7.906	1.110
NI K	3.537	0.778
TOTAL		100.000

(a) inner layer

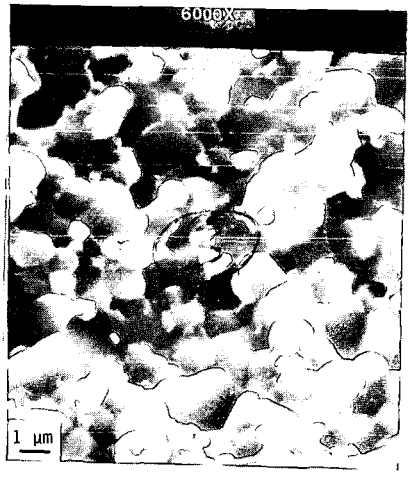

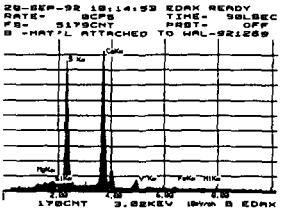

ELEM	CPS	AT % ELEM
MG K	4.317	0.646
SI K	14.869	1.213
S K	502.562	41.121
CA K	633.079	51.248
V K	40.092	3.367
FE K	10.808	1.238
NI K	8.267	1.166
TOTAL		100.000

(b) cross-section

Figure 3 SEM photomicrographs and EDX spectra for cyclone deposit: (a) inner layer and (b) cross-section

SIZE DISTRIBUTION OF ASH PARTICLES FORMED DURING COMBUSTION OF LOW-SULFUR RESIDUAL FUEL OIL IN AN ELECTRIC UTILITY BOILER

Peter M. Walsh,* Dominick J. Mormile,† and Bruce F. Piper§

*Fuel Science Program
Department of Materials Science and Engineering
Pennsylvania State University, University Park, PA 16802

†Environmental Affairs
Consolidated Edison Co. of New York, Inc.
4 Irving Place, New York, NY 10003

§Energy Technology Consultants, Inc.
51 Virginia Avenue, West Nyack, NY 10994

Keywords: ash size distribution, ash vaporization, residual oil ash

INTRODUCTION

The size distribution of particulate matter was measured by Piper and Nazimowitz (1985) in Unit 110 at the 59th Street Station of the Consolidated Edison Co. of New York, while firing low-sulfur residual fuel oil. The particles were collected using a low pressure cascade impactor placed in the flue gas at the stack breeching, where the gas temperature was 450 K (350°F). As shown in Figure 1 the particle size distribution has three distinct modes, thought to correspond to the following types of particles, from largest to smallest: 1. Unburned residues of coke formed on loss of volatile matter from spray droplets, 2. Residues of ash left on burnout of coke particles and fragments, 3. Submicron ash particles formed by vaporization of metal atoms and metal oxides from burning coke, followed by nucleation, condensation, and coagulation of the vapor. Because of the high temperature at the sampling location, sulfate was not expected to have been a significant fraction of the particulate matter. Also, because of the long residence time in the unit and high excess oxygen, soot is not expected to have been a major contributor to the submicron particles. The problem is to relate the size distribution and concentration of ash and unburned coke to fuel properties and combustion conditions.

The yield and size of coke particles formed in a boiler flame are considered by McElroy et al. (1992) and Urban, Huey, and Dryer (1992). Calculations of the emission of unburned coke and its size distribution are described by Walsh, Olen, and Washington (1992) and Walsh, Mormile, and Piper (1992). In the present preprint we focus on the two peaks associated with ash, at the left and near the center of Figure 1.

SUBMICROMETER ASH

There are two principal problems associated with a calculation of the size distribution of particles formed from the inorganic matter which vaporizes: determination of the amount of ash vaporized, and calculation of the sizes of particles resulting from coagulation of the fine particles formed on nucleation and condensation of the vapor. A previous paper (Walsh, Mormile, and Piper, 1992) describes the application of the models of Senior and Flagan (1982) and Helble, Neville, and Sarofim (1988) to ths latter process. The principal features of that model are as follows: Metal atoms, suboxides, and/or oxides vaporize from burning coke particles and diffuse from the high temperature, reducing atmosphere at the coke surface toward the more oxidizing free stream. The vapor species nucleate and condense as they

move outward, in a sequence determined by their concentrations, the oxygen concentration profile in the boundary layer, the rate coefficients for oxidation of reduced species, and their vapor pressures at the surfaces of the resulting particles (Graham, 1990; Graham et al., 1990). Once particles are formed, diffusion toward the free stream is much slower. The primary mechanism for transport of the particles then becomes the slow outward flow due to the change in gas volume accompanying the reaction $2C + O_2 \rightarrow 2CO$ at the coke particle surface (Senior and Flagan, 1982). Concentration of ash particles in the coke particle boundary layer explains the large sizes of ash particles (~0.2 μm) formed during the short time available. Coagulation occurs in the boundary layer until it dissipates on burnout of the coke, after which coagulation continues at a slower rate in the free stream. The geometric standard deviation of the size distribution formed by coagulation is given by Lee and coworkers (1983, 1984). The process is shown in Figure 2.

The other component of the submicron ash problem is the explanation of the extent of ash vaporization. The model of Quann and Sarofim (1982) and Senior and Flagan (1985) was adapted to vaporization of inorganic species from residual oil coke. The low sulfur oil contained very little vanadium, so the vaporizing species was assumed to be SiO formed by reduction of SiO_2 from aluminosilicate droplets imbedded in the coke. These droplets are derived from particles suspended in the fuel oil, which become incorporated in the coke residues. The aluminosilicate inclusions were assumed to be 1 μm in diameter. The fraction of ash vaporized was calculated for coke particles burning at constant size with decreasing density. Voidage was assumed to be uniform throughout the burning particles, and to increase linearly with time up to the porosity at which the coke disintegrates (Kerstein and Niksa, 1985). The effective pore diffusion coefficient was estimated from the porosity (Holmes, Purvis, and Street, 1990). The vapor pressure of metal suboxide adjacent to the aluminosilicate inclusions was adjusted to reproduce the observed segregation of ash between submicron particles and micron-size residues. The value giving the best agreement with the measurements was 2.8×10^{-5} atm.

The fraction of ash vaporized from small coke particles was limited by the burnout time, while the fraction vaporized from large particles was limited by diffusion. The maximum fraction vaporized occurred at a coke particle size of 40 μm, near the median size of coke formed from the oil spray droplets. For the low ash, low sulfur oils and conditions in the postflame region of the boiler, a typical fraction vaporized was 80 wt% of the ash in the oil. The calculated size distribution of submicron particles is compared with the measured distribution in Figure 1.

ASH RESIDUES

Disintegration of the coke particles on approach to complete burnout was assumed to determine the size distribution of ash remaining unvaporized. In order for this to be a good approximation, the ash particles must be uniformly distributed and smaller then the coks fragments. The breakup of coke was assumed to generate a power law distribution of fragments having a number-based probability density proportional to the -3 power of particle size (Holve, 1986; Quann and Sarofim, 1986; Baxter, 1992). This is equivalent to a uniform distribution on a mass basis. Under this assumption, fragmentation of a given size of parent coke particles produces the same mass of fragments in every geometrically-spaced size bin from the minimum fragment size up to the parent particle size. The size distribution of

ash residues left when the fragments burn out is similar to the fragment size distribution, but shifted to smaller sizes by a factor depending upon the initial ash content of the coke and fraction vaporized. The process is shown in Figure 2. All fragments, regardless of their parent particle size, were assumed to have lost the same fraction of ash by vaporization. The minimum size of fragments was adjusted to make the resulting ash residue distribution match the observed particle size distribution in the 0.8 to 7 μm size range. A minimum fragment size of 6 μm gave the best overall agreement with the size distribution measurements.

The calculated distribution of ash residues is shown near the middle of Figure 1. The step on the left side of the peak is the result of the assignment of a specific value (6 μm) to the minimum size of coke fragments. The shape could be improved by allowing for variation in the amount of ash remaining unvaporized in fragments derived from different sizes of coke particles, or by introducing a more detailed treatment of influences on the fragment size distribution (Miccio and Salatino, 1992).

CONCLUSION

The fraction of ash appearing as submicron particles in the products from combustion of a low sulfur residual oil is consistent with the model of Quann and Sarofim (1982) for vaporization of mineral particles imbedded in porous coke, accompanied by diffusion of the vapor through pores to the external surface. The sizes of the particles formed from the vapor are in agreement with the model of Senior and Flagan (1982) for coagulation of submicron particles in the boundary layer of a burning char particle.

The sizes of residues formed by the ash remaining unvaporized in the coke were assumed to depend upon the sizes of fragments formed on disintegration of the coke. The assumption of a uniform mass-based size distribution for the fragments, and a minimum fragment size of 6 μm, produced a distribution of micron-size ash particles similar to measurements in the 1 to 10 μm range, using a cascade impactor.

ACKNOWLEDGMENTS

This work was supported by the Consolidated Edison Co. of New York, Inc., Electric Power Research Institute, Empire State Electric Energy Research Corp., and Florida Power & Light Co. The Project Managers are Peter E. Coffey (ESEERCO), Dominick J. Mormile (Con Edison), Kenneth R. Olen (FPL), and William C. Rovesti (EPRI).

REFERENCES

L. L. Baxter, Char Fragmentation and Fly Ash Formation During Pulverized-Coal Combustion, Combustion and Flame 90 (1992) 174-184.

K. A. Graham, Submicron Ash Formation and Interaction with Sulfur Oxides During Pulverized Coal Combustion, Dissertation, Massachusetts Institute of Technology, Department of Chemical Engineering, Cambridge, MA, 1990.

K. A. Graham, P. M. Walsh, J. M. Beér, and A. F. Sarofim, Compositional Mapping of the Inorganic Submicron Aerosols Produced from the Combustion of Pulverized Coals and Residual Oils, Paper No. 8C4, American Association for Aerosol Research, Annual Meeting, Philadelphia, PA, June 18-22, 1990.

J. Helble, M. Neville, and A. F. Sarofim, Aggregate Formation from Vaporized Ash During Pulverized Coal Combustion, Twenty-First Symposium (International) on Combustion, The Combustion Institute, Pittsburgh, PA, 1988, pp. 411-417.

R. Holmes, M. R. I. Purvis, and P. J. Street, The Kinetics of Combustion of Oil Coke Particles, Combustion Science and Technology 70 (1990) 135-150.

D. J. Holve, In Situ Measurements of Flyash Formation from Pulverized Coal, Combustion Science and Technology 44 (1986) 269-288.

A. R. Kerstein and S. Niksa, Fragmentation During Carbon Conversion: Predictions and Measurements, Twentieth Symposium (International) on Combustion, The Combustion Institute, Pittsburgh, PA, 1985, pp. 941-949.

K. W. Lee, Change of Particle Size Distribution During Brownian Coagulation, Journal of Colloid and Interface Science 92 (1983) 315.

K. W. Lee, H. Chen, and J. A. Gieseke, Log-Normally Preserving Size Distribution for Brownian Coagulation in the Free-Molecule Regime, Aerosol Science and Technology 3 (1984) 53.

M. W. McElroy, L. J. Muzio, U. Carl, R. L. Hack, and T. A. Montgomery, The New Coking Index Method for Characterizing Fuel Oil, Proceedings: 1991 Fuel Oil Utilization Workshop, EPRI TR-100701, Electric Power Research Institute, Palo Alto, CA, 1992, pp. 3-119 to 3-135.

F. Miccio and P. Salatino, Monte-Carlo Simulation of Combustion-Induced Percolative Fragmentation of Carbons, Twenty-Fourth Symposium (International) on Combustion, The Combustion Institute, Pittsburgh, PA, 1992, pp. 1145-1151.

B. Piper and W. Nazimowitz, High Viscosity Oil Evaluation: 59th Street Station - Unit 110, KVB 21640-1, Vol. 1, Report prepared for the Consolidated Edison Co. of New York, Inc. by KVB, Inc., Engineering and Research Division, 1985.

R. J. Quann and A. F. Sarofim, Vaporization of Refractory Oxides During Pulverized Coal Combustion, Nineteenth Symposium (International) on Combustion, The Combustion Institute, Pittsburgh, PA, 1982, pp. 1429-1440.

R. J. Quann and A. F. Sarofim, A Scanning Electron Microscopy Study of the Transformations of Organically Bound Metals During Lignite Combustion, Fuel 65 (1986) 40-46.

C. L. Senior and R. C. Flagan, Ash Vaporization and Condensation During Combustion of a Suspended Coal Particle, Aerosol Science and Technology 1 (1982) 371-383.

C. L. Senior and R. C. Flagan, Synthetic Chars for the Study of Ash Vaporization, Twentieth Symposium (International) on Combustion, The Combustion Institute, Pittsburgh, PA, 1985, pp. 921-929.

D. L. Urban, S. P. C. Huey, and F. L. Dryer, Evaluation of the Coke Formation Potential of Residual Fuel Oils, Twenty-Fourth Symposium (International) on Combustion, The Combustion Institute, Pittsburgh, PA, 1992, pp. 1357-1364.

P. M. Walsh, D. J. Mormile, and B. F. Piper, Size Distribution of Particulate Matter from Combustion of Low-Sulfur Residual Fuel Oils in a Utility Boiler, Proceedings: 1991 Fuel Oil Utilization Workshop, EPRI TR-100701, Electric Power Research Institute, Palo Alto, CA, 1992, pp. 3-31 to 3-49.

P. M. Walsh, K. R. Olen, and K. T. Washington, Combustion and Emission of Coke Particles Formed from Residual Fuel Oil in Wall-Fired Electric Utility Boilers, Proceedings: 1991 Fuel Oil Utilization Workshop, EPRI TR-100701, Electric Power Research Institute, Palo Alto, CA, 1992, pp. 3-5 to 3-28.

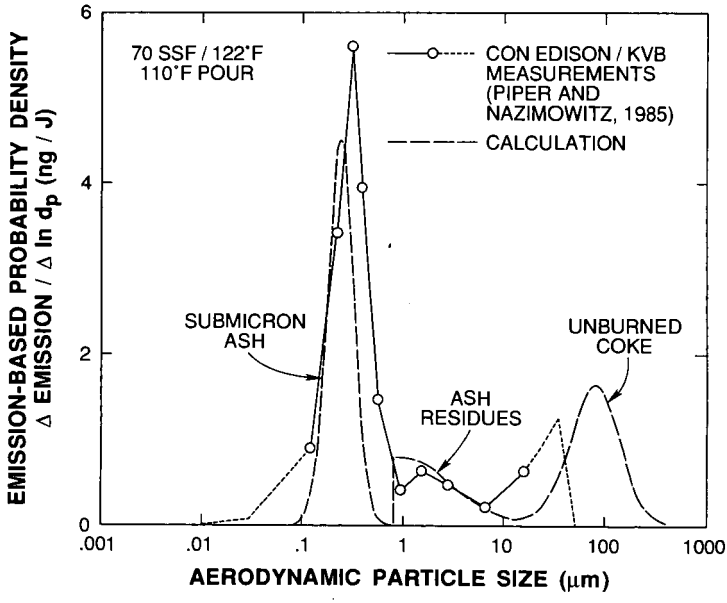

Figure 1. Emission-based size distribution of particles collected at the stack breeching in Unit 110 of the Consolidated Edison Co. of New York, using a low pressure cascade impactor (Piper and Nazimowitz, 1985). The fuel was residual oil containing (wt %): 86.64 carbon, 12.39 hydrogen, 0.23 nitrogen, 0.29 sulfur, 0.37 oxygen, 0.02 ash, 0.5 asphaltenes (IP 143), and 12 wt ppm vanadium. The API gravity was 21.3, heating value was 44.1 MJ/kg, viscosity was 70 SSF at 50°C, and the pour point was 43°C. The excess oxygen in flue gas was 2.4 mol %.

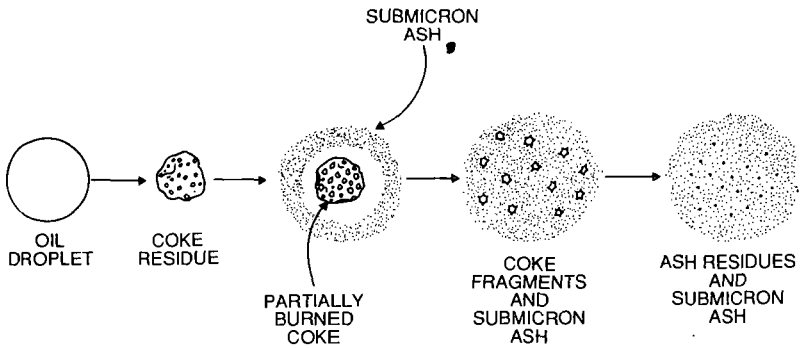

Figure 2. Formation of submicron ash and ash residues during combustion of residual oil coke particles.

UTILIZATION OF PETROLEUM COKES FOR STEAM RAISING

Richard W. Bryers
Foster Wheeler Development Corporation
12 Peach Tree Hill Road
Livingston, New Jersey 07039

Key Words: Petroleum Cokes, Vanadium, Combustion, Fouling and Corrosion

ABSTRACT

A glut of petroleum coke has made it an attractive source of cheap Btu's, either as a blended fuel or as the primary fuel. Petroleum coke, however, is low in volatiles and contains substantial concentrations of vanadium, nickel, and sulfur, which can be sources of combustion and fireside fouling or corrosion problems if not properly handled. This paper discusses the combustion characteristics of the various types of petroleum cokes used for steam raising and the fireside behavior of tha mineral matter they contain.

BACKGROUND

An excess of petroleum coke residues has stirred a great interest in firing all types of petroleum cokes in steam generators used to produce steam and electricity. The residual coke from a crude refining process—considered a residue or byproduct depending upon its utility in the marketplace—is low in volatiles and rich in vanadium, iron and nickel. The low-volatile coke produces a char with a reactivity similar to a bituminous coal. Low-volatile fuels are generally fired in an arch-type furnace to induce ignition and ensure flame stability. Attempts have been made to directly extrapolate the fireside behavior of minerals founds in oil to those retained in the coke. However, there is a significant difference in the mechanisms and kinetics of combustion for solid and liquid petroleum products, to significantly alter the behavior of the most troublesome mineral constituents found in the solid fuel. Historically, the corrosion-, slagging-, and fouling-free limit for vanadium in petroleum cokes is several orders of magnitude higher than the trouble-free limit of 50 ppm set for oil.

PETROLEUM COKE

The physical properties and the fuel analysis of a petroleum coke depend upon the crude and the manner in which it was processed. Petroleum cokes—including delayed coke, fluid coke, needle coke, shot coke, and flexicoke—are byproducts of solid residuals from the refining process.

Delayed coking is an endothermic process in which reduced crude is rapidly heated in a furnace batch-wise and then confined to a reaction zone or coke drum under proper conditions of pressure and temperature until the unvaporized portion of the furnace effluent is converted to vapor and coke. Products of the coke are gas, gasoline, gas oil, and coke.

When charging the coke with highly aromatic feedstocks at high pressures (i.e., 100 psig), a coke with a needle-like structure can be produced. The needle coke has high strength and a low coefficient of expansion. It is preferred over sponge coke for use in electrode manufacturing because of its lower electrical resistivity and lower coefficient of thermal expansion.

A third type of coke is produced unintentionally during operating upsets, probably as a result of low coke drum pressures or temperatures, or low API feed gravities. This type of coke is called "shot coke" because it occurs as clusters of shot-size pellets.

Fluid coke, as the name implies, is generated in a fluidized bed reactor operating at 1000°F. Feedstock is sprayed onto a bed of fluidized coke. The thin film of feedstock is vaporized and cracked by steam introduced into the bottom of the reactor as the coke laden with feedstock flows downward and is withdrawn from the bed. The coke is removed from the reactor where it is fed to the fluidized bed burner. Approximately 25 percent of the coke is spent to raise the temperature of the reactor coke back to 1000°F and thus provide for the endothermic losses caused by feedstock vaporization and cracking yields from fluid cokes, which are about 75 to 80 percent that of delayed coke. The resultant fluid coke withdrawn from the burner is a solid, spherical particulate smaller than 8 mesh (i.e., $< 2380\ \mu m$). The coke is very abrasive and can have a Hardgrove Index as low as 17.

The flexicoke is essentially a fluid coke from a process that includes a gasifier loop for gasifying and heating the coke leaving the fluidized bed burner in the fluid coke system. The fluidized bed burner functions as an intermediate heat exchanger between the reactor and gasifier. Adding the gasifier to the system increases the yield. Flexicoker yields can be 2 to 40 percent that of delayed coker yields. At the higher yields, one might expect higher concentrations of ash. The yields may also be limited by the initial concentration of minerals in the feedstock [1].

Table 1 compares the fuel analysis profiles of the various types of cokes described above. Table 2 compares the mineral composition.

Combustibility of Petroleum Coke

The fuel analysis indicates petroleum cokes are low in moisture and ash; consequently, they have high heating values. Unfortunately, they contain less than 10 percent volatile matter and only a few percent O_2, making them difficult to ignite. For ignition to occur, the specific rate of heat release from the oxidation process must exceed the rate of heat loss to the unheated char and the environment. Solid fuel particles provide a relatively small surface area for oxidation; and the reactivities of the char, compared with the volatiles released during the initial stage of heating, are low.

To reach a temperature where ignition or self-sustained combustion occurs, the petroleum coke particles depend upon radiant and convective heat exchange from the furnace to compensate for the lack of heat of reaction—otherwise provided by the volatiles. Minimizing excess air during ignition and the initial stages of combustion supports the rise in char temperature required to ignite the petroleum coke. Furnaces and burners designed for low-volatile fuels generally use refractory-lined walls in the immediate vicinity of the burner to support heating the fuel rather than quenching it. They also introduce air stage-wise along the path of combustion, as needed, to minimize the quenching effect of secondary air. As illustrated in Figure 1, an arch-type furnace is used to increase the flame length and provide recirculate heat to stabilize ignition, as shown in Figure 2.

Thermogravimetric analysis (TGA) performed on the various types of petroleum cokes, illustrated in Figure 3, qualitatively shows that there is very little difference in the reactivity of the raw cokes. Char generated by heating the cokes samples at 20°C/min to 1000°C is then reheated under air at a heating rate of 20°C/min. The thermograms appearing in Figure 4 indicate differences in char reactivity are even less once the volatiles have been removed. A comparison of the raw cokes with various rank coals, shown in Figure 5, indicate the reactivity of petroleum coke falls between that of a medium- to low-volatile bituminous and an anthracite. Global kinetic data may be extracted for comparison purposes by applying the Arrhenius equation:

$$\frac{dw}{dt} = K_s W^n = -A W^n e^{E/RT} P_s$$

where w = 1 for a first-order reaction.

All experiments using TGA are performed on a 10-mg sample, -44μ in size. Although flexicoke appears to be the least reactive of the petroleum cokes, recent field trials have demonstrated that blending of 15-percent flexicoke with a delayed coke resulted in a reduction in carbon loss. It would appear that a reduction in particle size associated with flexicoke can compensate for its slightly reduced reactivity. Generally, the percent carbon in fly ash from a full-scale boiler runs between 20 to 40 percent. This is equivalent to approximately 0.2 to 0.4-percent carbon loss in a coke containing 1-percent ash.

History of Fireside Problems With Heavy Oil Products

The principal ash-forming elements found in crude oil, as given by Bowden, et al., in Table 3 are the same as those found in coal, except for the addition of vanadium, nickel, and zinc [2]. Both inorganic and organic, metallic, oil-soluble forms have been observed for several of the elements. No matter which forms these elements take, the important point to note is they are retained essentially intact during the refining process and are concentrated in the residual oil. Recent X-Ray Absorption Near-Edge Structure (XANES) analysis, performed by the University of Kentucky and illustrated in Figure 6, has shown that vanadyl porphins found in heavy oil also remain intact in during the process of forming petroleum cokes. All the elements listed in Table 3 are intrinsic to the crude. Sodium concentrations may increase considerably if the crude is shipped by sea. However, the sodium level should not exceed 50 ppm in the residual oils if they are properly desalted at the refinery. Asphaltic-base crudes are generally rich in vanadium—particularly those from Venezuela, which often contain more than 500-ppm vanadium, reported as V_2O_5. Some Middle East crudes, as well as some from California, also contain appreciable amounts of vanadium. Paraffinic-base crudes usually are free of vanadium [3,4]. Refining of the crudes should raise the vanadium levels at least an order of magnitude (i.e., 1000 to 4000 ppm vanadium).

Corrosion and fouling of boilers fired with residual oil are caused by sodium, vanadium, and sulfur in the oil [5-9]. The literature attributes high-temperature corrosion primarily to vanadium, as V_2O_5 in a molten state. Molten V_2O_5 readily dissolves most refractory and metal oxides, exposing virgin metal surfaces to an oxidizing environment. The rate of oxidation is enhanced as the low viscosity and surface tension promote the counterdiffusion of O_2 to the metal surface and corrosion product from the metal surface. Condensation of sodium sulfate lowers the melting temperature of the solution by forming complex vanadates. Thus far, only the complex sodium vanadyl vanadate has been identified in actual deposits. During its formation, free O_2 is released, increasing the corrosion potential at the tube surface. Corrosion is particularly troublesome when the sodium-to-vanadium ratio exceeds 0.3, or the sodium concentration exceeds 20 ppm in the oil. The primary approach

to controlling vanadium corrosion is maintaining surface temperatures below the lowest melting vanadate.

Fouling is caused when the V_2O_5 condenses on fly ash material composed of refractory oxides at temperatures above the melting point of the V_2O_5. Counter-diffusion of the two components at the particle surface produces a sticky surface, giving the particle a high potential for sticking. Very high concentrations of refractory oxide tend to dry up the V_2O_5. If the absorption is complete prior to contact with a steam generator surface, fouling is inhibited. If not, severe fouling occurs as a sintered deposit develops on the tube surface. Fouling can also be caused by incomplete combustion, resulting in deposition of soot during operation or poor atomizing during shutdown. Vanadium is retained in oil until the last of the petroleum is vaporized, hence the high concentration of vanadium and sulfur in petroleum cokes. Unspent oil or carbon that deposits on tube surfaces is rich in vanadium and sulfur. Completion of the oxidation of this carbon at the tube surface temporarily raises the melting temperature of the ash, allowing it to melt and react with other ash on the tube surface. On cooling, it solidifies and remains tenaciously attached to the metal surface.

V_2O_3 or V_2O_4, which have melting points greater than 3500°F, will form in the presence of insufficient excess air [4]. In this case, the vanadium is innocuous and leaves the steam generator as dry ash.

Fireside Behavior of Mineral Matter in Petroleum Cokes

Petroleum cokes containing vanadium in concentrations as high as 4000 ppm have been fired in full-scale steam generators since 1957, free of corrosion or fouling except for occasional deposits attributed to either an excursion in nickel or sodium concentration or operation resulting in total char burnout. The deposits, when formed, consisted of nickel vanadates formed as a result of condensation of a nickel compound and V_2O_5. Figure 7 illustrates the crystalline nature of the deposit formed. A DTA thermogram on the petroleum coke deposit indicated that two endotherms were encountered upon heating—one coincident with the liquidous line for V_2O_5 + $Ni(VO_3)_2$, and the other coincident with the liquidous line of $Ni_2V_2O_7$—suggesting the presence of $Ni(VO_3)_2$ + $Ni_2V_2O_7$.

Combustion tests in a pilot plant of a flexicoke containing 10,000 ppm vanadium, 1700 ppm nickel, 2.35 percent sulfur, and only 5 percent volatiles in a 100-lb/h combustor for 100 hours indicated petroleum cokes with very high vanadium concentrations could be safely burned free of corrosion, slagging, or fouling. Despite the low volatility, ignition was good. The flame was stable, and the carbon loss in the ash ran about 17 percent, representing a 99.2 percent carbon utilization. The material tested came from a storage pile. Because flexicoke is extremely fine, about 60 percent -200 mesh, dirt had been used as a cover or dust suppressant to reduce wind losses. The dirt lowered the vanadium concentration to 50 percent V_2O_5 in the ash and added 31 percent SiO_2 and 11.4 percent CaO. Less than 0.3 percent of the total vanadium actually deposited on the convection bank tubes. Of the vanadium, 75 percent was captured in the fly ash as silicates and calcium vanadates. The remaining 25 percent was unaccounted and included deposited material on other surfaces or loss to the stack. The analysis of deposits appear in Table 4. The 299-g deposit formed took 100 hours to accumulate in a combustor designed to demonstrate fouling within the 5-1/4 hours of testing. Normally, fouling is considered medium if 150 to 300 g forms in 5-1/2 hours, and severe if the weight exceeds 300. Subsequent tests performed on the petroleum coke with the dirt removed indicate some V_2O_5 was formed and deposited on the convection pass probe. Fouling was light and there was no corrosion of carbon steel surfaces restricted to 850°F surface temperatures.

CONCLUSIONS

Formation of vanadium pentoxide during the combustion of vanadium-rich petroleum cokes is inhibited by excess carbon in the fly ash and/or additional mineral species such as SiO_2 or CaO in the ash. Petroleum cokes containing as much as 10,000-ppm V_2O_5 have been fired free of corrosion with minimal fouling.

REFERENCES

1. J. H. Gary, and G. E. Handwerk, Petroleum Refining Technology and Economics, Marcel Dekker, New York, 1984.

2. A. T. Bowden, P. Draper, and H. Rowling, "The Problem of Fuel Oil Ash Deposition in Open-Cycle Gas Turbines," Proceedings of the Institute Mechanical Engineers, 1953, pp. 241-300.

3. W. H. Thomas, "Inorganic Constituents of Petroleum — Part II," Science of Petroleum, Oxford University Press, London, 1938, pp. 1053-1056.

4. R. H. Filby, K. R. Shah, and F. Yaghane, "The Nature of Metals in Petroleum Fuels and Coal-Derived Synfuels," Ash Deposits and Corrosion Due to Impurities in Combustion Gases, R. W. Bryers (ed.), Hemisphere Publishing Corporation, Washington, DC, 1977.

5. W. T. Reid, External Corrosion and Deposits — Boiler and Gas Turbines, Elsevier, New York, 1971.

6. J. O. Collins and W. A. Herbit, "How Ash of Residual Fuel Oil Affects High-Temperature Boiler Operation," Power, November 1954.

7. H. W. Nelson, et al., "A Review of Available Information on Corrosion and Deposits in Coal and Oil-Fired Boilers and Gas Turbines," Battelle Memorial Institute, 1958.

8. W. D. Jarvis, "The Selection and Use of Additives in Oil-Fired Boilers," Journal of the Institute of Fuel, November 1958.

9. C. T. Evans, "Oil Ash Corrosion of Materials at Elevated Temperatures," presented at the Fifty-Third Annual Meeting of the American Society for Testing Materials, Atlantic City, New Jersey, June 26, 1950.

Table 1 Fuel Characterization of Petroleum Cokes

Description	Delayed Coke		Shot Coke		Fluid Coke		Flexicoke	
	1	2	1	2	1	2	1	2
Proximate Analysis, wt%								
Fixed Carbon	84.47	80.20	91.35	83.86	89.58	91.50	95.27	94.80
Volatile	8.62	4.48	7.21	9.59	3.07	4.94	1.77	1.28
Ash	1.08	0.72	0.87	0.76	1.05	1.32	2.50	0.99
Moisture	5.95	7.60	0.57	5.69	6.29	2.24	0.46	2.86
Ultimate Analysis, wt%								
Carbon	83.44	81.12	86.81	81.29	82.29	84.41	92.31	92.0
Hydrogen	3.35	3.60	3.46	3.17	1.74	2.12	0.68	0.30
Oxygen	0.04	0.04	0.21	0.93	1.41	0.82	0.04	0.00
Nitrogen	1.71	2.55	2.04	1.60	1.83	2.35	1.52	1.11
Sulfur	4.45	4.37	6.04	5.98	5.32	6.74	2.49	2.74
Ash	1.08	0.72	0.87	0.76	1.05	1.32	2.50	0.99
Moisture	5.95	7.60	0.57	5.69	6.29	2.24	0.46	2.96
HHV, Btu/lb	14,530	14,298	16,121	14,364	13,326	14,017	14,056	13,972

Table 2 Typical Ash Analysis of Various Types of Cokes

Elemental Composition, wt%	Delayed Coke	Shot Coke	Fluid Coke	Flexicoke Production	Flexicoke Stoker Pile
SiO_2	10.1	13.8	23.6	2.8	28.2
Al_2O_3	6.9	5.9	9.4	1.1	2.9
TiO_2	0.2	0.3	0.4	0.1	0.6
Fe_2O_3	5.3	4.5	31.6	0.8	2.7
CaO	2.2	3.6	8.9	1.8	10.3
MgO	0.3	0.6	0.4	0.2	0.8
Na_2O	1.8	0.4	0.1	2.1	0.5
K_2O	0.3	0.3	1.2	0.2	0.0
SO_3	0.8	1.6	2.0	1.0	10.0
NiO	12.0	10.2	2.9	8.0	4.5
V_2O_5	56.2	57.0	19.7	79.0	39.9
ASTM Ash Fusion, °F					
Reducing					
I.D.	2910	2617	2513	2196	2222
S.T. (Sph.)	2910	2910	2527	2199	2413
S.T. (Hem.)	2910	2910	2623	2272	2506
F.T.	2910	2910	2685	2322	2800
Oxidizing					
I.D.	2505	2299	2003	2378	2339
S.T. (Sph.)	2597	2605	2111	2454	2528
S.T. (Hem.)	2609	2680	2162	2521	2576
F.T.	2611	2680	2236	2565	2609

Table 1 Principal Ash-Forming Elements in Crude Oil

Element	Type	Solubility in Oil	Probable Chemical Form
Aluminum	Inorganic	Insoluble	Complex aluminosilicates in suspension
Calcium	Organic	Soluble	Not identified
	Inorganic	Insoluble	Calcium minerals in suspension; calcium salts in suspension or dissolved in emulsified water
Iron	Organic	Soluble	Possible iron porphyrin complexes
	Inorganic	Insoluble	Finely sized iron oxides in suspension
Magnesium	Organic	Soluble	Not identified
	Inorganic	Insoluble	Magnesium salts dissolved in emulsified water or in suspension in microcrystalline state
Nickel	Organic	Soluble	Probably porphyrin complexes
Silicon	Inorganic	Insoluble	Complex silicates and sand in suspension
Sodium	Inorganic	Insoluble	Largely sodium chloride dissolved in emulsified water or in suspension in microcrystalline state
Vanadium	Organic	Soluble	Vanadium porphyrin complexes
Zinc	Organic	Soluble	Not identified

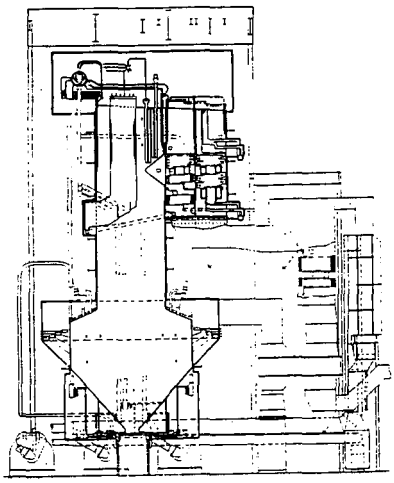

Figure 1 Utility Style Steam Generator Side Elevation

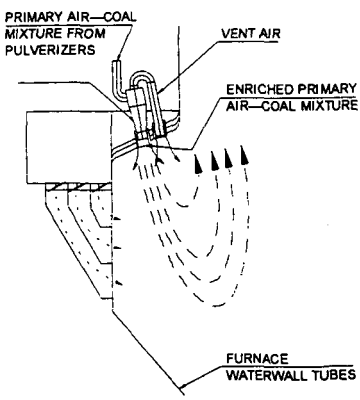

Figure 2 Downshot Cyclone Burner Arrangement

Figure 3 Combustion Profiles of Various Types of Petroleum Cokes

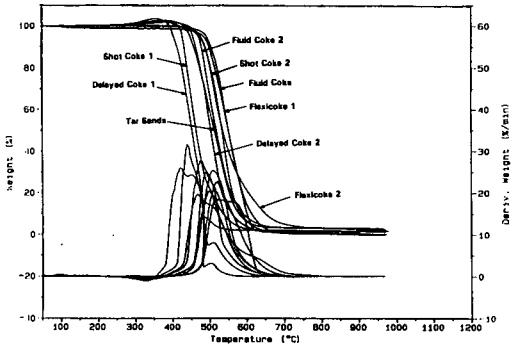

Heating Rate: 20°C/min

Figure 4 Combustion Profiles of Various Types of Petroleum Cokes Chars

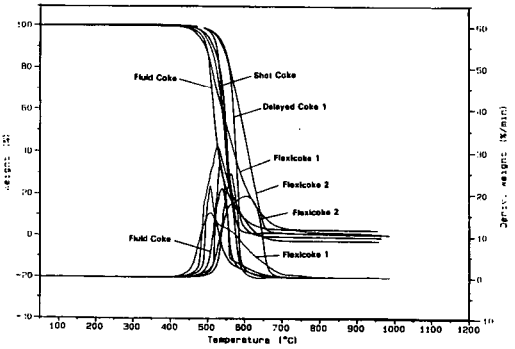

Heating Rate: 20°C/min

Figure 5 A Comparison of Combustion Profiles of Various Types North American Coals

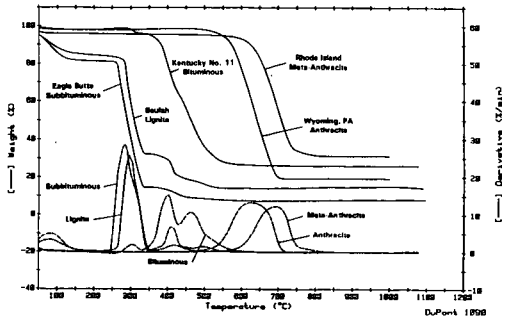

Heating Rate: 20°C/min

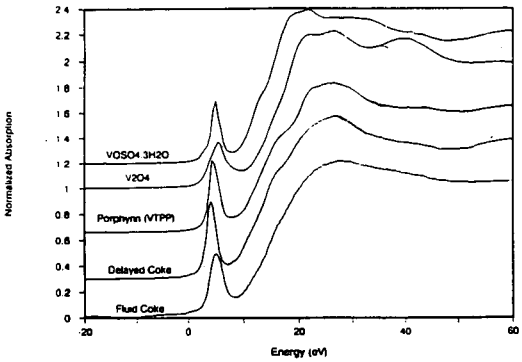

Figure 6 Comparison of the Forms of Vanadium in Delayed and Fluid Coke with the Porphyrins Found in Oil Using X-ray Absorption Near Edge Structure (XANES) Analysis by the University of Kentucky

Deposit Cross Section

Mag. 15X

Pure V_2O_5 Crystals

Mag. 300X

Figure 7 Scanning Electron Microphotography of the Deposit Formed While Firing A Petroleum Coke Whose Ash Contains 85-Percent Vanadium Expressed as V_2O_5

Table 4 Summary of Ash Fouling Probe Test Results

Gas Temperature Entering Probe Bank, °F	2034
Probe Metal Temperature, °F	753
Excess Air, %	20.4
Total Deposit Weight, g (100 hrs)	299
Chemical Composition	**wt%**
V_2O_5	45.4
NiO	4.6
SiO_2	18.1
Al_2O_3	3.0
Fe_2O_3	2.1
TiO_2	0.6
P_2O_5	1.0
CaO	7.9
MgO	0.3
Na_2O	0.6
K_2O	0.6
SO_3	15.7

IRON SULFIDE DEPOSITION DURING COAL GASIFICATION

D. Duane Brooker and Myongsook S. Oh,
Texaco R&D, P.O. Box 509, Beacon, NY 12533

Keywords: Gasification, ash, iron sulfide

INTRODUCTION

The partial combustion of coal under reducing conditions in entrained gasifiers and fluidized beds is becoming more prevalent. However, very little information on ash deposition chemistry from operating units has been published. Instead, most of the work that has been done is based on thermodynamic calculations, or laboratory experimentation associated with these calculations[1,2,3]. The thermodynamic calculations often indicated that calcium or sodium sulfide can form as a sticky slag phase at low temperatures, while iron sulfide should be the prevalent at higher temperatures.

Analyses of deposits from the Cool Water Coal Gasification Project did not identify any calcium, sodium, nor solid solution of sodium-calcium-iron sulfides in the SUFCo ash[4]. Iron sulfide was observed around most fly ash particles, but it could not be determined if the sulfide was formed from vapor deposition, reaction of H_2S from the gas with iron in the flyash, or wetted the surface of the siliceous spheres during gasification. Layers of iron sulfide that had encapsulated flyash particles within it were noted on water wall tubing and within the deposit. Based on these layers, vapor or fume deposition of iron sulfide was thought to have occurred. However, at normal gasification temperatures (1300-1500°C), iron sulfide is expected to occur as a liquid phase, not in the vapor state.

An additional opportunity to study iron sulfide deposit formation during gasification occurred during a hot gas clean-up run at Texaco's Montebello Research Laboratory. Pitts. #8, a high iron bituminous coal, was gasified during this test. Analysis of the samples yielded similar results as with the SUFCo ash from Cool Water, in that iron and sulfur were enriched on the outer surface of the siliceous flyash particles. However, unlike the Cool Water deposit analyses where distinct iron sulfide crystals were not observed, numerous euhedral iron sulfide crystals, some with siliceous spheres encapsulated in them, formed in the Pitts. #8 deposit. Again, no sodium or calcium sulfides were observed. In order to gain a better understanding of deposit formation mechanisms during gasification, detailed analyses of the Pitts. #8 deposits were done.

PROCESS DESCRIPTION

The Texaco coal gasification process involves the partial combustion of a water-coal slurry with oxygen in a refractory lined vessel[5]. Operating pressure in the unit ranges from 21-63 atm. while the operating temperatures varies from 1260-1538°C. The typical partial pressure of oxygen is approximately 10^{-11} atm. while the partial pressure of sulfur is 10^{-5} atm. at gasification temperatures. Carbon conversion is over 99%. During gasification, the inorganic material encapsulated in the coal particles forms small, molten, spherical (submicron to 100 micron) particles that either impact on the refractory lined wall to form a molten slag layer, or is entrained in the synthesis gas (syngas) exiting the vessel. Depending on the end use of the

syngas, the gas can be cooled by direct water quench, or partially cooled by passing it through a syngas cooler. Once through the cooler, the syngas is then scrubbed and cooled to remove over 99% of the sulfur. In an alternate mode of gas clean-up (hot gas clean-up), the particualte can be removed by ceramic cross-flow filters, and the sulfur captured by inorganic sorbents. Ultimately, the syngas is fed to a gas turbine for electric production, or used as process gas for chemical production.

Following a 20 hour test run for hot gas clean-up using Pitts. #8 coal, deposits were removed from a bend in a refractory lined gas transfer line exiting from a radiant syngas cooler at Texaco's pilot unit in Montebello, CA. Gasification temperatures during this run were between 1370-1482°C. The thermocouple in the transfer line indicated that the gas temperature was between 870-932°C in the area of deposition. No additives or slag modifiers were used with the coal. The initial ash chemistry of Pitts. #8 is given in Table I.

SAMPLE ANALYSIS

The deposit was removed from the transfer line without exposing them to water. Pieces of castable refractory were adhered to the outer surface of the deposit. The deposit was dark grey in color and friable in most areas. Layering occurred throughout the deposit and consisted of glass-like materials intermixed with less dense, sintered ash. Stringers of harder ash formed throughout the less sintered ash. Polished sections were made using standard reflective light polishing procedures for microscopic analyses.

A JEOL 6300 scanning electron microscope (SEM) with an attached Noran Explorer energy dispersive x-ray spectrometer (EDS) was used to analyze the samples. Chemical analyses were done using a standardless PROZA correction routine. The SEM showed that the hard, dense layers and stringers consisted of devitrofying ash particles, mostly under 2 microns in size. The rate of devitrofication appears to have been controlled mainly by the size of the particles in the layers; e.g. the smaller the particle size, the denser the layer. EDS analysis indicated that the highly sintered layer consisted of calcium alumina silicate and a sintering phase of iron-magnesium alumina silicate. Iron sulfide particles having a similar size as the remnant ash particles occurred throughout this material (Fig. 1). Also found within the highly sintered layer were layers of iron sulfide which contoured the ash layering (Fig. 2). No depletion in iron sulfide or iron were noted around the sulfide layers. However, the overall sulfur in the highly sintered material was lower than the poorly sintered samples.

In the more porous, sintered layers, the particle size increased: many flyash particles were between 5-10 microns in diameter. Deformation was common with many particles, suggesting that the particles were semi-molten at the time of impact. All of these particles were surrounded by iron sulfide droplets and crystals (Fig. 3). Most of these particles consisted of calcium-potassium alumina siliceous glass with magnesium-iron alumina silicates crystallizing within them and on the outer surface.

On the ID (gas side) of the deposit, there was a layer of poorly sinter ash which was the last material to be deposited. In this layer, the flyash particles still maintained their original roundness and showed no signs of recrystallization (Fig. 4). Iron sulfide particles were found on the outside of some of the flyash, but were smaller in size than those in the sintered material.

The deposit chemical composition (Table II) was compared to the clarifier bottom particles (flyash that passed through the transfer line and was water scrubbed from the gas) and slag particles. As seen by the bulk composition, iron is similar in concentration in the slag, clarifier bottoms, and deposit, but the sulfur concentration increases respectively. However, chemical analyses of the individual flyash particles indicate significant differences between those in the clarifier bottom and deposit. The siliceous flyash particles in the deposit are iron poor, potassium and calcium rich compared to the flyash in the clarifier bottoms. In turn the clarifier ash is slightly lower in iron content than the slag. Also, less than 5 % of the clarifier bottom particles are surrounded by iron sulfide.

SEM analysis of broken surfaces of the deposit revealed euhedral iron sulfide crystals up to 1.5 microns on the outside of the larger particles. Some of these particles were growing around the siliceous ash particles into well developed crystals (Fig. 5). X-ray diffraction (done on a Scintag Pad V instrument with a quartz standard) indicated that the sulfide occurred as both troilite and pyrrhotite.

DISCUSSION

Based on the Cool Water and MRL deposits, iron sulfide is the lowest melting phase that occurs in abundant on the outside of the ash particles, and is the most likely bonding phase for the ash. However, the mode-of-formation of the iron sulfide is not as clear based on these analyses. For instance, iron sulfide visibly occurs on the outer surface of less than 5 % of the clarifier flyash while every particle in the deposit is coated by iron and sulfur. The discreet iron sulfide particles found in the clarifier material consist of spheres or fragments mixed with siliceous glass, not euhedral crystals. Also, there exist a clear difference in the clarifier flyash chemical composition which is closer to the composition of the slag, and is much different chemical composition than the ash in the deposit. Based on the analytical evidence from the deposits, the three most likely means of formation of iron sulfide are given below:

1) **Formation of FeS during gasification.** During gasification some of the pyrite in the coal is converted to FeS droplets with small amounts of FeO (iron oxy-sulfides) and Fe within them, and fume particles. The oxy-sulfide droplets migrated to the outer surface of the siliceous ash. Only those ash particles with sufficient iron sulfide on their outer surfaces are sticky enough to be deposited. The thermodynamic calculations indicate that iron oxy-sulfide particles are sticky at deposition site temperature[6]. After deposition, the high temperatures in the transfer line caused crystallization of the glass, and recrystallization of the FeS.

A possible explanation for the difference in chemical composition between the siliceous ash in the clarifier and in the deposit is the associated mineralogy with the pyrite-rich areas in the coal seam (e.g. clay rich praticles were more prevalent). Difficulties with this theory include the formation of the discreet FeS layers within the deposit, and the large size of some of the FeS crystals compared to the loosely bonded ash. Also, not explained is the change in composition among the loosely bonded ash, clarifier bottoms, and ash in the deposit.

2) **Formation of FeS from Vapor Phase Species during Cooling.** After the particles leave the gasifier, a volatile iron species is condensed on the surface of the ash particle and reacts with H_2S upon cooling to produce an FeS coating. A thin layer of iron and sulfur was observed on the outside of the flyash from Cool Water could be indicative of vapor condensation. Other

evidence suggestive of vapor formation include the euhedral nature of the FeS crystal, encapsulation of siliceous particles within these crystals, and the occurrence of discreet FeS layers.

Vapor deposition of FeS from the gas phase does not appear very likely due to the low vapor pressure of FeS. Iron pentacarbonyl, which is a very volatile iron species, is not stable at high temperatures and is not expected to play a role in FeS formation. According to our thermodynamic equilibrium calculations shown in Table III, the only likely species of iron to be volatile is iron chloride, which may combine with the H_2S to form FeS upon cooling. However, the importance of $FeCl_2$ on FeS formation is not very conclusive as indicated by the equilibrium vapor pressure which does not change from 1200 to 900°C

3) **Formation of FeS from Iron in the Glass during Cooling**. During cooling the H_2S in the syngas interacts with iron in the ash. If this mechanism occurs, then iron depletion within the siliceous ash particle should be observed. The identification of iron magnesium alumina silicates on the surface of the ash in the deposit does indicate that iron is being expelled from the glass structure which is recrystallizing to form anorthite. However, no iron depletion was noted around the FeS layers.

Laboratory support of H_2S combining with iron to form euhedral crystals was gained from several experiments conducted by flowing a H_2S-CO-CO_2 gas mixture through a bed of clarifier bottoms ash within a quartz tube. Analysis of the clarifier bottom ash indicated the sulfur content went from 3.3 wt. % to 11.3 wt.%. Within the ash, euhedral cyrstals of iron sulfide were prevalent and of the same size as the deposit.

Quite likely, both mechanisms 1 and 3 are occurring based on the evidence from Pitts. #8 and SUFCo deposits. Hence, the following depositional pathways are believed to have occurred:

1. During gasification iron oxy-sulfide particles and fumes are produced along with siliceous particles containing iron sulfide. The iron sulfide within the siliceous particles migrate to the outer surface of the ash. In the case of Pitts. #8, the FeS_2 particles in the coal may be associated with calcium-potassium alumina silicate clay mineral.

2. The ash particles begin cooling downstream of the reaction chamber, where the gas temperature is still above the solidification point of the FeS and at the softening point of the ash. Additional fume particles collect on the ash. FeS also forms on the outside of the particles due to H_2S combining with the iron within the siliceous glass.

3. FeS fume particles collected on the cooler surface of the gasifier due to thermopheresic effect, thus forming a fouling layer. The ash particles that have the thickest FeS layer around them adhere to the wall in areas of high turbidity. Once adhered to the wall, the glass, which is low melting, begins to sinter and devitrofying forming anorthite and an iron-magnesium alumina silicate.

4. During sintering, the oxy-sulfide particles on the outside of the siliceous particles migrate to pores in the deposit. At temperatures above 1000°C, the iron sulfide already deposited, will recrystallized and combine with additional FeS generated from H_2S reacting with iron from the silicates to form large euhedral crystals of FeS.

CONCLUSIONS

Iron sulfide has been identified as the most likely bonding phase on the outside of flyash particles in both low and high iron coals during partial oxidation within Texaco's gasifers. SEM-EDS analysis has indicated no other elements (e.g. sodium or potassium) were present in the iron sulfide to form a low melting eutectic. Laboratory testing also suggest that the iron sulfide can be generated from H_2S in the gas reacting with iron from the glass in the flyash. The occurrence of discreet layers of iron sulfide within the deposit still remains problematic. Our own research will continue to concentrate on determining the interaction between iron and hydrogen sulfide in partial oxidation systems, by sintering the clarifier bottoms and ash deposits under simulated gasifier conditions.

REFERENCES

1. John, R. C., "Slag, Gas, and Deposit Thermochemistry in a Coal Gasifier", J. Electochemsitry, 133, (1), p205-211

2. Benson, S. A., et. al., "Coal Ash Behavior in Reducing Environment", NDEERC Report, 1992

3. Najjar, M. S. and Jung, D. Y., ACS, Div. of Fuel Chemistry Preprint 35(3), 615, 1990.

4. Brooker, D. D., "Chemistry of Deposit Formation in a Coal Gasifier Syngas Cooler", Fuel, 72(5), 665, 1993.

5. Cool Water Coal Gasification Program: Final Report, EPRI GS-6806, 1990.

6. Levin, E. M. et. al, Phase Diagrams for Ceramist, 1. p522, 1964.

TABLE I
Chemical Composition of Pitts. #8 Coal

	wt.%
Na2O	1.19
MgO	0.48
Al2O3	20.25
SiO2	38.60
P2O5	0.82
K2O	1.56
CaO	4.54
TiO2	1.05
Fe2O3	22.44
SO3	8.40

TABLE II
Chemical Composition In Deposit (SEM-EDS, elemental wt. %)

	Na	Mg	Al	Si	P	S	K	Ca	Fe
BULK									
Gas Side	1.4	2.4	17.7	34.1	0.4	10.9	3.1	8.3	20.1
Interior	1.5	2.0	17.2	31.0	0.7	11.0	2.4	8.7	24.6
Clarifier	2.5	2.1	18.6	31.2	x	3.2	2.8	7.9	27.9
Slag	2.1	1.8	20.6	35.8	x	2.3	2.1	6.0	29.7
Ave. 15 Particles									
Part. Gas Side	1.6	1.7	19.8	41.0	1.0	4.3	2.8	7.0	19.7
Part. Dep	1.5	1.5	19.6	48.1	0.7	1.8	5.0	13.0	7.4
Part. Clar.	1.8	2.2	22.4	40.5	0.3	1.1	3.1	7.2	21.6

Table III. Equilibrium Calculation of Cl and Fe system under TGP conditions.

Possible species and phases in system

GAS		LIQUID
CO (G)	Cl (g)	Fe O (l)
N2 (G)	Cl2 (g)	Fe (l)
H2 (G)	HCl (g)	Fe S (l)
H2 O (G)	Fe (g)	S (l)*
O2 (G)	FeS (g)	
H2 S (G)	FeO (g)	SINGLE
S2 (g)	Fe(CO)5 (g)	Fe (s)
	FeCl2 (g)	FeO (s)
		FeS (s)

Initial input of species

	mole	mole frac
CO (G)	30	0.30
N2 (G)	12.51	0.12
H2 (G)	23.63	0.24
H2 O (G)	33.09	0.33
H2 S (G)	0.75	0.0075
Cl2 (g)	0.014	0.00014
Fe (g)	0.243	0.0024242
System Totals	100.24	

*Temperature limits extended: max 1226.85 to 1300 °C using equation

EQUILIBRIUM STATE OF SYSTEM AT 40.0 ATM

Temp (°C)	1300	1200	1100	1000	900	800	700	600
GAS (Fugacity, atm)								
N_2 (G)	5.01	5.01	5.01	5.01	5.02	5.03	5.03	5.03
CO_2 (G)	12.01	12.01	12.02	12.02	12.03	12.06	12.06	12.06
H_2 (G)	9.45	9.45	9.45	9.45	9.45	9.45	9.45	9.45
H_2 O (G)	13.24	13.24	13.24	13.24	13.24	13.24	13.24	13.24
O_2 (G)	4.5e-11	3.4e-12	1.7e-13	5.5e-15	1.0e-16	8.7e-19	2.9e-21	2.6e-24
H S (G)	0.28	0.27	0.27	0.26	0.26	0.20	0.20	0.20
S_2 (g)	1.2e-04	4.8e-05	1.6e-05	4.3e-06	9.6e-07	1.1e-07	1.3e-08	1.1e-09
Cl (g)	1.2e-07	3.8e-08	1.0e-08	2.2e-09	3.8e-10	4.7e-11	3.8e-12	1.7e-13
Cl_2 (g)	1.6e-12	6.1e-13	2.0e-13	5.4e-14	1.2e-14	1.9e-15	2.2e-16	1.5e-17
Cl H (G)	1.1e-02	1.1e-02	1.1e-02	1.1e-02	1.1e-02	1.1e-02	1.1e-02	1.1e-02
Fe (g)	1.3e-07	1.7e-08	1.5e-09	9.1e-11	3.2e-12	5.1e-14	2.1e-16	2.4e-19
FeS (g)	4.0e-08	5.5e-09	5.6e-10	3.8e-11	1.5e-12	2.3e-14	1.2e-16	1.9e-19
FeO (g)	1.0e-09	8.4e-11	4.7e-12	1.6e-13	3.0e-15	2.2e-17	3.6e-20	1.4e-23
$Fe(CO)_5$ (g)	1.9e-19	4.0e-19	9.5e-19	2.6e-18	8.2e-18	2.9e-17	8.2e-17	3.1e-16
$FeCl_2$ (G)	2.4e-06	2.0e-06	1.6e-06	1.2e-06	7.8e-07	4.1e-07	1.2e-07	2.5e-08
LIQUID (gram)								
Fe O (l)	10.37	9.935	9.389	8.704	7.85	0	0	0
Fe (l)	2.371	2.189	1.974	1.723	1.438	0	0	0
Fe S (l)	4.938	5.759	6.767	7.999	9.493	0	0	0
S (l)	0.0045	0.0035	0.0026	0.0019	0.0013	0	0	0
SINGLE PHASES (gram)								
Fe O (s)	0	0	0	0	0	0	0	0
Fe (s)	0	0	0	0	0	0	0	0
Fe S (s)	0	0	0	0	0	21.36	21.36	21.36

Note: The concentrations of H_2, H_2O, and CO were fixed, and CO_2 was treated as an iert gas (N_2) in the calculation.

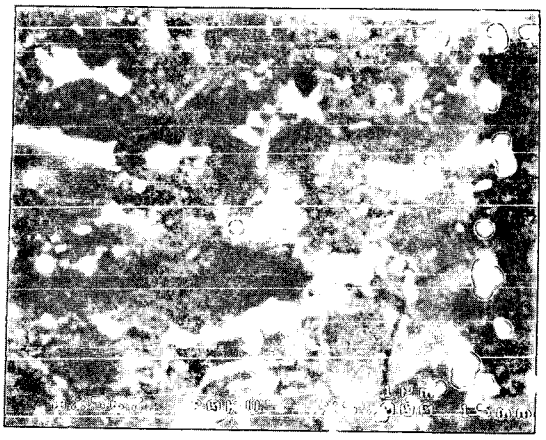

Fig. 1. SEM backscatter image of a well sintered layer in the deposit. Bright areas are iron sulfide, light grey - iron magnesium alumina silicate, and dark grey - calcium alumina silicate.

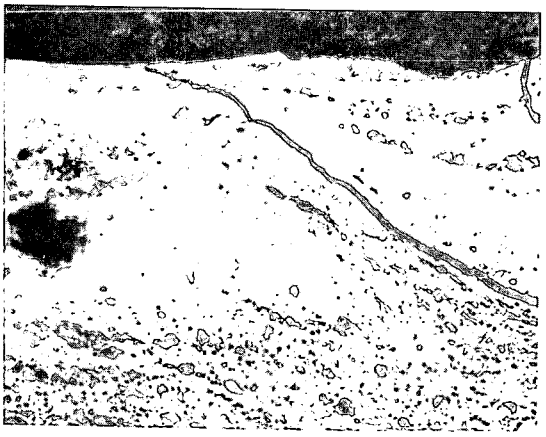

Fig. 2. Backscatter SEM image showing iron sulfide layering (bright) within a moderately sintered area of the deposit.

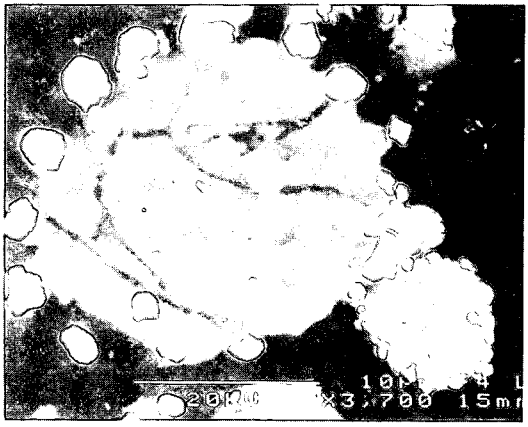

Fig. 3. Backscatter SEM image showing ash particles in a porous part of the deposit. Iron sulfide crystals (bright areas) are on the outside surface. The light grey areas are iron-magnesium alumina silicates within a calcium-potassium rich glass.

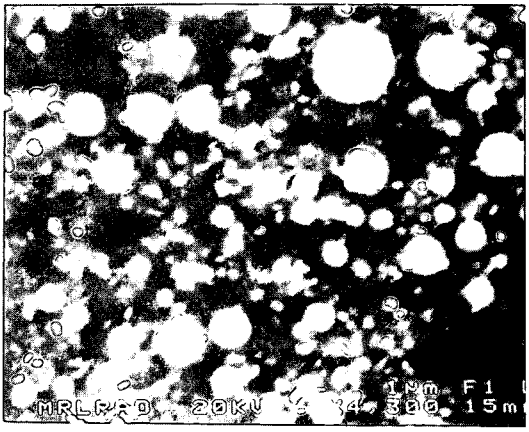

Fig. 4. SEM backscatter image of the gas exposed surface of the deposit showing an absence of sintering and devitrofication of the flyash.

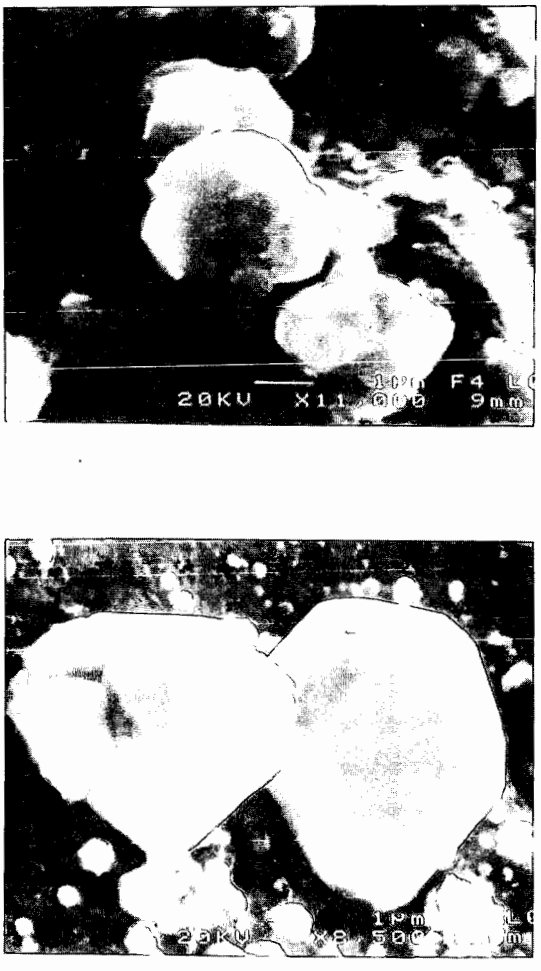

Fig. 5. SEM images of iron sulfide crystals growing on the outer surfaces of the deposit. Crystals growth can be seen occurring around siliceous particles.

COAL-ASH CORROSION OF MONOLITHIC, SILICON CARBIDE-BASED REFRACTORIES

T.M. Strobel and J.P. Hurley

Energy & Environmental Research Center
University of North Dakota
P.O. Box 9018
Grand Forks, ND 58202-9018

Keywords: ash corrosion, silicon carbide refractories, coal combustion

ABSTRACT

Several silicon carbide-based monolithic refractories were subjected to static coal ash corrosion tests to determine corrosion mechanisms and rates. Two castable refractories with 75% and 85% SiC were exposed to two types of coal ash at temperatures from 1090°C to 1430°C. Several plastic refractories were exposed to a high-calcium coal ash at 1430°C for over 100 hours. Optical microscopy and scanning electron microscopy with energy-dispersive x-ray analysis were used to determine the corrosion mechanisms and rates of these materials.

INTRODUCTION

Silicon carbide-based monolithic refractories are commonly used in coal combustion environments. Their thermal conductivities are superior to conventional materials, such as alumina or chrome-based refractories, so they are useful as replaceable, corrosion-resistant coatings on surfaces through which heat flow is required. Therefore, they are ideal for use as protective coatings on ceramic heat exchangers in advanced coal combustion systems. In these systems, a refractory may be exposed to temperatures above 1400°C, but in conventional fluidized-bed combustors, temperatures are several hundred degrees lower. Therefore, it is important to understand the interactions between SiC (silicon carbide) refractories and coal ashes in a range of temperatures.

Previous corrosion experiments focused on structural ceramics (1, 2) and SiC refractory bricks (3). The corrosion of structural SiC ceramics by acidic coal slags at 1230°C resulted in localized corrosion by iron silicides (1). The corrosion by high-calcium, basic slags at 1240°C was characterized by uniform corrosion by the dissolution of a protective SiO_2 layer by CaO in the slag to form calcium silicate compounds (2). The corrosion of SiC refractory bricks by acidic and basic slags at 1500°C involved the formation of iron silicides, and the basic slag corroded the SiC more rapidly than the acidic slag (3).

Although the literature describes corrosion of SiC ceramics and refractory bricks, little information exists on the corrosion of monolithic SiC refractories by coal ash. To determine slag corrosion mechanisms and rates, five commercially available SiC refractories were subjected to static slag corrosion tests. The materials were tested at three temperatures, 1090°, 1260°, and 1430°C, and with two types of coal ash, a high-calcium Powder River Basin (PRB) coal and a high-iron Illinois No. 6 coal. These coals were chosen because they are frequently used by utility boilers, and utility operators can use the corrosion information to determine the effects of switching from a bituminous eastern coal to a PRB coal. The slag/refractory interfaces were examined after the exposure by scanning electron and optical microscopy to determine the corrosion effects and penetration depths.

EXPERIMENTAL

These experiments focused on ash corrosion mechanisms and rates for castable and plastic monolithic SiC refractories. Monolithic refractories are nonbrick materials that are usually mixed with water at the application site and develop strength by firing to produce chemical or ceramic bonds. Two common binder materials are phosphoric acid, which produces a chemical bond at 260°C, and calcium aluminate, which develops a ceramic bond above 980°C. The castable materials contained calcium aluminate binders, and the plastics contained phosphoric acid binders. The SiC concentrations in the castables ranged from 75% to 85% and the SIC concentrations in the plastics from 50% to 70%.

The samples were prepared according to manufacturer's instructions, and each sample was formed into a cup shape to hold the coal ash during the exposure. The samples were then prefired, which caused the development of vesicular glass coatings on the plastics, but the calcium aluminate-bonded refractories were not affected, so the vesicular glass formation was attributed to the phosphoric acid binders in the plastic SiC refractories.

The two coal ashes used in the corrosion experiments included a high-calcium PRB coal ash and a high-iron Illinois No. 6 ash (Table 1). Approximately 5 grams of ash was placed into the cup of each sample, then the samples were heated to temperatures of 1090°, 1260°, and 1430°C at a rate of 100°C per hour. The castables were tested with both coal ashes at all exposure temperatures, and the plastics were tested only at 1430°C for 110 hours. All of the samples were quenched in air to determine phases present at temperature, then cross-sectioned and examined.

LOW-TEMPERATURE EXPOSURE – 1090°C FOR 55 HOURS

The two SiC castables, containing 75% and 85% SiC, were exposed to both ashes for 55 hours. After the exposure, the PRB ash was somewhat sintered, but porous and friable, and the Illinois No. 6 ash was well sintered and more dense than the PRB ash. Neither ash adhered well to the SiC refractory substrates, indicating that soot blowing would be an effective means of ash removal at this temperature. X-ray fluorescence of the ashes after the exposure showed that they did not react with the refractory, and there was no infiltration of the ash into the refractory.

INTERMEDIATE-TEMPERATURE EXPOSURE – 1260°C FOR 45 HOURS

A similar test was conducted at 1260°C using the 75% and 85% SiC castable refractories. The samples were held at temperature for 45 hours, then quenched and examined using optical microscopy and scanning electron microscopy with energy-dispersive x-ray analysis (SEM/EDX). Both ashes were liquid at 1260°C and reacted with the SiC refractories.

Powder River Basin Coal Ash. Each castable sample contained a 3- to 4-mm layer of dark gray slag, which contained a few small vesicles, approximately 0.5 mm in diameter. The vesicles indicate gas evolution during the exposure. The slag contained a continuous, red reaction layer, 0.5 mm thick, at the undulating, slag/refractory interface. Figure 1 shows several circular, metallic phases, ranging up to 0.25 mm in diameter, at the interface. The circular nature of these phases, which were high in iron, indicates that they were liquid at 1260°C and immiscible with the slag. The maximum depth of penetration of the slag into both refractories was 1 mm.

A few of the high-iron grains at the refractory/slag interface contained mainly Fe (55 wt%) and O_2 (40 wt%), but several other grains contained Fe (60 wt%), Si (up to 10 wt%), and P (up to 20 wt%), which is similar in composition to iron silicides described in other studies (1, 2), although phosphorus is not mentioned. Iron silicides are stable only under reducing conditions and indicate that portions of

the slags had low partial pressures of oxygen during the exposure. The iron oxide in the slag reacts with the SiC to form the iron silicide. This reaction also causes gas evolution of CO or CO_2, as indicated by vesicles in the slags.

The remaining slags in both sample cups were very similar in composition (Table 2). In comparison with the original ash, the slags contained less calcium oxide and more silica. The decrease in calcium is difficult to explain because no high-calcium phases were identified, but the increase in silica can be explained by the oxidation and dissolution of SiC grains from the refractory into the slag.

Illinois No. 6 Coal Ash. The slags remaining in the castable samples ranged from 5 to 6 mm thick and were black in color. Many 0.5- to 2-mm-diameter vesicles were present at the top of the slags, with a few small vesicles (0.5 mm in diameter) present at the slag/refractory boundaries, which were probably formed from CO or CO_2 evolution during the oxidation of the SiC. The samples exposed to the PRB ash contained only a few vesicles, indicating that the refractory reacted less with the PRB ash to produce fewer vesicles or that the PRB slag was less viscous at this temperature, as indicated from the higher base/acid ratio, and allowed vesicles to escape rapidly from the slag.

The maximum depth of corrosion reached 0.25 mm, but corrosion and surface pitting of the refractories were uneven and occurred in isolated areas, unlike the samples exposed to the PRB ash, which caused an even reaction layer. The slag/refractory interfaces contained discontinuous, red reaction layers and circular, iron-rich phases, 0.25 to 0.5 mm in diameter (Figure 2). The iron phases were composed of Fe (75-80 wt%) and Si (15-20 wt%), with little or no O_2 or P.

The resultant slag compositions were similar in both samples and differed only slightly from the original ash composition (Table 2). The slag contained less iron oxide than the ash, but the other major oxides were present in almost equal amounts.

HIGH-TEMPERATURE EXPOSURE – 1430°C FOR 40 HOURS

Both castable SiC refractories were subjected to a corrosion test with the PRB and Illinois No. 6 ashes at 1430°C for 40 hours. The samples were quenched and analyzed. Reaction between the slags and refractories seemed to be more extensive at this temperature than observed at 1260°C.

Powder River Basin Coal Ash. The residual slag layers in the castable SiC refractories ranged from 1 to 3 mm thick. The slags were tan in color and highly vesicular with the vesicles ranging in size from 0.5 to 2 mm in diameter. The slag was able to penetrate 2.5 mm into the refractory materials, and the penetration was aided by dissolution of the refractory binder and the incorporation of SiC grains into the slag. Some of these incorporated SiC grains were coated with red reaction rims that contained high amounts of iron and silicon. These rimmed grains indicate that the iron in the slag can be reduced to elemental iron and react with the SiC to produce iron silicides. Only a few circular, iron-rich grains were present in the slag and ranged from 0.25 to 1.0 mm in diameter. These phases contained 70 wt% Fe, 10 wt% Si, and 10 wt% P.

Chemical analyses of the slag remaining in the SiC refractory samples are given in Table 3. In general, the slag contained less calcium and magnesium and more silica than the original ash composition. The increase in silica content resulted from oxidation and dissolution of SiC grains by the slag.

Illinois No. 6 Coal Ash. The castable SiC samples contained layers of residual slag that ranged from 3 to 5 mm thick and the slag/refractory interfaces were undulating. Many vesicles, from 0.25 to 3 mm in diameter, were present along the top surfaces of the slags. Several circular metallic grains were

present at the refractory/slag interfaces and were approximately 0.25 to 0.5 mm in diameter. These grains contained 75 wt% Fe, 20 wt% Si, 5 wt% O_2, and less than 2 wt% P and were present in isolated areas along the slag/refractory interface. The maximum depth of slag penetration was 0.75 mm.

The castables seemed to react less with the Illinois No. 6 ash than the PRB ash, but some reaction occurred to alter the slag composition (Table 3). The resultant slag contained less iron and more calcium and silica than the original ash. The reduction of iron in the slag resulted from the formation of iron silicides during the dissolution of the SiC refractory.

HIGH-TEMPERATURE EXPOSURE – 1430°C FOR 80 HOURS

Powder River Basin Coal Ash. The samples contained residual slag layers 1 to 3 mm thick. The slags were transparent and highly vesicular, with vesicles ranging from 1 to 2 mm in diameter. The slag/refractory interfaces of both samples were marked with a red reaction layer, which contained small (0.25 mm in diameter), iron-rich phases (70 wt% Fe, 10 wt% Si, 8 wt% O_2, 9 wt% P). The maximum depth of slag penetration was 4 mm.

SEM analysis indicated that the ash reacted with the refractory materials to produce a resultant slag similar in composition to the slag of the 40-hour 1430°C exposure (Table 3). The slags contained more silica and less calcium and magnesium than the original ash. The decreases in calcium and magnesium may be related to the formation of calcium-magnesium phases that were not detected, but other explanations may account for their decreases. The increase in silica was caused by the oxidation and dissolution of SiC grains into the slag.

Illinois No. 6 Coal Ash. A 2- to 3-mm layer of slag was present in both of the castable samples after the 80-hour exposure. The gray slags contained a few isolated vesicles (0.25 to 0.5 mm in diameter) at the slag/refractory interfaces. Several, circular iron-rich grains were present at the interfaces and were 0.25 to 1.0 mm in diameter. These high-iron phases contained 70 to 75 wt% Fe, 20 wt% Si, 5 to 10 wt% O_2, and no P. The occurrences of the iron-rich phases were isolated, which resulted in isolated surface pitting of the refractories, and the maximum depth of slag penetration was 3 mm.

The SEM analyses indicated that the resultant slags were similar in composition to the 40-hour 1430°C exposure and contained more silica and less iron than the original slag (Table 3). The decrease in iron is related to the formation of iron silicides, and the increase in silica is a result of oxidation and dissolution of the SiC grains by the slag.

HIGH-TEMPERATURE EXPOSURE – 1430°C FOR 110 HOURS (POWDER RIVER BASIN COAL ASH)

The 75% SiC castable refractory and three plastic refractories, with SiC compositions ranging from 50% to 70%, were exposed to the PRB ash at 1430°C for 110 hours. After the exposure, the samples were quenched, cross-sectioned, and examined optically.

Castable SiC Refractory. The cup of the castable refractory contained a 5- to 6-mm layer of slag intermixed with refractory grains. Several circular metallic grains ranging from 0.5 to 2 mm in diameter were present within the slag and contained high amounts of iron and silicon, similar to the castables exposed to the PRB ash for 80 hours. This slag also was highly vesicular, indicating gas evolution during exposure. The maximum depth of penetration of the slag into the refractory was 3 mm.

Plastic SiC Refractories. The plastic samples contained residual slag layers 3 to 4 mm thick. A few small metallic grains were present within the slags, which contained vesicles ranging from 0.5 to 1 mm in diameter. The slag easily penetrated the plastic refractory materials, and penetration depths reached 10 mm in most samples.

CONCLUSIONS

Table 4 gives the penetration rates for the castable refractories exposed to the PRB and the Illinois No. 6 ashes in the static corrosion tests. The 1090°C exposure showed no ash penetration and was not included in the table, and the plastics were omitted because of their rapid penetration rates. Table 4 also shows the penetration rates relative to a 25-mm (1-in) refractory layer. These penetration rates are derived from static slag corrosion tests and do not take into consideration erosion effects of flowing slag or replenishment of fresh slag in a dynamic system. In a dynamic system, penetration rates are expected to be higher than rates determined from these static tests.

The corrosion of the SiC refractories by the PRB ash was characterized by uniform surface reaction, similar to previous studies (1, 2). Although iron silicides were found, their formation was probably not the main corrosion mechanism for this ash. The CaO in the slag may have dissolved the protective SiO_2 layer on the surface of the SiC to form calcium silicate compounds. The slag also attacked and dissolved the refractory binder and incorporated SiC grains into the slag during the 1430°C exposures.

The Illinois No. 6 ash caused localized surface pitting by the formation of iron silicide compounds. This type of corrosion was not as rapid as penetration by the PRB ash, but was still rapid at the 1430°C exposures. Only the Illinois No. 6 at 1260°C had an acceptable corrosion rate that would require replacement of a 25-mm layer of refractory every 6 months, although this rate is still excessive.

The differences in penetration rates of the two coal ashes may be related to slag viscosity, which is dependent on ash composition and temperature. The base-to-acid ratios indicate that the PRB slag probably had a lower viscosity at all exposure temperatures, which would facilitate the diffusion of corrosive elements (Ca and Fe) to the SiC surface. As temperature increases, viscosity decreases, which would also increase diffusion. The penetration rates also increased when the exposure time was increased from 40 to 80 hours at 1430°C; therefore, the penetration rates are not uniform over long exposure times, and future work should focus on comparisons of short- and long-term slag corrosion experiments.

REFERENCES

1. Ferber, M.K.; Tennery, V.J. "Behavior of Tubular Ceramic Heat Exchanger Materials in Acidic Coal Ash from Coal-Oil-Mixture Combustion," *Ceram. Bull.* **1983**, *62* (2), 236-243.

2. Ferber, M.K.; Tennery, V.J. "Behavior of Tubular Ceramic Heat Exchanger Materials in Basic Coal Ash from Coal-Oil-Mixture Combustion," *Ceram. Bull.* **1984**, *63* (7), 898-904.

3. Kennedy, C.R. "Refractory/Coal-Slag Compatibility Studies: Progress to Date," Presented at the the American Ceramic Society, Washington, D.C., May 3-8, 1981.

TABLE 1. Compositions of the Powder River Basin Ash and the Illinois No. 6 Ash Used in the Corrosion Experiments

Oxide	Powder River Basin Ash, wt%	Illinois No. 6 Ash, wt%
Na_2O	2.52	1.18
MgO	9.44	2.50
Al_2O_3	15.93	18.50
SiO_2	31.08	57.80
P_2O_5	1.77	0.00
SO_3	0.00	0.00
K_2O	0.30	0.62
CaO	33.00	3.74
TiO_2	1.03	1.03
FeO	4.40	14.62
Base/Acid*	1.03	0.29

* Base/Acid = $(FeO + CaO + MgO + Na_2O + K_2O)/(SiO_2 + Al_2O_3 + TiO_2)$.

TABLE 2. Resultant Slag Compositions for the 1260°C, 45-hour Exposure

Oxide	Powder River Basin Slag, wt%	Illinois No. 6 Slag, wt%
Na_2O	0.6	0.9
MgO	5.0	0.9
Al_2O_3	16.7	20.7
SiO_2	52.0	62.3
P_2O_5	0.0	0.1
SO_3	0.2	0.1
K_2O	0.2	1.4
CaO	23.4	5.1
TiO_2	0.5	0.8
FeO	0.5	7.6
Base/Acid	0.4	0.2

TABLE 3. Resultant Slag Compositions for the 1430°C, 40-hour Test

Oxide	Powder River Basin Slag, wt%	Illinois No. 6 Slag, wt%
Na_2O	0.9	0.6
MgO	1.7	1.0
Al_2O_3	8.9	21.6
SiO_2	69.4	66.5
P_2O_5	0.4	0.0
SO_3	0.0	0.1
K_2O	0.1	1.5
CaO	14.5	6.9
TiO_2	0.8	0.9
FeO	2.9	0.7
Base/Acid	0.3	0.1

TABLE 4. Penetration Rates for Castable Refractories Exposed to Powder River Basin and Illinois No. 6 Ashes

Ash	Temperature, °C	Exposure Time, hours	Penetration Rate, mm/100 hours	Time for Penetration of 25-mm Layer	
				hours	weeks
PRB	1260	45	2.2	1100	6.5
PRB	1430	40	6.3	400	2.4
PRB	1430	80	7.5	300	1.8
Illinois No. 6	1260	45	0.6	4500	26.8
Illinois No. 6	1430	40	1.9	1300	7.7
Illinois No. 6	1430	80	3.8	700	4.2

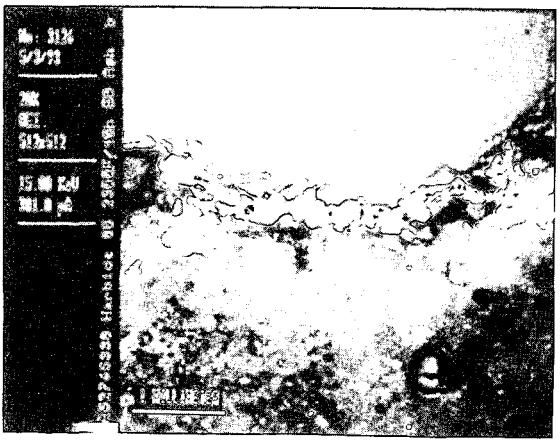

Figure 1. SEM micrograph of the reaction layer between the slag and a SiC castable refractory exposed to a PRB coal ash at 1260°C for 45 hours.

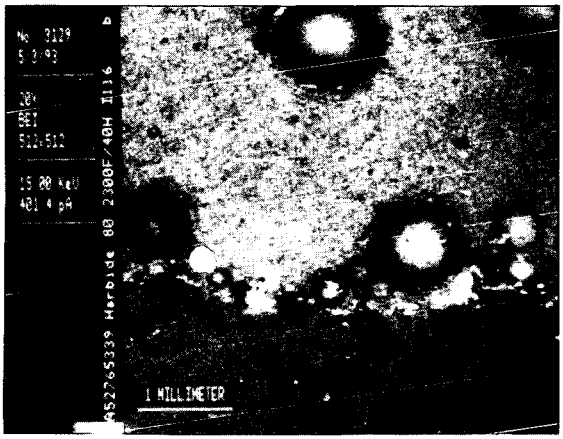

Figure 2. SEM micrograph of the slag/refractory boundary in a sample exposed to an Illinois No. 6 coal ash at 1260°C for 45 hours.

EFFECT OF CRYSTALLINE PHASE FORMATION ON COAL SLAG VISCOSITY

M. S. Oh, E. F. de Paz, D. D. Brooker, J. J. Brady, and T. R. Decker
Texaco, Inc., P.O. Box 509, Beacon, NY 12508

Keywords: Coal, Slag Viscosity, Gasification

INTRODUCTION

The Texaco Gasification Process (TGP) employs a high temperature and pressure slagging gasifier, in which the viscosity of the slag plays a key role in determining operating conditions. For all the feedstocks to TGP, the viscosity of the slag at the operating temperature has to be low enough to ensure a smooth flow out from the gasifier. The slag viscosity behavior in the gasifier has been studied through experimentation under reducing atmosphere as well as using empirical models. As in the oxidizing conditions, some coal slags exhibit the classical behavior of a glass: a continuous increase in viscosity as the temperature decreases, while others exhibit a rapid increase in viscosity when temperature is lowered below a certain temperature which is referred as the temperature of critical viscosity (T_{cv}). Below T_{cv}, it is believed that slag changes from a homogeneous fluid to a mixture containing crystallized phase(s). For glassy slags, the viscosity-temperature behavior has been modeled fairly successfully using empirical models based on slag composition, such as Watt-Fereday,[1] Si Ratio,[2] Urbain,[3] or modifications of those models.[4-6] However, when the viscosity is modified by crystalline phase formation, the empirical models fail to predict correct slag viscosity behavior. Even though the importance of the crystalline phase formation on the bulk flow properties of the slag has been long recognized, only limited information is available for prediction of T_{cv} or crystalline phase formation.[7,8]

Formation of crystalline phases and its effect on slag viscosity under gasification conditions were investigated with 4 coal slags. Slag viscosity was measured under reducing atmosphere at temperatures between 1150 - 1500 °C. Crystalline phases in slag samples were identified, and related to the observed viscosity.

EXPERIMENTAL

Set Up: The schematic of our high temperature slag viscometer is shown in Figure 1. The Haake Rotovisco RV-100 system with a coaxial cylinder sensor system was employed for viscosity measurements. The sensor system, stationary crucible and rotating bob with tapered bottom, is made of high density alumina, and placed in a high temperature furnace. The heating elements (Kanthal Super ST) of the furnace are completely isolated from the viscometer assembly by a mullite tube which runs from the top to the bottom of the furnace. This protects the brittle heating elements from breaking during loading and unloading of the sensor system. The furnace temperature control and the data acquisition of shear rate vs. shear stress were obtained through PARAGON software on an IBM PC. To simulate a reducing condition, a 60/40 mix of CO/CO_2 was passed over the sample at 300 cc/min. The gas mixture entered from the bottom of the furnace and exited through the top. The viscometer was calibrated with a NBS borosilicate glass (Standard Reference Material 717).

Procedures: A cylindrical crucible is placed in the furnace. The crucible is locked into the bottom plates of the furnace, to prevent the crucible from rotating. The bottom plates are made of low density alumina to minimize conductive heat loss from the sample. Then, the CO/CO_2 sweep gas is turned on, and the furnace is heated to 1480 °C. When the furnace reaches 1480

°C, a few grams of pelletized ashes are fed from the top. This feeding process is slow to allow the pellets to completely melt and degas before the next feeding to prevent the slag from boiling over. Once the desired level of the melt is obtained, the bob is lowered from the top, guided by an alignment pin and a stopping plate. In this way, the viscometer is assembled in the same way every time, assuring that the bob is placed in the middle of the slag sample, both horizontally and vertically. Once the viscometer assembly is complete, the temperature is decreased at the rate of 56 °C/hr. The viscosity measurements are made every 10 minutes. After the experiment, the slag is cut as shown in Figure 1 and polished for Optical Microscopy (OM) and Scanning Electron Microscopy (SEM) phase analysis. The elemental composition of the slag before and after the viscosity experiments were determined by Inductively Coupled Plasma Emission Spectroscopy (ICP-ES) and the phase analysis was also conducted by X-Ray Diffraction (XRD).

The viscosity measurements take 6 mins. The rotation rate of the bob is ramped from 0 to 65 rev/min for 3 mins and back to 0 for the next 3 mins. The shear rate is varied from 0 to 18.2 s^{-1}. The resulting shear rate-shear stress curve is that of a newtonian fluid at high temperatures, and the characteristic of a non-newtonian fluid is typical at low temperatures. For the viscosity-temperature plot, we took the viscosity at the highest shear rate.

Temperature Calibration: During viscosity measurements, there is no way to measure the sample temperature without disturbing the flow. Separate experiments were conducted to calibrate the slag temperature against the furnace temperature. Four thermocouples were placed in the slag as shown in Figure 1 to measure temperature distribution throughout the sample. Figure 2 plots the temperature differences from the mid-thermocouple (TC2) as a function of the TC2 temperature. As can be seen, the deviation was less than ± 2 °C most of the time as the temperature decreases from 1480 to 1090 °C at the rate of 56 °C/hr. One thermocouple (TC4) was placed in the center of the bob to measure the thermal inertia of the bob. The temperature difference between TC2 and TC4 was less than 5 °C most of the cooling time, proving that the alumina bob did not give much thermal inertia. In order to estimate the sample temperature during the viscosity measurements, TC2 was calibrated against the furnace control thermocouple.

Materials: The four coals include SUFCo (Hiawatha seam, high volatile C bituminous rank), Pittsburgh #8 bituminous, and two Powell Mountain coals [unwashed (PMA) and washed (PMB) coals]. SUFCo and PMA were gasification slag samples which were further ashed to remove any remaining organic carbon. Pittsburgh #8 and PMB samples were prepared from coal by ashing at 750 °C under air. We found that alumina from the crucible and the bob dissolved into the slag during viscosity measurements and raised the concentration of alumina. Table 1 presents the normalized composition after the experiments.

RESULTS

Slag Viscosity: Figure 2 plots the viscosities of the four slags as a function of temperature. The viscosity of SUFCo and PMB slags exhibit the glassy slag behavior, while the viscosity curves of Pittsburgh #8 and PMA are typical of a crystalline slag. The SUFCo slag contains high concentrations of SiO_2 and CaO, and low concentrations of Al_2O_3 and Fe_2O_3. The high concentration of SiO_2 in SUFCo causes the slag to have a higher viscosity than the others at high temperatures, and to act as a glassy slag showing a gradual increase in viscosity as the temperature decreases. Compared to SUFCo slag, Pittsburgh #8 slag has a lower SiO_2 and CaO, but higher Al_2O_3 and Fe_2O_3. Even though it exhibits the behavior of a crystalline slag, it has a low T_{cv}: the slag remains the most fluid among the four slags at temperatures above ~ 1285 °C.

As expected from a washed coal, PMB has a lower concentration of Fe_2O_3 than PMA. The SiO_2 concentration was very similar in both samples, and both contain a very low concentration of CaO and a high concentration of Al_2O_3. Since it is believed that the higher iron content usually lower the slag viscosity, the higher viscosity of PMA with T_{cv} of 1425 °C is opposite of what is expected. PMB shows a viscosity of less than 1000 poise even at 1300 °C.

Crystalline Phase Formation: The crystalline phases in the four slags, which were examined by XRD, OM, and SEM, are listed in Table 2. The SEM micrographs of the four slags are shown in Figure 4. The SUFCo slag shows glass (40-45 vol. %) and anorthite (55-60 %) as major phases. Pittsburgh #8 slag contains glass, both large crystals and dendrite of hercynites, and needle-like corundum and mullites. Both large crystals and dendritic hercynites were iron rich, with the composition of $Fe(Al,Fe)_2O_4$. The PMA slag shows extensive formation of dendritic hercynites ($FeAl_2O_4$) along with long needles of mullites. In contrast, the PMB slag has long, needle-like crystals of corundum and large crystals of hercynites. The anorthites in SUFCo and the mullite and corundum crystals in the other three were all aligned to the direction of the flow. The alignment of the crystals suggests that the crystals were formed during the viscosity measurement, not during the cooling. The crystal size of corundum in PMB was much larger than those found in Pittsburgh #8 sample. The examination of the interface between the slag and the aluminum crucible also showed that the nucleation of corundum occurred at the alumina crucible and the bob. As the nucleated particles grew into elongated crystals, they were broken off from the wall and mixed into the melt.

DISCUSSION

T_{cv}'s observed in our experiments were compared to the model proposed by Watt[7] which correlates T_{cv} as a function of slag composition. While T_{cv} for Pittsburgh #8 showed fair agreements between observed (1285 °C) and predicted (1223 °C), the predicted T_{cv} for PMA was much lower than observed (1255 vs. 1425 °C). The biggest failure of the model is for SUFCo, a glassy slag: the predicted T_{cv} was 2440 °C.

The glassy slag behavior of SUFCo and PMB suggests that the large elongated crystals do not cause a rapid increase in viscosity. In addition, precipitation of corundum and hercynite in PMB lowers the concentration of Al_2O_3 in the melt, while increasing SiO_2 concentration which may cause the melt to behave as a glassy slag. The two crystalline slags, Pittsburgh #8 and PMA, showed dendritic hercynites. From our experiment, it is not clear whether dendrites were formed during quenching after the viscosity measurements or at around T_{cv}. If the dendrites were formed during quenching, the increase in the viscosity cannot be explained. For the PMA slag, as mullites precipitate out, the remaining melt should have a lower aluminum and higher iron which would result in a lower viscosity, not higher. However, the high concentration of iron in the melt also makes it susceptible for precipitation of a Fe-phase such as hercynite. Therefore, it is more likely that the dendrites were formed at around T_{cv} and caused a rapid solidification of the slag. Watt and Fereday[7] also observed the frequent occurrence of the spinels in their slags samples from the viscometer, and stated that the formation of phases under the experimental conditions is determined more by the rate of crystallization that the phase equilibria.

The only model, we found, which incorporate the effect of crystalline phases on the slag viscosity was the model proposed by Annen et al.[9] They treated the slag as a mixture of the melt and crystalline phases, and modeled the viscosity of the mixture ($\mu_{mixture}$) as a function of liquid's viscosity (μ_{liq}) and the solid content:

$$\mu_{mixture} = \mu_{liq} (1 + 2.5\ c + 9.15\ c^2)$$

where c is the volume fraction of solids. For the viscosity of liquid phase, they employed the Watt-Fereday model. The solid's concentration and the liquid composition in the mixture were calculated using a chemical equilibrium code. The above equation is valid for solids present in the shape of spheres at low concentrations. For those slags that contained elongated crystals of mullites and corundum, the above equation may not be appropriate. The model also does not describe the effect of the particle size we observed in large crystals of spinel vs. dendritic spinels. However, the above model or variations of the above may still provide an improved first approximation to model the effect of crystalline phase formation on slag viscosity.

The success of the model by Annen et al. also depends on the accuracy of the solid's concentration predicted as a function of temperature. The thermodynamic equilibrium calculations were made for the four coal slags using normalized compositions of the five major components (SiO_2, Al_2O_3, CaO, FeO, and MgO). It was assumed that the liquid phase was an ideal mixture of various silicate species. The predicted crystalline phases at 900 °C agreed well with the observation as shown in Table 2. However, the concentration of solids predicted as a function of temperature did not improve the viscosity predictions for Pittsburgh #8 and PMA. As we and the others observed, the formation of crystalline phases in those slags may be governed by the kinetics factors. Better understanding of the rate of crystallization of various phases as well as more realistic treatments of silicate melts in thermodynamic equilibrium analysis are needed.

CONCLUSIONS

The slag viscosities of SUFCo and PMB coals exhibited the behavior of a glassy slag, of which the viscosity gradually increases as the temperature decreases. The other two, Pittsburgh #8 and PMA, showed the behavior of a crystalline slag with T_{cv} of 1285 and 1425 °C, respectively. Crystalline phase analysis of the slag samples revealed that extensive network formation of dendrite spinels in Pittsburgh #8 and PMA caused a rapid increase in the viscosity, while anorthites in SUFCo and large crystals of hercynites and elongated particles of corundum in PMA did not affect the slag viscosity as much. The prediction of crystalline phase formation under a given experimental condition and its effect on the viscosity remains to be a challenging task. Thermodynamic equilibrium analysis with a realistic treatment of silicate melt system may improve the predictions of phase formation as a function of temperature. In addition, better understanding of the rate of crystalline phase formation is needed.

REFERENCES

1. Watt, J. D., and Fereday, F., *J. Inst. Fuel, 42*, 99-103, 1969
2. Urbain, G., Cambier, F., Deletter, M., and Anseau, M. R., *Trans. J. Brit. Ceram. Soc. 80*, 139, 1981
3. Corey, R. C., US Bureau Mines Bull. No. 618, 1964
4. Schobert, H. H., Streeter, R. C., and Diehl, E. K., *Fuel, 64*, 1611, 1985
5. Kalmanovitch, D. P., Weinmann, J.R., Ness, S.R., and Benson, S. A., DE90-011398, 1990
6. Jung, B., and Schobert, H. H., *Energy Fuel, 6*, 387, 1992
7. Watt, J. D., *J. Inst. Fuel, 42*, 131-134, 1969
8. Kalmanovitch, D. P., Sanyal, A., Williamson, J., *J. Inst. Energy, 59*, 20, 1986
9. Annen, K., Gruninger, J., and Stewart, G., *Proc. Flames Res. Foundation*, 3-1, 1983

Table 1. Normalized Composition of Four Coal Slags

Oxides	SUFCo	Pitt. #8	PMA	PMB
SiO_2	60.21	46.77	43.79	43.37
Al_2O_3	15.60	24.67	26.04	29.28
Fe_2O_3	5.85	17.26	21.01	16.57
CaO	11.57	5.50	2.58	3.51
MgO	2.14	1.07	1.06	1.19
Na_2O	2.67	1.00	0.45	0.51
TiO_2	0.88	1.02	1.40	1.52
K_2O	0.43	1.84	2.22	2.08
P_2O_5	0.26	0.32	0.70	0.98
BaO	0.08	0.11	0.15	0.20
SrO	0.12	0.18	0.26	0.46
PbO	0.00	0.05	0.08	0.08
Cr_2O_3	0.19	0.22	0.26	0.30

Table 2. Crystalline Phases in Coal Slags

Coal Slag	Observed	Crystalline Phases at 900 °C by Equilibrium Calculation
SUFCo	Anorthite	Anorthite Diopside
Pittsburgh #8	Mullite Fe-rich Hercynite Corundum	Mullite Hercynite & Spinel Anorthite
PMA	Mullite Hercynite	Mullite Hercynite & Spinel
PMB	Corundum Hercynite	Mullite Spinel

Figure 1. Schematic of Slag Viscometer

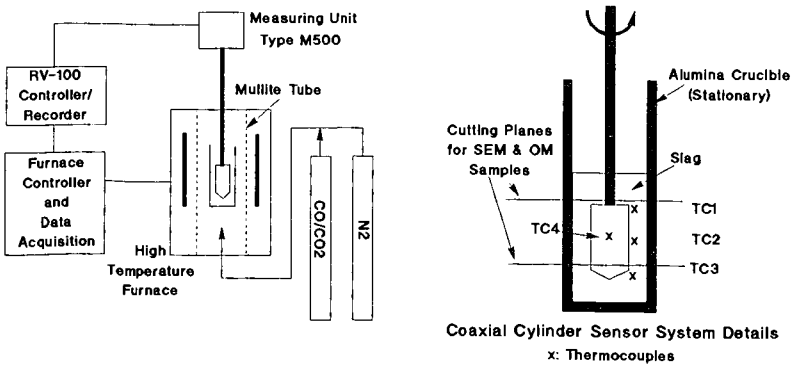

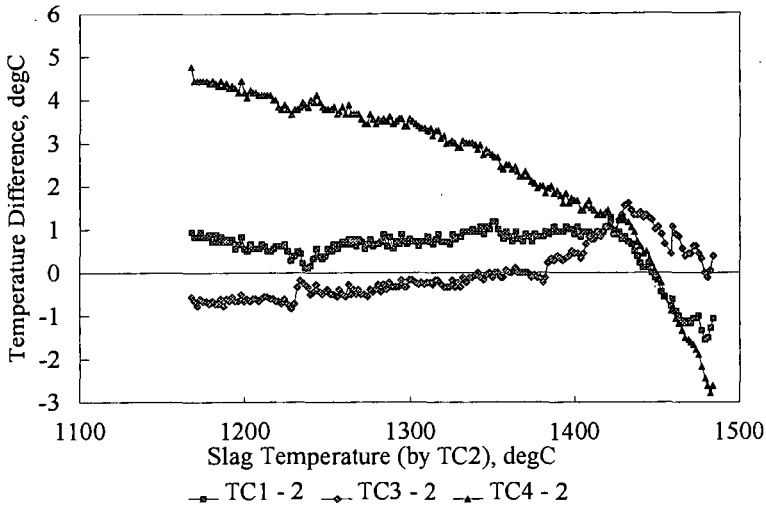

Figure 2. Temperature differences in slag sample from the mid-point.

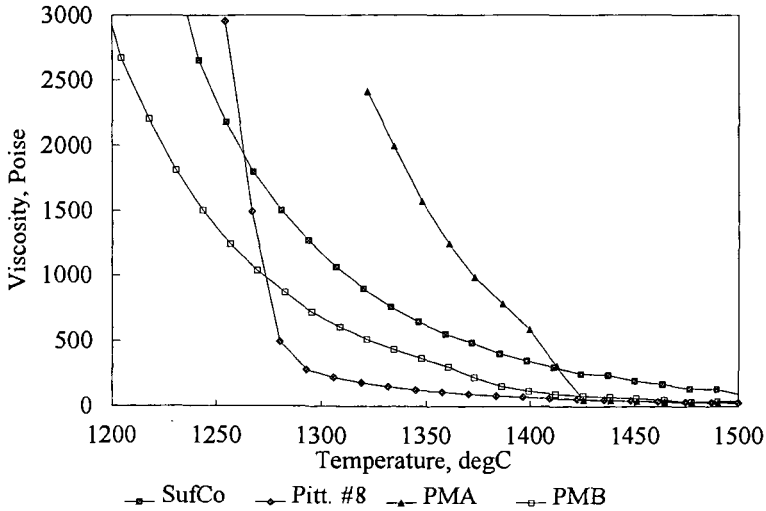

Figure 3. Slag Viscosity as a Function of Temperature
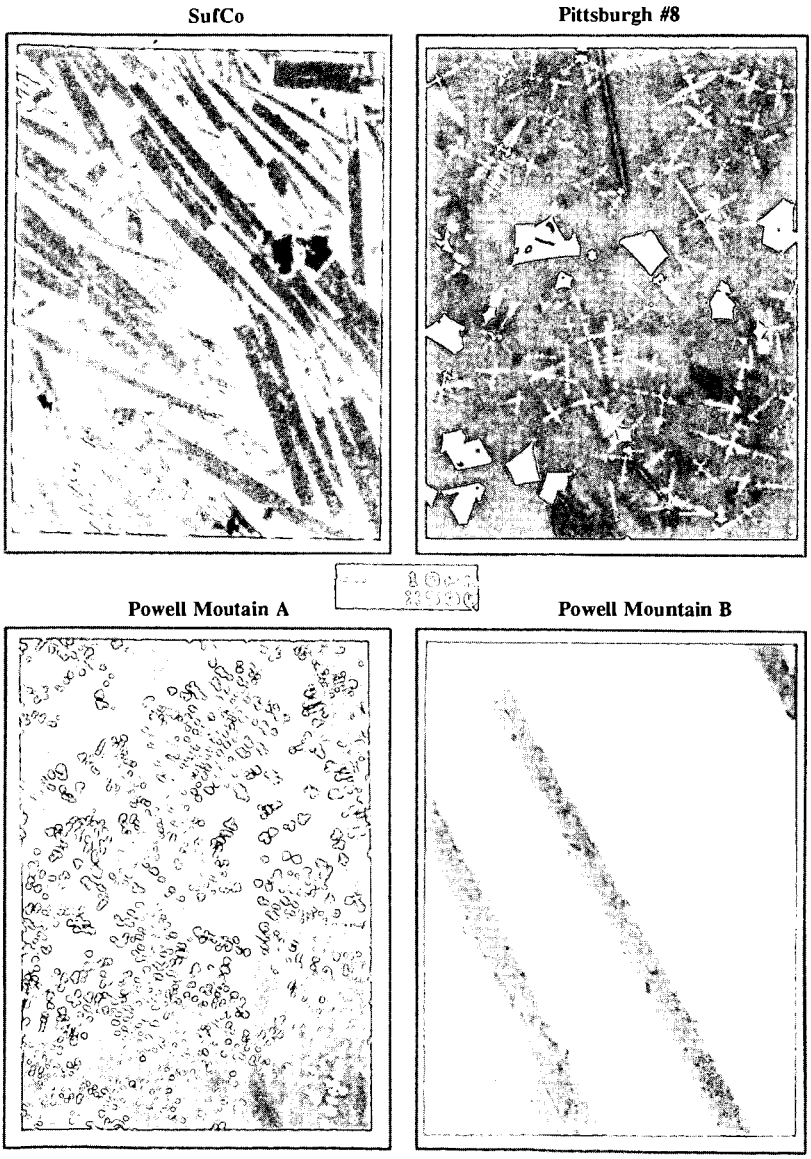
Figure 4. SEM Micrographs of Crystalline Phases in Coal Slags